

DOE/ET-53088-238

IFSR #238

**The Effect of Energetic Particles on Stability
of Mirror and Tokamak Plasmas**

Daren Stotler

Institute for Fusion Studies
The University of Texas at Austin
Austin, Texas 78712-1060

July 1986

THE EFFECT OF ENERGETIC PARTICLES ON STABILITY
OF MIRROR AND TOKAMAK PLASMAS

Publication No. _____

Daren Price Stotler, Ph.D.
The University of Texas at Austin, 1986

Supervising Professor: Herbert L. Berk

The effects of an energetic particle species on high-mode-number, curvature-driven instabilities in magnetic mirror and tokamak plasmas are studied. We will investigate whether or not these hot particles can stabilize the magnetohydrodynamic (MHD) ballooning mode by having magnetic drift velocities large enough that they do not respond on the usual time scale of the instability and consequently allow thermonuclear fusion devices to operate at higher, more efficient plasma pressures. However, the energetic particles themselves are subject to instabilities that limit the effectiveness of this procedure.

Using an MHD particle simulation code, the stabilizing effect of a diamagnetic well formed by the energetic particles is demonstrated in an axisymmetric mirror by treating the hot species as a rigid current ring. The results match those predicted by an analytic theory based on the MHD equations. More general aspects of linear stability in mirrors containing energetic particles are

examined through analysis of equations derived from the drift kinetic equation. Numerical techniques are used to show that a magnetic compressional instability can arise if the core plasma density is too high or if the hot particle pressure gradient is too large.

A similar set of equations is solved numerically in a tokamak geometry to determine whether or not energetic particles will allow access to the desirable second stability region for MHD ballooning modes. An instability with frequency on the order of the energetic particle magnetic curvature drift frequency can appear if the hot pressure gradient is too large. When the energetic species pressure peaks on the outside edge of the tokamak, the thermal energy of the species needs to be in excess of 1 MeV for this scheme to be viable. Alternative distributions with pressure peaking on the inside edge were expected to produce more favorable results. However, new instabilities are found to appear with these distributions, yielding no improvements to the stability picture. Furthermore, a simple analytic treatment predicts the loss of an important stabilizing effect with the switch of the pressure peak to the inside.

THE EFFECT OF ENERGETIC PARTICLES ON STABILITY
OF MIRROR AND TOKAMAK PLASMAS

APPROVED BY SUPERVISORY COMMITTEE:

Michael I. Bell

John D. Dalko

R. D. Hazeltine

[Signature]

James W. Van Dam

Copyright

by

Daren Price Stotler

1986

This thesis is dedicated to my
mother and father
for their never-ending
encouragement and support.

THE EFFECT OF ENERGETIC PARTICLES ON STABILITY
OF MIRROR AND TOKAMAK PLASMAS

by

Daren Price Stotler, B.A.

DISSERTATION

Presented to the Faculty of the Graduate School of

The University of Texas at Austin

in Partial Fulfillment

of the Requirements

for the Degree of

DOCTOR OF PHILOSOPHY

THE UNIVERSITY OF TEXAS AT AUSTIN

August, 1986

ACKNOWLEDGEMENTS

During the years spent working on this thesis, it has been an honor and a privilege to collaborate with and learn from Professor Herbert L. Berk. Without the many productive suggestions he has provided during our numerous discussions, this dissertation would not have been possible. I am pleased to also acknowledge significant contributions to this research made by Professor Marshall Rosenbluth and Dr. Jim Van Dam. Their insight into the topics covered by and related to this thesis has been invaluable in my work.

I would like to thank Professor Toshiki Tajima for providing me with an opportunity to become familiar with the techniques of particle simulation. The results of my collaboration with him form an integral part of the work presented here. I am also deeply indebted to Dr. Richard Hazeltine, Professor Wendell Horton, Professor John Dollard, and Dr. Patrick H. Diamond for giving me a chance to learn from them during their various classroom lectures.

I wish to express my gratitude to Dr. J. L. Geary, Dr. Y.M. Li, G. Craddock, M. J. Le Brun, E. G. Zaidman, and many other fellow graduate students too numerous to mention for their

warm friendship and support over the last several years. Finally, I want to acknowledge all of the help I received from the staff of the Institute for Fusion Studies. In particular, the efforts made by Carolyn Valentine, Dawn East, Saralyn Stewart, Suzy Crumley, and Rhandon Hurst have made my stay here an enjoyable one.

TABLE OF CONTENTS

Chapter	Page
I. INTRODUCTION	1
II. MHD SIMULATION	9
2.1 Introduction	9
2.2 Theoretical Basis	12
2.3 Simulation	16
2.3.a Equilibrium	18
2.3.b Results	25
2.4 Summary	33
III. CURVATURE-DRIVEN MODES IN EBT	34
3.1 Introduction	34
3.2 Basic Equations	37
3.3 Magnetic Compressional Mode	52
3.3.a Numerical Model	53
3.3.b Results	65
3.3.c Summary	80
3.4 Coupled Equations	83
IV. EFFECTS OF TRAPPED, ENERGETIC PARTICLES ON BALLOONING MODES IN TOKAMAKS	95
4.1 Introduction	95
4.2 Basic Equations and Numerical Model	99
4.3 Deeply Trapped Particles	118
4.3.a Growth Rates of Instabilities	120
4.3.b Stability Window	125
4.3.c Gap Modes	133
4.3.d Conclusions	145

Chapter	Page
4.4 Sloshing Particles	149
4.4.a Equilibrium Modifications	151
4.4.b Eigenmode Calculations	157
4.4.c Asymptotic Solutions (Boundary Condition Problems)	166
4.4.d Analytic Results: Full Eigenmode Equations	178
4.4.e Analytic Results: $k = 1/2$ Continuum Instability	196
4.4.f Conclusions	203
V. CONCLUSIONS	207
REFERENCES	213

LIST OF FIGURES

Figure		Page
1.1	Typical marginal stability contours for ideal MHD ballooning modes	5
2.1	Contours of the equilibrium magnetic field B_z with $\beta_h=0.9$ and $g_0=0.03$	21
2.2	Initial positions of background particles in simulation box with $r_0=10\Delta$ and $\Delta_r=4\Delta$	22
2.3	Equilibrium background plasma pressure, P_A , contours computed from particle positions	23
2.4	Magnitude of the gravity as a function of x with $g_0=0.03$ C_{s0}^2/Δ	24
2.5	Background plasma density contours at $t=100 \Delta/C_{s0}$ with $g_0=0$, $\beta_h=0$	26
2.6	Background plasma density contours at $t=50 \Delta/C_{s0}$ with $g_0=0.2$, $\beta_h=0$	27
2.7	Natural logarithm of the background fluid kinetic energy as a function of time during a run with $g_0=0.2$, $\beta_h=0$	28
2.8	Square of the growth rate plotted as a function of g_0	29
2.9	Fluid velocity vectors at various positions in the simulation box at $t=100 \Delta/C_{s0}$ with $g_0=0$, $\beta_h=0.9$	31
2.10	Fluid velocity vectors at various positions in the simulation box at $t=100 \Delta/C_{s0}$ with $g_0=0.03$, $\beta_h=0.9$	32
3.1	Imaginary part of the eigenvalue plotted as a function of Δ_{rm} with $\omega_{kh0}^2/k_{10}^2 V_A^2(0)=0.2$	67
3.2	Imaginary part of the eigenvalue plotted as a function of Δ_{rm} with $\omega_{kh0}^2/k_{10}^2 V_A^2(0)=0.014$	68

Figure	Page
3.3 Imaginary part of the eigenvalue plotted as a function of \hat{P}_c/B_{vmin}^2 with $\Delta_{rm}=0.3$	70
3.4 Eigenfunction plotted as a function of the distance along the field line for $\Delta_{rm}=0.3$ and $\hat{P}_c/B_{vmin}^2=0.002$	74
3.5 Eigenfunction plotted as a function of the distance along the field line for $\Delta_{rm}=0.3$ and $\hat{P}_c/B_{vmin}^2=0.084$	75
3.6 Negative logarithm of δ obtained by using an N term cosine series expansion for $B_{ }$	77
3.7 Eigenfunction plotted as a function of the distance along the field line for $\Delta_{rm}=0.4435$ and $\hat{P}_c/B_{vmin}^2=0.002$	78
3.8 Imaginary part of the eigenvalue for the magnetic compressional mode plotted as a function of \hat{P}_c/B_{vmin}^2	89
3.9 Imaginary part of the eigenvalue for the background pressure-driven interchange as a function of \hat{P}_{lh}/B_{vmin}^2 for $\hat{P}_c/B_{vmin}^2=0.002$, $\Delta_{rm}=0.1$	91
3.10 Imaginary part of the eigenvalue for the interacting pressure-driven interchange mode as a function of \hat{P}_c/B_{vmin}^2 for $\hat{P}_{lh}/B_{vmin}^2=0.12$	93
4.1 Imaginary part of the eigenvalue plotted as a function of α_h for (i) $\omega_{d0}/\omega_A=0.01$, (ii) $\omega_{d0}/\omega_A=0.4$, (iii) $\omega_{d0}/\omega_A=0.7$, and (iv) $\omega_{d0}/\omega_A=2.0$	121
4.2 Real part of the eigenvalue plotted as a function of α_h for (i) $\omega_{d0}/\omega_A=0.01$, (ii) $\omega_{d0}/\omega_A=0.4$, (iii) $\omega_{d0}/\omega_A=0.7$, and (iv) $\omega_{d0}/\omega_A=2.0$	122
4.3 Imaginary part of the eigenvalue plotted as a function of α_h for low-frequency, MHD and high-frequency, precessional branches with $\omega_{d0}/\omega_A=1.06$	126
4.4 Marginally stable values of α_h for low-frequency, MHD and high-frequency, precessional branches as ω_{d0}/ω_A is varied	127

Figure	Page
4.5 Marginally stable values of α_h for low-frequency, MHD and high-frequency, precessional branches as Δ_r/r is varied	128
4.6 Marginally stable values of α_h for low-frequency, MHD and high-frequency, precessional branches as ω_{*0}/ω_{d0} is varied	129
4.7 Imaginary part of the eigenvalue for the gap mode near $\omega/\omega_A=0.5$ as α_h and α_c are varied	138
4.8 Real part of the eigenvalue for the gap mode near $\omega/\omega_A=0.5$ as α_h and α_c are varied	139
4.9 Generic trajectory in the complex ω plane used to generate a Nyquist diagram	142
4.10 Path traced out in the complex g plane as $\text{Re } \omega$ is varied from $-3\omega_A$ to ω_A with $\text{Im } \omega/\omega_A = 10^{-4}$ and $\alpha_h=0.86$	143
4.11 Marginally stable values of α_h for the high-frequency precessional, low-frequency MHD, and $\text{Re } \omega/\omega_A = -1.5$ gap modes as α_c is varied	146
4.12 Variation of the perpendicular pressure function $p_{\perp}(\vartheta)$ with ϑ for (i) $\Delta\lambda=10$, (ii) $\Delta\lambda=0.1$, (iii) $\Delta\lambda=0.05$, and (iv) $\Delta\lambda=0.02$	153
4.13 Imaginary part of the eigenvalue as a function of α_h with $\Delta\lambda=10^6$, (i) $\vartheta_0=0.785$, (ii) $\vartheta_0=1.57$, (iii) $\vartheta_0=2.355$, and (iv) $\vartheta_0=3.04$	158
4.14 The value of α_h needed to get $\langle\omega_d\rangle=0$ plotted as a function of the turning point for $\Delta\lambda=10^6$, (i) $\vartheta_0=0.785$, (ii) $\vartheta_0=1.57$, (iii) $\vartheta_0=2.355$, (iv) $\vartheta_0=3.04$, and (v) $\Delta\lambda=0.02$, $\vartheta_0=3.04$	162
4.15 The imaginary part of the eigenvalue plotted as a function of α_h for $\Delta\lambda=0.02$, $\vartheta_0=3.04$ and (i) $\omega_{*0}/\omega_{d0}=0$, (ii) $\omega_{*0}/\omega_{d0}=0.55$	164

Figure	Page
4.16 Plot of $\text{Re } \delta Q$ as a function of ϑ for $\alpha_h=1.88$, $\Delta\lambda=0.02$, $\vartheta_0=3.04$, and $\omega_{*0}/\omega_{d0}=0.55$	167
4.17 Plot of γ_{\max} as a function of $\log \Delta\lambda$ for the $k=0$ mode with $\alpha_h=1.52$	172
4.18 Plot of γ_{\max} as a function of α_h for the $k = 1/2$ mode with $\Delta\lambda=0.02$	176
4.19 Plot of the real part of the frequency as a function of α_h for the $k = 1/2$ mode with $\Delta\lambda=0.02$	177

CHAPTER I

INTRODUCTION

Instabilities in plasmas are one of the main concerns of magnetically confined thermonuclear fusion research. Sources of free energy to drive instabilities can be found in any known thermonuclear fusion reactor configuration.^{1,2} Indeed, the word "confinement" implies the existence of plasma density gradients; since thermonuclear plasmas must also be very hot, there can be a corresponding pressure gradient, a possible driving force for instability.³ Many plasma confinement devices introduce curvature of magnetic field lines and gradients of magnetic field strength perpendicular to the field; both of these features provide mechanisms for instabilities that can tap this energy source.^{4,5} In regions of the machine where the field lines curve away from the plasma (the radius of curvature and the pressure gradient are in the same direction), it is energetically favorable for magnetic flux tubes in the center of the plasma to "interchange" with those in lower density regions. As long as the pressure gradient remains, the motion grows in amplitude, leading to a loss of confinement. This interchange instability⁴ may be modeled by a

gravitational force that acts in the same direction for both plasma ions and electrons (the gravitational instability). In this way one is reminded of the Rayleigh-Taylor instability of hydrodynamics arising when a heavy fluid (i.e., the plasma) is supported by a lighter one (the vacuum with magnetic fields) against a gravitational force of some sort.

If the field lines curve toward the plasma, these same perturbations only give rise to stable oscillations in magnetohydrodynamic (MHD) theory. In this case one speaks of "favorable" curvature, and of "unfavorable" curvature in the former situation. In general, regions of both signs of curvature will be present in a confinement device, and stability is determined by an average along a field line, using appropriate weighting. Because the mode amplitude is mostly constant along the field line, but has a modulation in the perpendicular direction, the interchange instability is sometimes referred to as the flute instability (as in the fluted columns of architecture). Given that the perturbation leaves the equilibrium field unchanged, a relatively straightforward calculation can be made to evaluate the interchange stability properties of an azimuthally symmetric system. The result is the so-called $\int dl/B$ criterion; namely $d/d\psi(\int dl/B) < 0$ is required for stability^{4,6} (B is the magnetic field strength; l is the arc length along the field line; the integral is computed over the range of l , and ψ labels the magnetic flux surfaces). For a

simple magnetic mirror, the result is that the unfavorable curvature dominates, and the system is susceptible to the interchange instability at all values of the pressure gradient.

In the case of the tokamak, the analysis is more complicated. Both the vacuum toroidal field and the poloidal field produced by an induced toroidal plasma current are necessary to provide ideal MHD equilibrium and stability.^{1,7} The tokamak design introduces magnetic shear into the system; that is, the direction of the magnetic field lines changes as we go from one magnetic flux surface to another. Now, for the interchange of flux tubes to take place as before, field lines must be bent to overcome the shear. Even without the stabilizing effect of the shear, the tokamak satisfies the jdl/B criterion. This is due to the presence of a region of favorable (or good) curvature on the inside of the tokamak. As a result, the most unstable mode is no longer constant along the field line; rather, it peaks, or "balloons" in the region of bad curvature. Hence, this particular manifestation of the interchange instability is referred to as a ballooning mode. However, the energy required to bend the field lines and allow the perturbation to overcome the magnetic shear is large enough that the system can be stable with a nonzero pressure gradient. In general, detailed analysis of their stability characteristics in tokamaks requires numerical analysis.⁸⁻¹⁹

The ideal, MHD treatment leads to a relation between the critical pressure gradient at the onset of instability and the shear in the system. It can also be shown via MHD theory that the most unstable ballooning modes are localized to one flux surface.⁸ Consequently, two variables representing the local shear and local plasma pressure gradient are all that is needed to specify the problem. The results of the ideal MHD calculation can then be expressed as a marginal stability curve in the space of these two parameters. Of course, all of the flux surfaces in the tokamak must be examined to completely characterize the ballooning stability of a particular equilibrium.

Investigations discussing the effects of a significant β (ratio of plasma energy to magnetic energy) plasma on the equilibrium and found that for large enough pressure gradients, the stability of the system with respect to ballooning modes actually improves with increasing β .^{11-13,16-19} The result is a second marginal stability line in the plot of critical pressure gradient versus shear, depicted qualitatively in Fig. 1.1. Larger pressure gradients than this fall into a "second stability" region. The physical reasons for this behavior stem from the fact that at significant β , the flux surfaces become so distorted that the local (localized in poloidal angle) shear is altered from its vacuum value. The effect increases the shear in the bad curvature region, and thus improves stability.

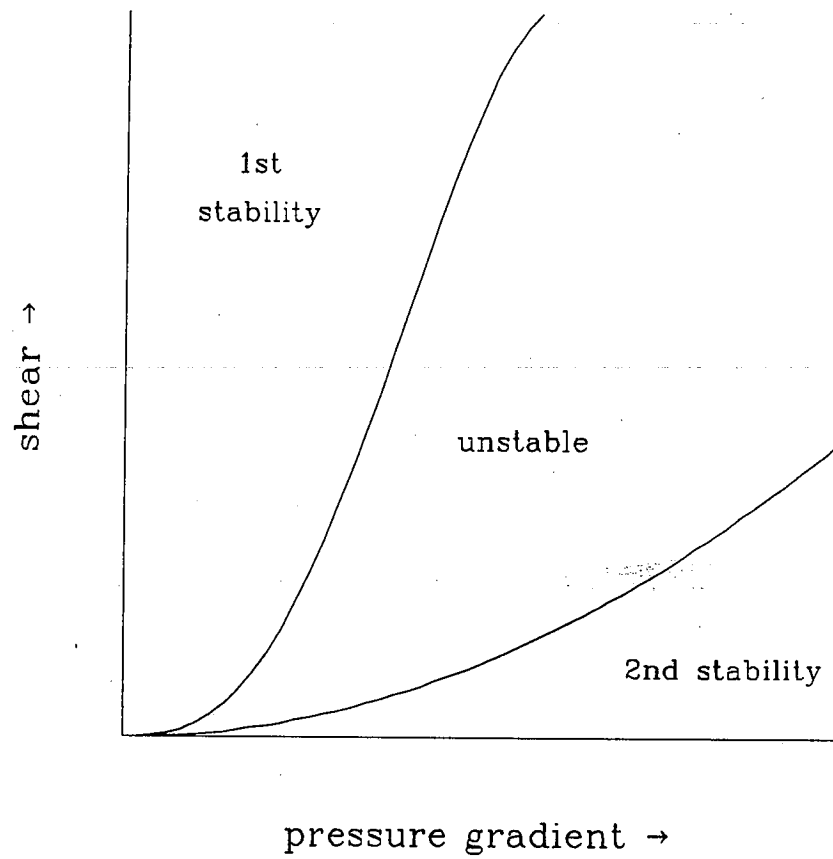


Fig. 1.1. Typical marginal stability contours for ideal MHD ballooning modes as a function of plasma pressure gradient and magnetic shear.

Operation of a reactor in the second stability regime is desirable for the higher values of β , and consequently of fusion power density, that can be achieved. However, it is unclear how to bridge the unstable range of pressure gradients in actual machine operation starting from the first stability regime. Thus, as was the case for the magnetic mirror, the ballooning modes present obstacles to the design of a viable tokamak reactor. It is the goal of this dissertation to examine some of the aspects of one approach to circumventing these limitations. In particular, we will consider how an energetic plasma component might be used to stabilize curvature-driven modes in magnetic mirrors and tokamaks.

The use of energetic particles for this purpose has been investigated in connection with Astron²⁰ and with ion ring devices.^{21,22} More recently, they have apparently had a stabilizing effect in the ELMO,²³ ELMO Bumpy Torus²⁴⁻²⁶ (EBT) and Nagoya Bumpy Torus^{27,28} devices, as well as in axisymmetric tandem mirror end-cells.^{29,30} The traditional theory of this concept is that sufficiently energetic particles will have large magnetic drift velocities and, therefore, will not respond on the time scale of the MHD perturbations that give rise to the interchange instability. The result is that different portions of the plasma are connected so that the destabilizing potential arising from the opposite magnetic drifts of the core ions and electrons is shorted out. At the same time, we can say that the hot particle pressure

digs a self-consistent diamagnetic "well" that provides $j d\ell/B$ stabilization.⁶ However, recent data indicates that other processes may actually be responsible for plasma stability in these devices.^{31,32} Finite Larmor radius (FLR) effects, both of the core ions and energetic electrons, may play a part in stabilization of the various modes present.³³⁻³⁵ The uncanceled $\underline{E} \times \underline{B}$ drift created when $n_c \neq n_e$ (n_c = the core ion density, n_e = core electron density) can provide a stabilizing frequency shift analogous to FLR stabilization if the hot electron density, $n_h = n_c - n_e$, is large enough (also referred to as charge uncovering).^{36,37} Also, inversion of the core plasma temperature profile may lead to stabilization.^{6,31,38}

The success of these methods in EBT has led to the suggestion that similar techniques be used in a tokamak to access second stability.³⁹ In this case, the energetic particles would be needed only in crossing the region between first and second stability.

Unfortunately, the introduction of a new species into a system brings with it new modes of instability. For instance, one must ask whether or not the hot electron rings of EBT will themselves be susceptible to instability. Theoretical work on Astron determined that the precessional magnetic drifts of the hot electron layer gave rise to a negative energy mode which was destabilized by interactions with positive energy waves or with

sources of positive dissipation⁴⁰⁻⁴². This same negative energy mode was also examined in connection with EBT⁴³⁻⁴⁶ and tandem mirrors having hot electron-stabilized end cells.⁴⁶⁻⁴⁹

In Chapter II of this dissertation, we will first consider the mechanisms by which a noninteracting hot electron ring can stabilize the EBT core plasma with respect to the interchange mode by digging a diamagnetic well. An MHD particle code will be used to demonstrate this; nonlinear as well as radial effects may be examined in this way. Chapter III discusses some of the other instabilities present in EBT. We will focus our attention on a purely magnetic mode that arises in connection with the hot electron precessional drifts. In Chapter IV we investigate the possibility of using energetic particles to access the second stability region for tokamaks. However, the precessional drift resonant mode may limit the effectiveness of this approach. An alternative hot particle distribution that peaks in good curvature should improve the stability of the drift resonant mode. Finally, in Chapter V we present an overall summary of the results of this dissertation.

CHAPTER II

MHD SIMULATION

2.1 Introduction

The stabilizing effect of energetic particles in simple mirror geometries has been known for quite some time. In the ELMO canted mirror, electron cyclotron resonance heating was used to raise the plasma temperature, but the resulting annular distribution of hot electrons was found to also have a stabilizing influence on the core plasma.²³ This concept led to the ELMO Bumpy Torus (EBT) device and other similar experiments.^{25,27-30}

The curvature drift frequencies of the hot electrons are larger than is permitted by the usual MHD ordering. In fact, their stabilizing influence relies upon the fact that they do not respond to perturbations on typical MHD time scales and can provide diamagnetic well stabilization. Thus, it is possible to demonstrate the desired effect by treating the hot electrons as a rigid current ring immersed in an MHD core plasma⁶. If three conditions are met: (i) the core β , β_c , is much less than $2\Delta_r/R$ (Δ_r is the gradient scale length, and R is the mirror radius of

curvature), (ii) the hot electron curvature drift frequency is larger than twice the typical MHD growth rates for the system, and (iii) the density ratio of the hot to core components is much less than unity, this is valid treatment of the system.⁵⁰

The origins of these criteria, and the instabilities which arise if they are not met will be discussed in Ch. III. Instead, we will assume that these conditions hold and carry out a simulation of an EBT mirror cell using an MHD particle code^{51,52} with a fixed current ring included to represent the effects of the hot electrons. In cases where $\beta_c \sim 2\Delta_r/R$, the interactions of the core plasma with the ring must be accounted for, as demonstrated originally by Nelson⁵³ and by Van Dam and Lee.⁵⁴ The plasma may then become susceptible to interchange instabilities for all values of the hot electron β . A possible extension of the work described here would be to include such effects.

Ohsawa and Dawson³⁵ described a simulation of an EBT plasma using a 2 1/2-D, fully electromagnetic and relativistic particle code with a slab geometry. In addition to demonstrating stabilization of the core plasma interchange mode, they were able to observe finite hot electron Larmor radius effects and the low frequency hot electron interchange instability. The methods adopted here differ in several respects. The primary distinction is that the MHD equations are used to determine the response of the core plasma instead of Maxwell's equations. The hot electrons are

then treated as a fixed current ring and enter as a $\underline{j}_h \times \underline{B}$ term in the force on the fluid particles (\underline{j}_h is the ring current density, and \underline{B} is the magnetic field). The advantage is that the time step of the simulation can be much larger than in an electromagnetic calculation, and, hence, phenomena occurring on the MHD time scale can be examined much more cheaply. However, it is not trivial to extend this treatment to include interactions between the hot and core components.

The assumption of a charge-neutral background plasma (valid if the hot electron density is much less than the background density), as in ideal MHD theory, prevents us from observing charge uncovering effects.^{36,37} Again following ideal MHD theory, we neglect ion and hot electron FLR effects, removing the possibility of seeing that stabilization mechanism.³³⁻³⁵ In other words, we focus here on stabilizing the background pressure-driven interchange mode by digging a diamagnetic well with the hot electron current and leave the investigation of the other suggested stabilizing effects³¹ to more detailed treatments such as the one by Ohsawa and Dawson.

The simulations to be discussed in this chapter are 2 1/2-D; that is, variations in two spatial and three velocity dimensions are allowed. The equilibrium is set up to represent the vertical cross section of the midplane of an EBT mirror cell with a radial gravity taking the place of magnetic field line curvature.

The code employed here allows the extension to three dimensional calculations, if desired.

Our objective is to demonstrate that the plasma is unstable in the presence of a nonzero gravity, but can be stabilized to a large degree if the ring current is strong enough. In this chapter, we will first show that this is the prediction of a linear analytic treatment based on the MHD equations. After describing the equilibrium geometry used in the code, we will present the results of several simulations. The chapter ends with a brief summary and discusses possible future work with this code.

2.2 Theoretical Basis

A linear analysis of the system of equations to be used in the simulations yields values of the growth rate for the interchange mode and predicts the size of the hot component current j_h needed to provide stability.

First, we write the MHD force equation for the core plasma motion (e.g., see Ref. 7) as

$$\rho \frac{d\mathbf{v}}{dt} = \mathbf{j}_p \times \mathbf{B} - \nabla P + \rho \mathbf{g}, \quad (2.1)$$

where ρ , \mathbf{v} , P and \mathbf{j}_p are the core plasma density, fluid velocity,

core plasma pressure, and current density associated with the background plasma, respectively. \underline{B} is the magnetic field, and \underline{g} is any gravity-like force present. The total current is the sum of the plasma current and the current due to the hot electron ring,

$$\underline{j} = \underline{\nabla} \times \underline{B} = \underline{j}_p + \underline{j}_{hot}, \quad (2.2)$$

so that

$$\rho \frac{d\underline{v}}{dt} = (\underline{\nabla} \times \underline{B}) \times \underline{B} - \underline{\nabla} P + \rho \underline{g} - \underline{j}_{hot} \times \underline{B}. \quad (2.3)$$

From standard MHD theory, we have equations describing the density and magnetic field evolution,

$$\frac{\partial \rho}{\partial t} + \underline{\nabla} \cdot (\rho \underline{v}) = 0, \quad (2.4)$$

and

$$\frac{\partial \underline{B}}{\partial t} = \underline{\nabla} \times (\underline{v} \times \underline{B}). \quad (2.5)$$

To close the system of equations, we use an adiabatic equation of state,

$$\frac{d}{dt}(P/\rho^\gamma) = 0, \quad (2.6)$$

where γ is the ratio of specific heats.

Now, we assume perturbations of the form

$$\tilde{f}_1(\underline{x}, t) = f_1(r) \exp(-i\omega t + im\vartheta), \quad (2.7)$$

where f_1 represents a field variable, and linearize Eqs. (2.3)-(2.6). Note that in this geometry, $\underline{B} = B_z \hat{z}$, $\underline{g} = g\hat{r}$, and all equilibrium quantities vary in only the radial direction. Thus,

$$P_1 = \frac{-i}{\omega} \left\{ \left[\frac{1}{r} \frac{d}{dr}(rv_r) + ik_\vartheta v_\vartheta \right] \gamma P_0 + v_r \frac{dP_0}{dr} \right\}, \quad (2.8)$$

$$\rho_1 = \frac{\rho_0}{\gamma} \frac{P_1}{P_0}, \quad (2.9)$$

$$\underline{B}_1 = \frac{-i}{\omega} \left\{ \left[\frac{1}{r} \frac{d}{dr}(rv_r) + ik_\vartheta v_\vartheta \right] B_0 + v_r \frac{dB_0}{dr} \right\} \hat{z}, \quad (2.10)$$

where $k_\vartheta = m/r$, m is the poloidal mode number, and the 0 subscript denotes an equilibrium quantity. The force equation has two nontrivial components,

$$-i\omega\rho_0 v_r = -B_1 \frac{dB_0}{dr} - B_0 \frac{dB_1}{dr} - \frac{dP_1}{dr} + \rho_1 g - j_{\text{hot}} B_1, \quad (2.11)$$

and

$$-i\omega\rho_0 v_{\parallel} = -ik_{\parallel} B_1 B_0 - ik_{\parallel} P_1. \quad (2.12)$$

Note that j_{hot} has been taken to be constant in time due to the noninteracting ring assumption. A great simplification arises if we set the right-hand side of Eq. (2.12) to zero. This is valid as long as $\omega/k_{\parallel} \ll V_A$, where V_A is the Alfvén velocity, and essentially removes the compressional Alfvén wave from consideration. In any event, the code used here is incapable of resolving waves with phase velocities of order V_A . Combining Eqs. (2.8)–(2.11) with this information yields a dispersion relation,

$$\omega^2 = \frac{-g\left(\frac{d}{dr} \ln B_0 - \frac{1}{\gamma} \frac{d}{dr} \ln P_0\right) \left(1 + \frac{j_h \gamma P_0}{\rho_0 B_0 g}\right)}{\left(1 + \frac{\gamma P_0}{B^2}\right)}. \quad (2.13)$$

Since the force equation for the hot electrons can be written as

$$j_{\text{hot}} \times \underline{B} = \underline{\nabla} P_{\text{hot}}, \quad (2.14)$$

$j_h = j_{\text{hot}} \cdot \hat{\vartheta} < 0$ when $dP_{\text{hot}}/dr < 0$. If we write $dP_{\text{hot}}/dr \sim -P_{\text{hot}}/\Delta_r$, so

that Δ_r defines a gradient scale length, and require that $g \sim v_{th}^2/R$ (v_{th} represents the thermal velocity of the core plasma, R is the radius of curvature of the mirror field being modeled),

$$\frac{j_{hot} \gamma P_0}{\rho_0 B_0 g} \sim - \frac{P_{hot} R}{B_0^2 \Delta_r} = - \frac{\beta_{hot} R}{2 \Delta_r} \quad (2.15)$$

So, stability can be obtained for $g > 0$ if $\beta_{hot} R / 2 \Delta_r > 1$, essentially the criterion found by Nelson and Hedrick⁶ through a more rigorous analysis. Likewise, if we arrange the parameters of the simulation such that

$$\left| \frac{j_{hot} \gamma P_0}{\rho_0 B_0 g} \right| > 1, \quad (2.16)$$

no growth of the interchange mode should be observed.

2.3 Simulation

The MHD particle code used to carry out the simulation was developed largely by Brunel and is described in detail in Refs. 51 and 52. The algorithm employed there treats elements of the MHD fluid as finite-sized particles; the force on these particles is then given by Eq. (2.1). Fluid densities and velocities are

computed directly from the particle positions and velocities. They are then stored along with the magnetic field strength on a fixed background grid. Since mass and momentum are conserved exactly in this scheme, unphysical effects such as negative densities arising from improper treatment of the advective derivatives in the fluid equations are avoided.

Two additional features of this code are noteworthy. First, interpolation of various quantities from the grid to the particle positions and vice-versa is accomplished by an area weighting scheme.⁵⁵ This method represents a factor of $k\Delta$ (k is the wavenumber of some perturbation; Δ is the grid spacing) improvement in accuracy relative to the nearest grid point method in which field values at the particle positions are taken to be those at the nearest grid point. Secondly, a time-centered Lax-Wendroff scheme⁵⁶ is used to push the magnetic field, significantly reducing numerical diffusion of magnetic fields relative to that which occurs when simpler methods are adopted.

This version of the code also employs finite difference methods to calculate derivatives; hence no Fourier transforms need to be computed. It is set up to run in 2 1/2-D with reflecting boundary conditions in the two spatial dimensions, although 3-D simulations are also possible.

2.3.a Equilibrium

In order to simulate the midplane of a single magnetic mirror cell, \underline{B} is taken to be in the \hat{z} direction, perpendicular to the plane of the computational box, with a radial gravity representing the field line curvature. After labeling some point near the center of the computational box as the origin of a polar coordinate system (r, ϑ) to be superimposed on the usual (x, y) coordinates, we can specify pressure profiles for the core and hot electron plasmas, as well as the gravity,

$$P(r) = P_0 \begin{cases} 1 & r < r_0 \\ \exp[-(r-r_0)^2/\Delta_r^2] & r > r_0 \end{cases} \quad (2.17a)$$

$$P_{\text{hot}}(r) = \beta_h \frac{B_0^2}{2} \exp[-(r-r_0)^2/\Delta_r^2], \quad (2.17b)$$

$$g(r) = g_0 \left[\frac{1}{2} \frac{r}{r_g} + \frac{1}{16} \left(\frac{r}{r_g} \right)^3 \right], \quad (2.17c)$$

where B_0 is the vacuum magnetic field (uniform in x and y); β_h and Δ_r will be used to alter the degree of influence of the hot electrons. This particular form for $g(r)$ is derived from the expected radial dependence of the midplane radius of curvature in a vacuum magnetic mirror field, essentially a Bessel function

$I_1(r/r_g)$, expanded for $r/r_g \ll 1$. For a mirror of length L , $r_g = L/2\pi$; we assume here $L = 4r_0$ so that $r_g = 2r_0/\pi$. The equation of state prescribes a desired density profile for the core plasma $\rho_I(r)$,

$$\frac{P(r)}{P_0} = \frac{[\rho_I(r)]^\gamma}{\rho_0^\gamma}, \quad (2.18)$$

where ρ_0 is the average mass density of the system; the corresponding average pressure P_0 is defined in terms of a sound speed, $C_{s0} = (\gamma P_0 / \rho_0)^{1/2}$.

The core particles are placed in the computational box so that their density ρ_A matches as closely as possible the ideal density ρ_I . Note that due to the rectangular configuration of the grid and the finite number of particles used, ρ_A (subscript A refers to actual value) will generally be a function of x and y instead of just r . The corresponding actual particle pressure is given by

$$\frac{P_A}{P_0} = \frac{\rho_A^\gamma}{\rho_0^\gamma}. \quad (2.19)$$

The equilibrium can then be calculated from the steady state version of Eq. (2.3),

$$\frac{d}{dr} \left(\frac{B_z^2}{2} + P_A + P_{\text{hot}} \right) = \rho_I(r)g(r). \quad (2.20)$$

Note that Eq. (2.14) has been used to write

$$j_{\text{hot}} = \frac{1}{B_z} \frac{dP_{\text{hot}}}{dr} \hat{\vartheta}, \quad (2.21)$$

where j_z will be held constant during the simulation.

By integrating Eq. (2.20) we find the equilibrium magnetic field $B_z(x,y)$. Since the actual force specified by Eq. (2.3) involves $\rho_A(x,y)$ and not $\rho_I(r)$, there will be errors in the equilibrium directly related to the size of $|\rho_A(x,y) - \rho_I(r)|$. The Gaussian profile used here was chosen in order to minimize the error. Since this problem enters only through the ρg term, equilibria computed for $g=0$ are exact. In Figs. 2.1-2.4 we present the results of a typical equilibrium calculation. Note in particular the changes in B_z (Fig. 2.1) and P_A (Fig. 2.3) as r increases through r_0 .

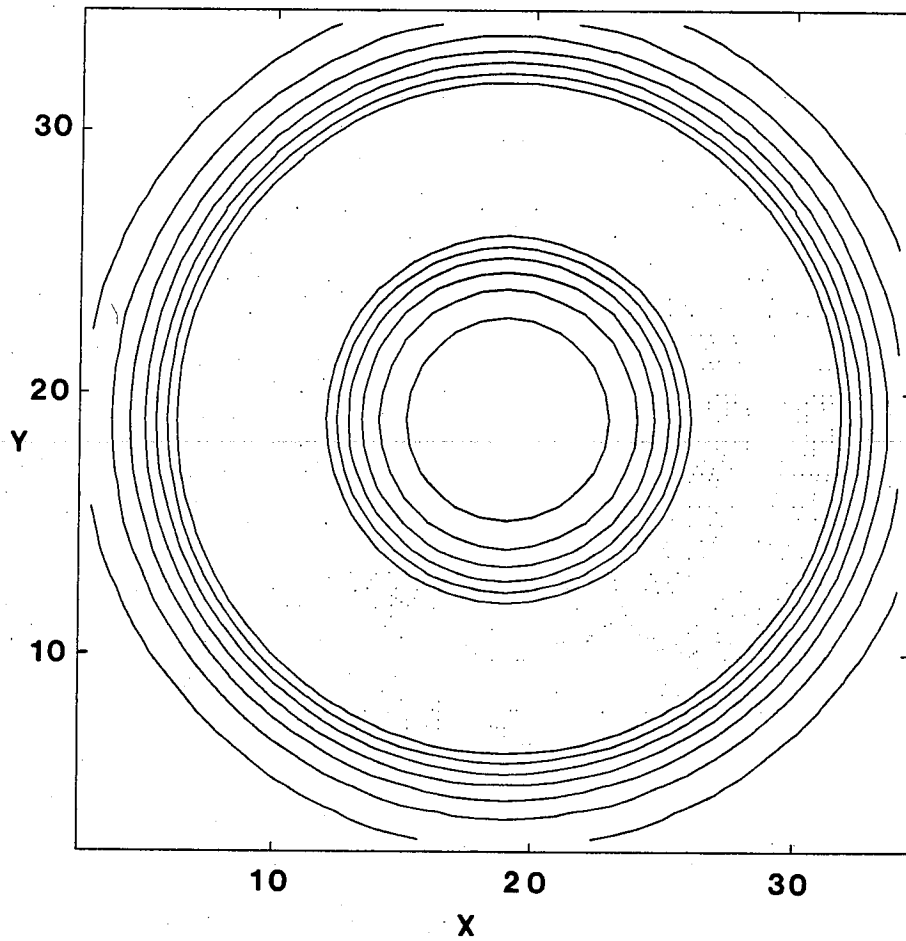


Fig. 2.1. Contours of the equilibrium magnetic field B_z with $\beta_h = 0.9$ and $g_0 = 0.03$.

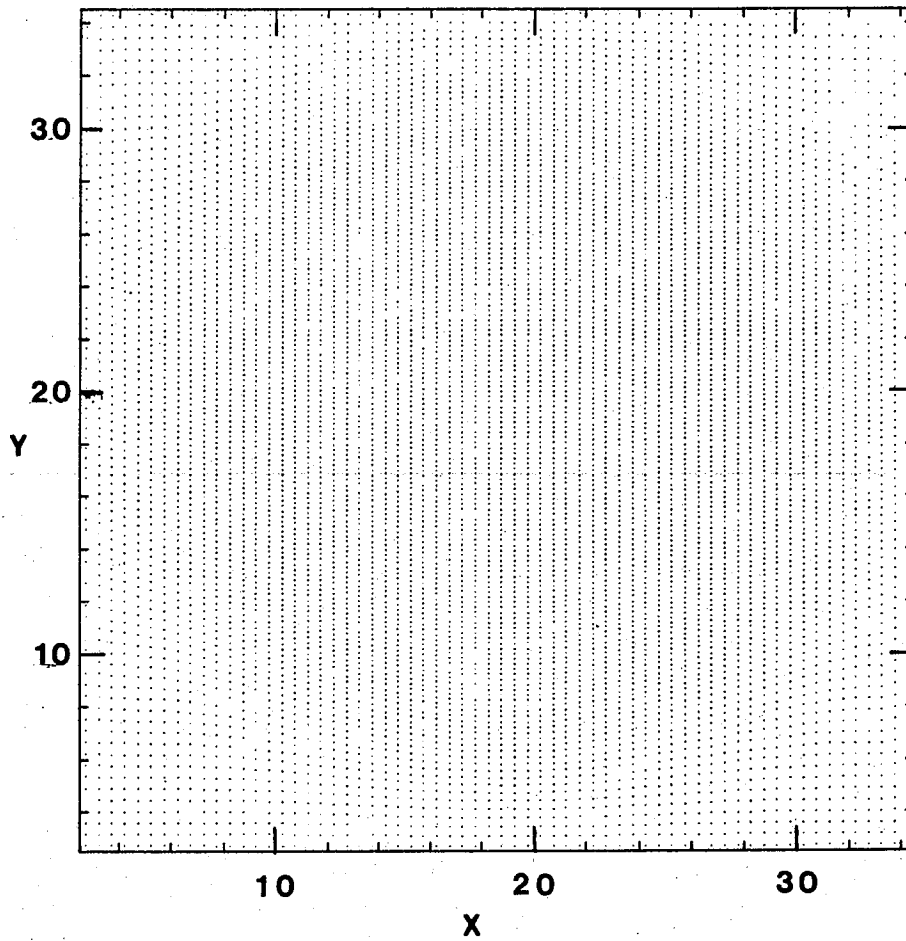


Fig. 2.2. Initial positions of background particles in simulation box with $r_0 = 10\Delta$ and $\Delta_r = 4\Delta$.

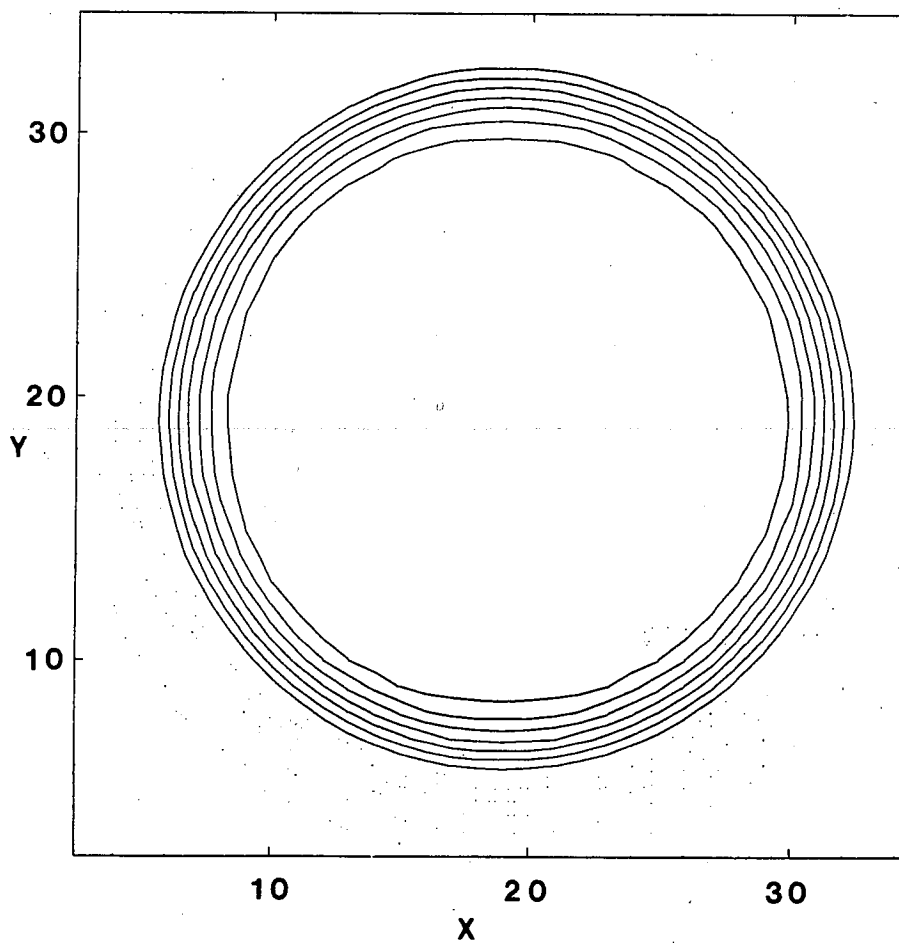


Fig. 2.3. Equilibrium background plasma pressure, P_A , contours computed from particle positions shown in Fig. 2.2.

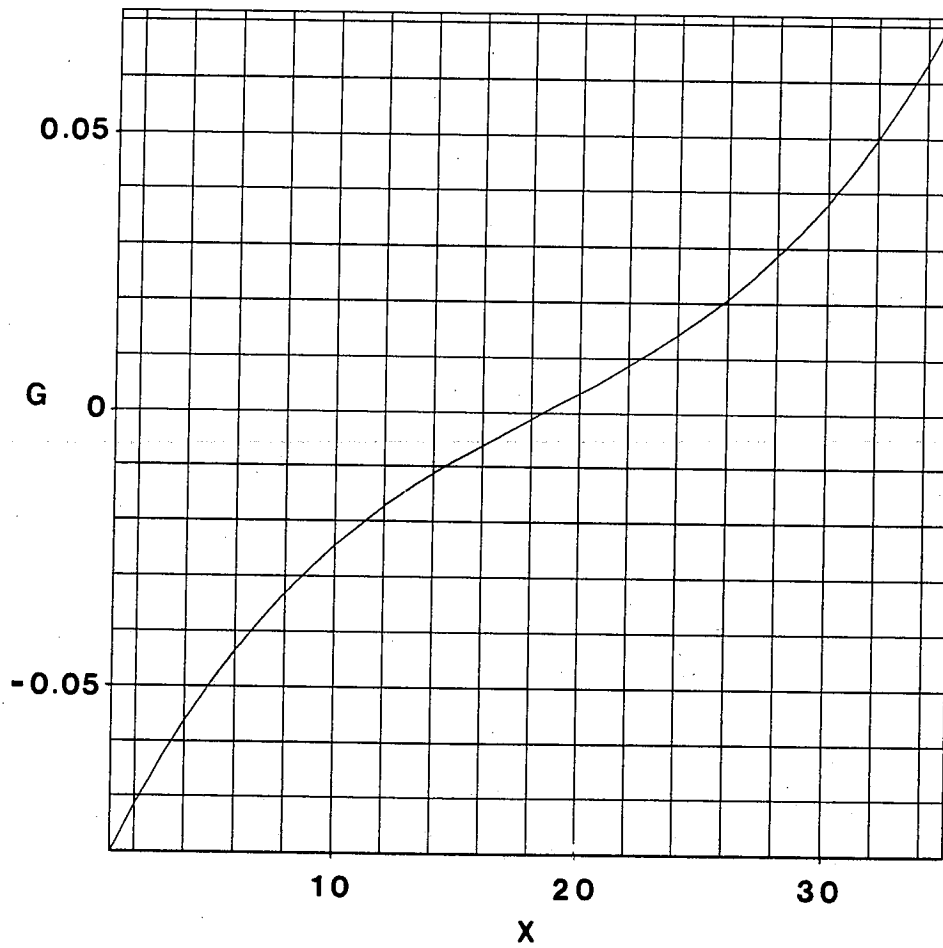


Fig. 2.4. Magnitude of the gravity, $G(x) \equiv g(r) \hat{r} \cdot \hat{x}$, defined in Eq. (2.17c) as a function of x at $y=18.5$ (passing through $r=0$) with $g_0 = 0.03 C_{s0}^2 / \Delta$.

2.3.b Results

We will investigate the effects of gravity and the fixed current ring in three steps. First, we set $g=0$ and $\beta_h=0$; the system should be stable in this case. Second, we try $g \neq 0$, $\beta_h=0$; Eq. (2.13) predicts instability and gives an estimate of the growth rate when evaluated at some appropriate radius, $r > r_0$.

Finally, for $\beta_h \neq 0$, we will compare runs in which $g=0$ and $g \neq 0$. If Eq. (2.13) predicts $\omega^2 > 0$ over most of the simulational plasma, the system ought to be stable.

A couple of different diagnostics must be used to effectively differentiate stability and instability. In the first case, we consider $g=0$, $\beta_h=0$. We have set $r_0=10\Delta$ and $\Delta_r=4\Delta$ for this run and all others to follow. Fig. 2.5 shows a contour plot of the particle density at $t=100 \Delta/C_{s0}$. The particle distribution has roughly retained its initial circular symmetry, and the density gradient for $r \gtrsim r_0$ is intact. Thus, we conclude that the system is indeed stable when the gravity force is not present.

Next, in Fig. 2.6, we see the same type of plot for $g_0=0.2 C_{s0}^2/\Delta$, $\beta_h=0$ at $t=50 \Delta/C_{s0}$. Clearly, in this case the instability has evolved into a nonlinear state. The linear growth rate can be obtained by examining the fluid kinetic energy, as in Fig. 2.7. In Fig. 2.8, the resulting growth rate is plotted for different values of g along with the value of $\gamma^2 = -\omega^2$ obtained from Eq. (2.13)

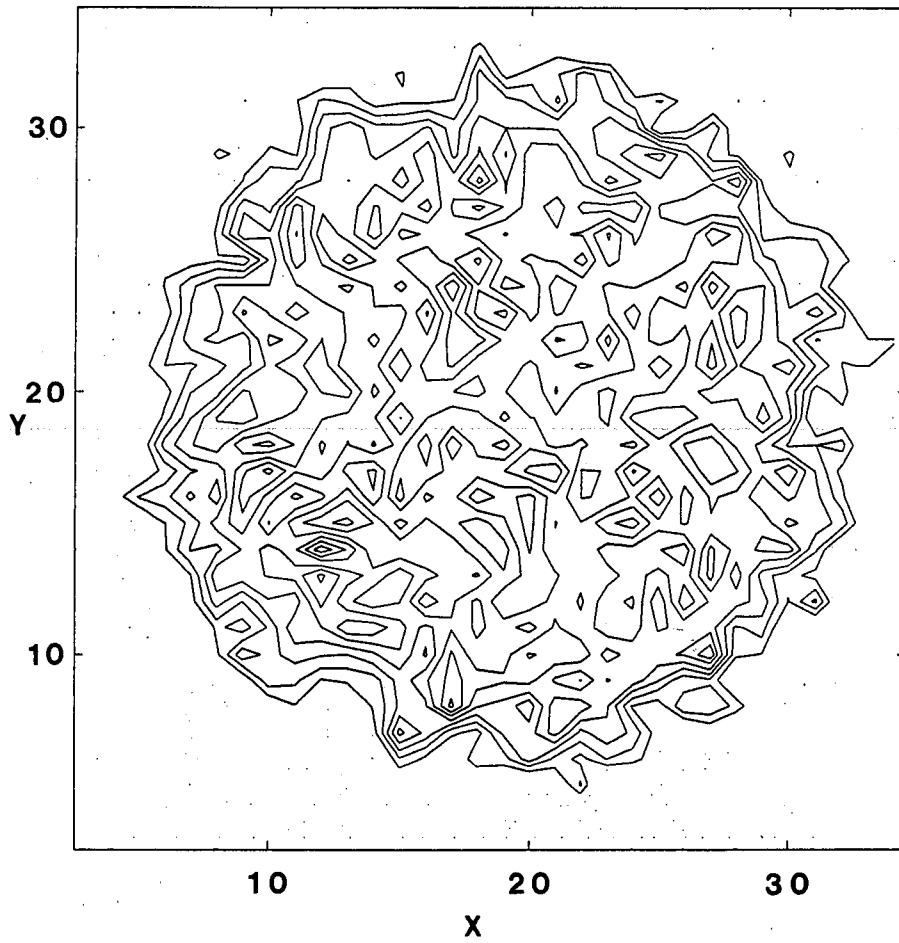


Fig. 2.5. Background plasma density contours at $t = 100 \Delta/C_{s0}$ with $g_0=0$, $\beta_h=0$.

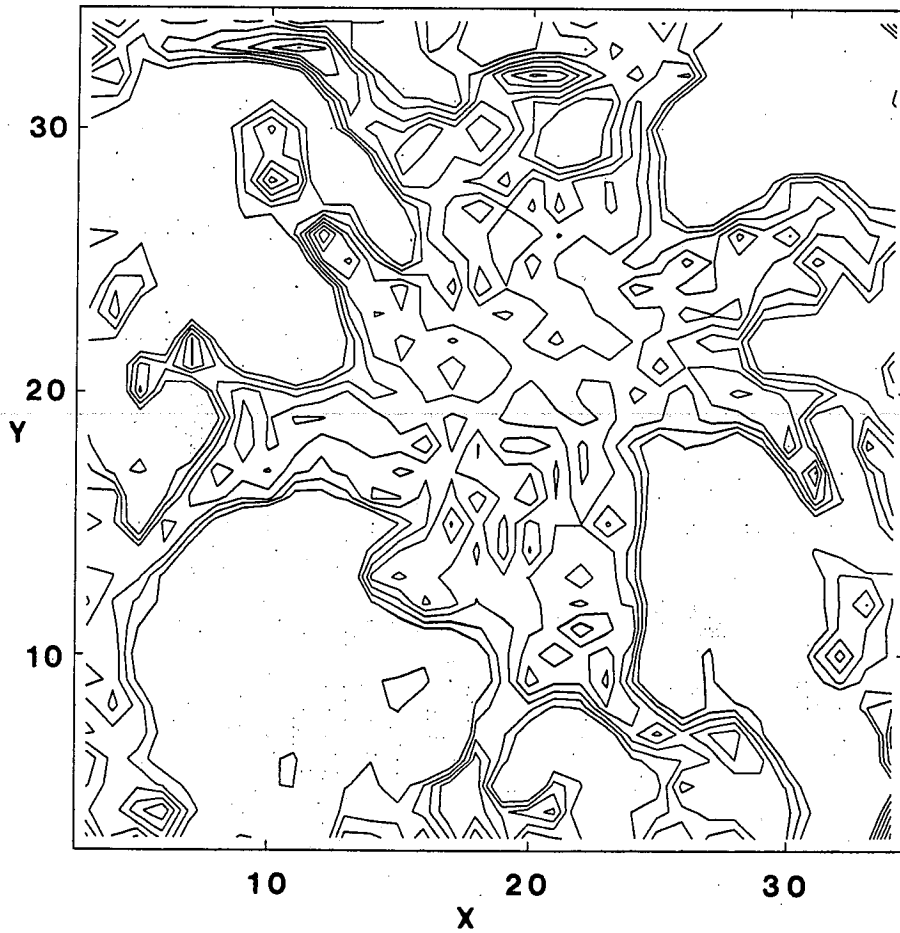


Fig. 2.6. Background plasma density contours at $t = 50 \Delta/c_{s0}$ with $g_0=0.2$, $\beta_h=0$.

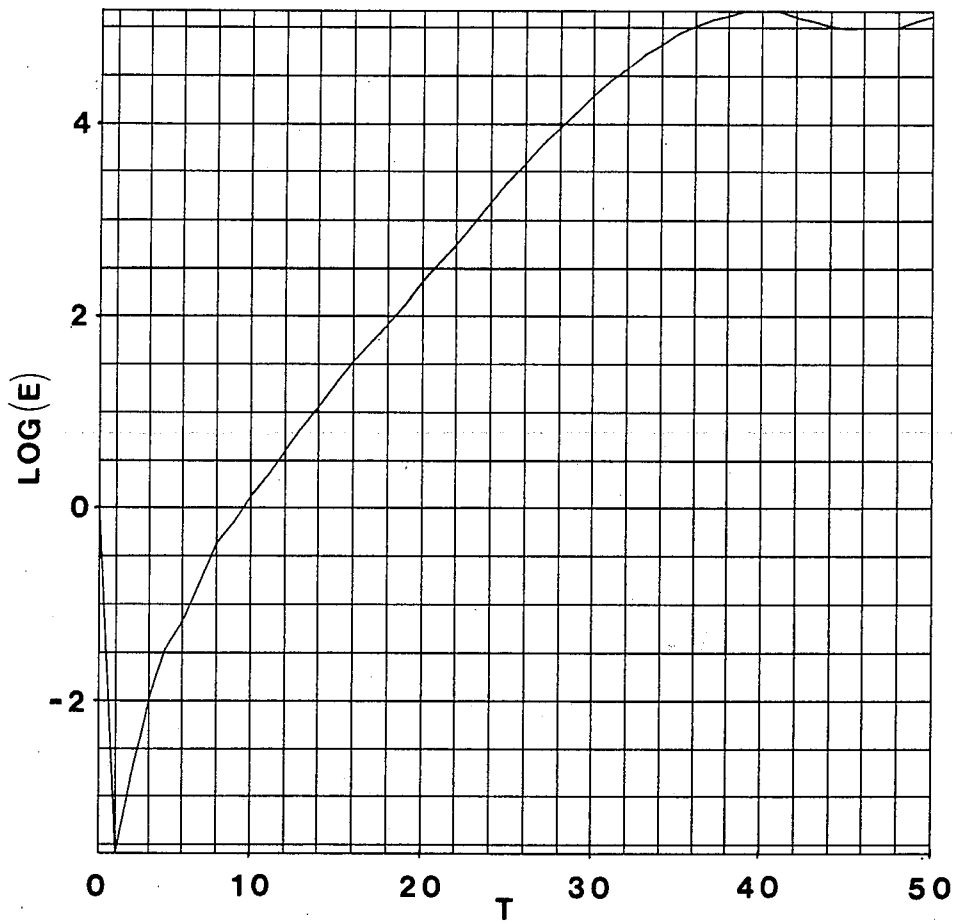


Fig. 2.7. Natural logarithm of the background fluid kinetic energy, E , as a function of time T (in units of Δ/C_{s0}) during a run with $g_0=0.2$, $\beta_h=0$.

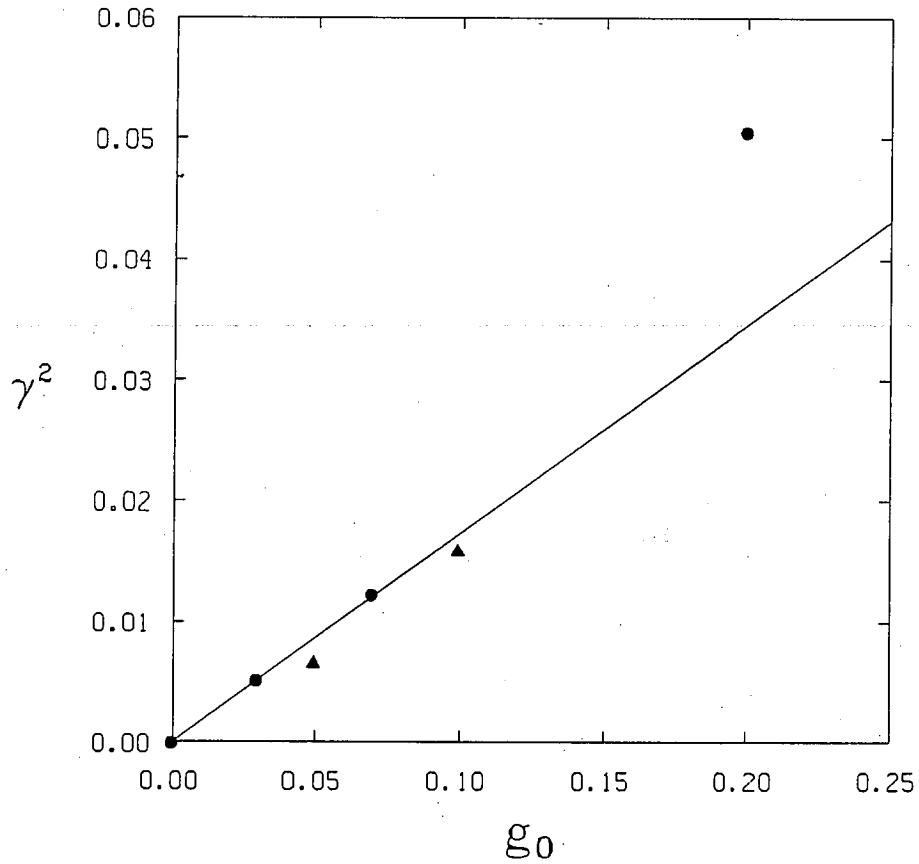


Fig. 2.8. Square of the growth rate γ (in units of Δ^2/c_{s0}^2) calculated from the fluid kinetic energy plotted as a function of g_0 . The solid line represents the value predicted by Eq. (2.13). The solid circles denote results of simulations using the Gaussian pressure profiles, Eqs. (2.17a) and (2.17b). The solid triangles denote use of a parabolic pressure profile not discussed here.

(evaluated at $r=r_0+3\Delta_r/4$). Note that two runs made with parabolic pressure profiles are included as well.

Finally, we discuss the case in which $g \neq 0$ and $\beta_h \neq 0$. Note that the analysis leading to Eq. (2.13) is local, whereas the simulation represents a solution of Eqs. (2.3)-(2.6) with full radial effects. In fact, with the profiles used here, one can see that at sufficiently large β_h , $\omega^2=0$ at some radius, $r=r_c$, and that $\omega^2(\gtrless)0$ for $r(\gtrless)r_c$. This is apparent in Figs. 2.9 and 2.10; each of these is a plot of the fluid velocity vectors at various grid points. In Fig. 2.9, $g_0=0$, $\beta_h=0.9$, and as one expects in a stable equilibrium, there is little more than random thermal motion present. In Fig. 2.10, $g_0=0.03 C_{s0}^2/\Delta$ and $\beta_h=0.9$; the values of g and β_h were chosen so that $r_c \approx r_0+3\Delta_r/4$ (most of the plasma is stable). Appropriately, one sees the vortices characteristic of interchange instability, but only in the corners of the box where $r > r_c$. A value of g large relative to what is expected from typical EBT-S⁵⁷ parameters is used here to shorten the time scale of the instability for economic reasons. Consequently, the critical β_h is also far greater than necessary in actual experiments.

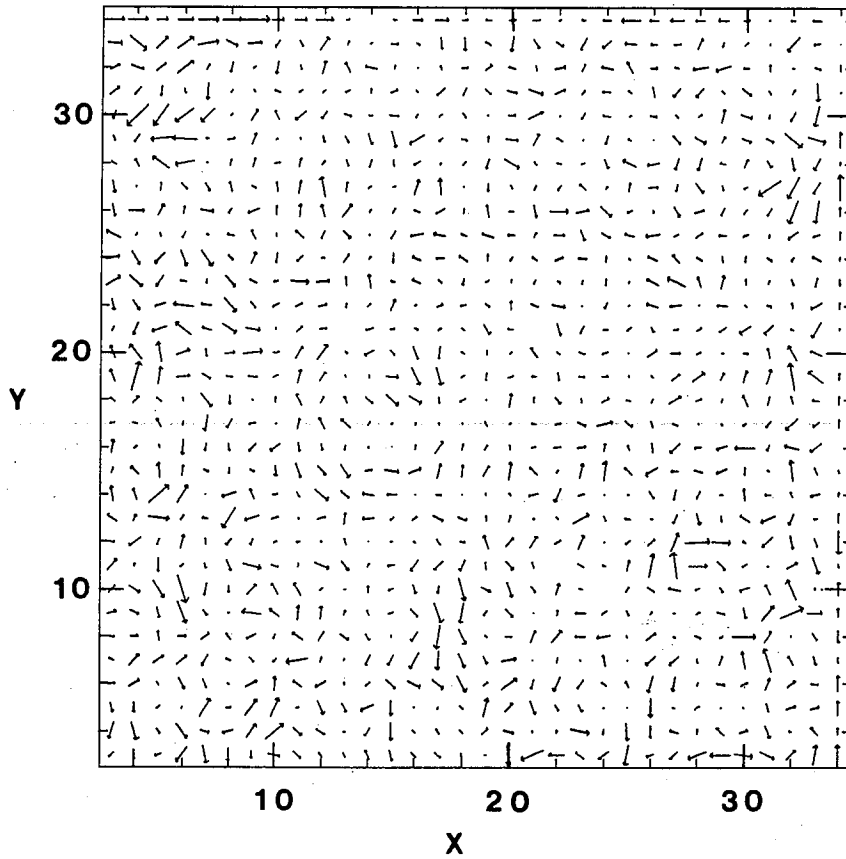


Fig. 2.9. Fluid velocity vectors at various positions in the simulation box at $t = 100 \Delta/C_{s0}$ with $g_0=0$, $\beta_h=0.9$.

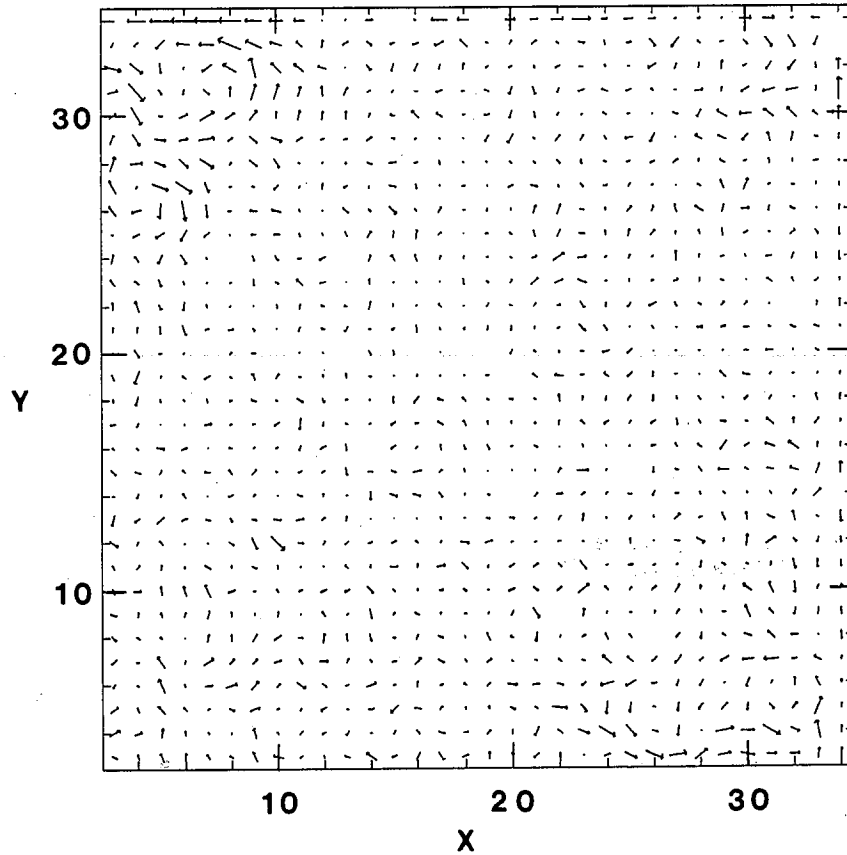


Fig. 2.10. Fluid velocity vectors at various positions in the simulation box at $t = 100 \Delta/C_{s0}$ with $g_0=0.03$, $\beta_h=0.9$.

2.4 Summary

The above results demonstrate the effectiveness of this method in simulating not only interchange instability in a mirror geometry, but also diamagnetic well stabilization of the mode by a fixed, embedded current ring. However, the critical level of current to achieve stabilization is a function of radius and the system may still be unstable in the outer regions of the simulation box, although the majority of the particles can be effectively confined. Because an MHD particle code is used here, the calculation can be carried out much more quickly than with an electromagnetic code. Extending the model to include interactions of the ring and core plasmas, as is needed to demonstrate the Nelson, Lee-Van Dam limit, appears feasible and is the subject of present work. The method to be used involves introducing particles representing the hot electrons and having motions governed by the full dynamics equations. In this way, the hot electron current can vary in time in response to background plasma and magnetic field changes. Introducing full three dimensional effects is also a possibility.

CHAPTER III

CURVATURE-DRIVEN MODES IN EBT

3.1 Introduction

Although the hot electron rings of the EBT may not react on MHD time scales and can in some cases be treated as rigid with respect to such modes, they need not be completely stable in general. For example, the hot electrons themselves represent a plasma of significant pressure gradient confined in a region of unfavorable curvature and should, therefore, be susceptible to some sort of interchange instability. The rings in ELMO, EBT, NBT and the other related devices appeared remarkably stable however.^{23,25,27-30} Thus, part of the history of the theoretical research on plasmas containing an energetic component has been devoted to attempting to explain the stability of the hot electron rings.

Since the curvature drift frequencies of the hot electrons are much larger than typical MHD frequencies and can even exceed the ion cyclotron frequency,²⁵ a more general approach than MHD is needed. The effect of the relatively cold, background plasma on

the hot electron interchange instability was considered in an electrostatic treatment by Krall.²⁴ This mode arises in the same manner as the usual MHD instability, but can be stabilized if the core plasma is sufficiently dense. An analysis of the same instability allowing for the hot electron curvature drift frequency to exceed the ion cyclotron frequency was carried out by Berk.⁵⁸ A self-consistent electromagnetic calculation was later done by Dominguez and Berk.²⁶ They confirmed the results of Krall²⁴ and Berk⁵⁸ and found that the hot electron interchange instability with mode frequency above the ion cyclotron frequency is driven by curvature even if a diamagnetic well is established. As in the case of the more conventional, low frequency interchange mode, it is stabilized by a sufficiently dense core plasma.

Further calculations of the interaction between the ring and the background plasma by Van Dam and Lee⁵⁴ and by Nelson⁵³ showed that even if the hot electron interchange modes are stable, and the background interchange is stabilized according to the criteria of Nelson and Hedrick,⁶ interchange instability can still arise if $\beta_c > 2\Delta_r/R$.

Furthermore, the reversal of the vacuum ∇B in the bad curvature areas can lead to a magnetic instability having the polarization of a compressional Alfvén wave, i.e., with the perturbed magnetic field, $\hat{B}_{\parallel} \parallel B_0$. In EBT such a mode arises if the background density is too high.^{38,59,60} It is stable at

arbitrary densities if $\beta_c > 2\Delta_r/R$,³⁶ but this is just the condition under which the plasma becomes interchange unstable through interactions of the ring and core plasmas!^{53,54}

An analysis of all of these modes as they appear in a Z-pinch model containing a hot electron component, but neglecting finite Larmor radius (FLR) effects, was carried out by Berk et al.³⁶ They determined that for parameters typical of EBT-S and EBT-P, windows of stability could be found. FLR effects could have a significant stabilizing influence on modes with short radial wavelengths, as demonstrated by Berk et al.³⁴ and Hammer and Berk.⁶¹ A full radial treatment^{36,49,61} showed that modes with wavelengths long compared to the annulus width (layer modes) could also be present. These instabilities, however, would be less affected by FLR and are considered to be potentially the most dangerous. Other authors have extended the investigation to include more effects, such as full field-line dependence of the mode amplitude⁶² and more general hot electron distributions.⁶³⁻⁶⁵

In this chapter we will demonstrate, starting with an appropriate variational form derived from the drift kinetic equation, how each of the instabilities discussed here (except the high frequency hot electron interchange) arises, its characteristic growth rate, and under what conditions it is stable (see also Ref. 66). This analytical treatment is valid when the mode frequency is much less than the \sqrt{B} drift frequency. We assume

throughout the chapter that the modes are localized in radius, and we neglect FLR effects. The balance of the chapter will be devoted to numerical solution of the complete equation, valid for arbitrary \sqrt{B} drift frequency, describing the magnetic compressional mode, as well as a brief examination of the background pressure-driven interchange modes. Conclusions regarding our investigation of the magnetic compressional mode are drawn in Sec. 3.3.c.

3.2 Basic Equations

The equations that we will use to describe electromagnetic perturbations arising in tokamak and mirror systems containing energetic particles have been derived by several authors.^{34,44,45,67} Each of these properly treats low-frequency, $\omega \lesssim \omega_d$ (ω_d is magnetic drift frequency), modes appropriate for energetic particle plasmas. Ref. 44 arrives at a kinetic energy principle through the use of adiabatic invariants; Ref. 45 extends their results to include finite frequency and equilibrium electrostatic potential effects. In Refs. 34 and 67, FLR effects are examined in the eikonal limit. The primary result of these calculations is that a new, purely magnetic instability may be present in energetic particle systems,^{36,38,59} giving rise to a stability picture more pessimistic than the Kruskal-Oberman kinetic energy principle.⁶⁸

We expect mode frequencies to be on the order of the energetic particle magnetic drift frequency, but smaller in the case of ballooning modes. Thus, we can assume that the energetic particle bounce frequency ω_b is large relative to the mode frequency and the magnetic drift frequency if $\omega_b > \omega_d$. Their ratio can be written approximately as

$$\frac{\omega_b}{\omega_d} \sim \frac{1}{\ell} \frac{v_{\parallel}}{v_{\perp}} \frac{r}{\rho} \frac{R}{L},$$

where ℓ is the mode number for propagation on a flux surface in the direction perpendicular to the magnetic field. v_{\parallel}/v_{\perp} is the ratio of the parallel to perpendicular velocities for the trapped species; ρ is a typical Larmor radius; r is the radial scale length for the device, and R is the radius of curvature of its magnetic mirror field. L represents the typical length of a bounce orbit. Because of the appearance of r/ρ here, the large bounce frequency approximation is very good for electrons, but less accurate for ions. We will assume that $\omega_b > \omega_d$ here and leave treatment of the opposite limit as a topic of further research (for example, see Refs. 46 and 69).

We will take as our starting point the high-mode-number (i.e., short perpendicular wavelength) limiting expression of the quadratic form as obtained by Antonsen and Lee,⁴⁵ in this limit,

the most unstable modes vary rapidly across the field lines and slowly along them. They arrived at this result by manipulating the linearized guiding center equations of motion derived from the bounce-averaged drift-kinetic equation.⁴⁵ For simplicity, we do not consider here the equilibrium electrostatic potential effects included in their treatment.

The magnetic field displacement vector is written in the form $\xi = \hat{\xi}(\underline{x})\exp[iS(\underline{x})]$, where S is the eikonal with $\hat{b} \cdot \nabla S = 0$; it provides the short wavelength behavior perpendicular to the magnetic field. $\hat{\xi}$ is a slowly varying amplitude; it can be decomposed into two components: $\hat{\xi} = X\hat{b} \times \nabla S + Y\nabla S$. To prevent the compressional term from dominating, we must have $Y \ll X$. Then

$$\begin{aligned} & \frac{1}{2} \int d^3x [\sigma |\nabla S|^2 |\hat{b} \cdot \nabla(XB)|^2 + \tau |\hat{Q}_L|^2 - |XB|^2 \hat{e} \cdot \underline{\kappa} (\frac{\sigma}{\tau} \hat{e} \cdot \hat{v} P_{\perp} + \hat{e} \cdot \hat{v} P_{\parallel}) \\ & - \frac{\rho \omega^2}{B^2} (|XB|^2 |\nabla S|^2 + \frac{|B_{\parallel}|^2}{|\nabla S|^2}) - \sum_{e,i} m \int d^3v \{ |\langle v_{\parallel}^2 \hat{e} \cdot \underline{\kappa}(XB) \\ & + \mu [\hat{Q}_L + B \frac{\sigma}{\tau} \hat{e} \cdot \underline{\kappa}(XB)] \rangle|^2 \frac{\omega - \omega_*}{\omega - \langle \omega_d \rangle} \frac{\partial F}{\partial E} \}] = 0, \end{aligned} \quad (3.1)$$

where

$$\sigma = 1 + \frac{P_{\perp} - P_{\parallel}}{B^2}, \quad \tau = 1 + \frac{1}{B} \frac{\partial P_{\perp}}{\partial B}, \quad \hat{e} = \frac{\hat{b} \times \nabla S}{B}, \quad \kappa = \hat{b} \cdot \nabla \hat{b},$$

$$\hat{b} = \underline{B}/B, \quad \hat{Q}_L = Q_L - \frac{\sigma}{\tau} B \hat{\xi} \cdot \underline{\kappa}, \quad Q_L = B_{\parallel} + \hat{\xi} \cdot \nabla B,$$

$$B_{\parallel} = \hat{b} \cdot \nabla \times (\hat{\xi} \times B), \quad \hat{\nabla} = \nabla - \nabla B \frac{\partial}{\partial B}, \quad \rho = m_i n_i, \quad \omega_* = \frac{B}{\Omega} \frac{\hat{e} \cdot \nabla F}{\partial F / \partial E},$$

$$\omega_d = -\frac{B}{\Omega} (\nu_{\parallel}^2 \hat{e} \cdot \underline{\kappa} + \mu \hat{e} \cdot \nabla B), \quad \mu = \frac{\nu_{\perp}^2}{2B}, \quad E = \mu B + \nu_{\parallel}^2,$$

$$\langle \dots \rangle \equiv \frac{\int d\ell (\dots) / |\nu_{\parallel}|}{\int d\ell / |\nu_{\parallel}|}, \quad d^3 v = \frac{dE d\mu B}{|\nu_{\parallel}|},$$

$\Omega = qB/m =$ cyclotron frequency, m and q are the particle mass and charge, respectively.

To get a form appropriate for a three component plasma such as in EBT, the kinetic term for the core electrons and ions is replaced by the conventional form in which $\omega \gg \omega_*, \omega_d$. We also make the change of variables, $\varphi \equiv -\omega X B$ to obtain

$$\frac{1}{2} \int d^3 x (|B_{\parallel}|^2 (\tau + \beta_c - \frac{\omega^2}{k_{\perp}^2 v_A^2}) + \frac{B}{\omega} (\varphi^* B_{\parallel} + \varphi B_{\parallel}^*) [\hat{e} \cdot \hat{\nabla} P_{lh} / B^2 + \hat{e} \cdot \nabla (\frac{P_c}{B^2})])$$

$$+ \frac{\sigma k_{\perp}^2}{\omega^2} |\hat{b} \cdot \nabla \varphi|^2 - \frac{k_{\perp}^2}{v_A^2} |\varphi|^2 - |\varphi|^2 \frac{B}{\omega^2} \{ \hat{e} \cdot \nabla B [\hat{e} \cdot \hat{\nabla} P_{lh} / B^2 + \hat{e} \cdot \nabla (\frac{P_c}{B^2})] \}$$

$$\begin{aligned}
& + \hat{e} \cdot \underline{\kappa} \left[\hat{e} \cdot \underline{\hat{V}} P_{\parallel h} / B + \hat{e} \cdot \underline{\nabla} \left(\frac{P_c}{B} \right) \right] - m_h \int d^3 v \left(\left| \left\langle \frac{q}{m_h} \frac{\omega_d}{\omega} \varphi \right. \right. \right. \\
& \left. \left. \left. + \mu B_{\parallel} \right| \right)^2 \frac{\omega - \omega_*}{\omega - \langle \omega_d \rangle} \frac{\partial F_h}{\partial E} \right) = 0, \tag{3.2}
\end{aligned}$$

where $\beta_c = 2P_c/B^2$, $k_{\perp} = |\underline{\nabla} S|$, $V_A^2 = B^2/\rho$, the subscript c refers to the core plasma with $P_c = P_{e,c} + P_{i,c}$; the subscript h refers to the energetic electrons. φ represents the perturbed electrostatic potential, and B_{\parallel} is proportional to the perturbed parallel magnetic field. A pair of coupled eigenmode equations can be obtained by varying this equation with respect to the complex conjugate variables φ^* and B_{\parallel}^* . These are the equations we will solve numerically to describe the magnetic compressional and interchange modes.

We first follow the analytic treatment outlined in Refs. 34 and 66 valid for $\omega \ll \omega_{dh}$ (see also Ref. 46). This will allow us to identify the magnetic compressional and interchange instabilities in addition to providing approximate analytic solutions to the complete integro-differential system. We assume $\beta \ll 1$, $\beta_h \gg \beta_c$, $\beta R/\Delta_r \gg 1$ (R is the field line radius of curvature, Δ_r is the pressure gradient scale length), expand the resonant denominator,

$$\frac{1}{\omega - \langle \omega_d \rangle} \approx \frac{-1}{\mu \frac{m}{q} \langle \hat{e} \cdot \nabla P_{1h} / B \rangle} \left(1 + \frac{\omega + \frac{m}{q} \langle (v_{\parallel}^2 + \sigma \mu B) \hat{e} \cdot \kappa \rangle - \mu \frac{m}{q} \langle \hat{e} \cdot \nabla P_c / B \rangle}{\mu \frac{m}{q} \langle \hat{e} \cdot \nabla P_{1h} / B \rangle} \right), \quad (3.3)$$

and write

$$B_{\parallel} = -\frac{B}{\omega} \varphi \hat{e} \cdot \nabla \left(\frac{P_c}{B^2} \right) + \tilde{B}_1. \quad (3.4)$$

Upon varying Eq. (3.2) with respect to B_{\parallel}^* and using these expressions, we obtain

$$\begin{aligned} \tilde{B}_1 - m_h \int d^3 v \mu \left(\frac{\hat{e} \cdot \nabla F_h \langle \tilde{B}_1 \rangle}{\langle \hat{e} \cdot \nabla P_{1h} / B \rangle} - \mu \frac{\partial F_h}{\partial \mu} \frac{\hat{e} \cdot \nabla B}{\hat{e} \cdot \nabla P_{1h}} \tilde{B}_1 \right) &= \left(\frac{\omega^2}{k_{\perp}^2 v_A^2} - \beta_c \right) \tilde{B}_1 \\ &+ \int d^3 v \frac{m_h \hat{e} \cdot \nabla F_h \langle \tilde{B}_1 \rangle}{\langle \hat{e} \cdot \nabla P_{1h} / B \rangle} \left[\frac{\omega \frac{q_h}{m_h} + \langle (v_{\parallel}^2 + \sigma \mu B) \hat{e} \cdot \kappa \rangle - \mu \langle \hat{e} \cdot \nabla P_c / B \rangle}{\langle \hat{e} \cdot \nabla P_{1h} / B \rangle} \right] \\ &- q_h \omega \int d^3 v \mu \frac{\partial F_h}{\partial E} \frac{\langle \tilde{B}_1 \rangle}{\langle \hat{e} \cdot \nabla P_{1h} / B \rangle} + m_h \int d^3 v \mu^2 \frac{\partial F_h}{\partial \mu} \tilde{B}_1 \left[\frac{B \sigma \hat{e} \cdot \kappa - (\hat{e} \cdot \nabla P_c) / B}{\hat{e} \cdot \nabla P_{1h}} \right] \\ &- \frac{m_h}{\omega} \varphi \int d^3 v \left[\frac{\mu \hat{e} \cdot \nabla F_h \langle \hat{B} \cdot \nabla (P_c / B^2) \rangle}{\langle \hat{e} \cdot \nabla P_{1h} / B \rangle} + \mu^2 \frac{\partial F_h}{\partial \mu} \hat{e} \cdot \nabla \left(\frac{P_c}{B^2} \right) \right] \end{aligned}$$

$$+ q_h \varphi \int d^3v \left(-\mu \frac{\partial F_h}{\partial E} + \frac{\hat{e} \cdot \nabla F_h}{\langle \hat{e} \cdot \nabla P_{\perp h} / B \rangle} \right); \quad (3.5)$$

φ has been assumed to be constant over the hot electron region. This is essentially the perpendicular component of Ampere's Law. We expect φ to vary only slightly over the hot electron region so that the field line bending term in Eq. (3.1) can be balanced by the other terms.³⁴

The left-hand side of this equation vanishes if $\tilde{B}_1 = C(\psi) \hat{e} \cdot \nabla P_{\perp h} / B$. After making this substitution, we multiply the entire equation by $\hat{e} \cdot \nabla P_{\perp h} / B^2$ and integrate over the hot electron region to obtain

$$\begin{aligned} C \int \frac{ds}{B} & \left[- \left(\frac{\hat{e} \cdot \nabla P_{\perp h}}{B} \right)^2 \frac{\omega^2}{k_{\perp}^2 v_A^2} + (\hat{e} \cdot \nabla P_{\perp h}) \hat{e} \cdot \nabla \left(\frac{P_c}{B^2} \right) - \omega q_h B \hat{e} \cdot \nabla \left(\frac{n_h}{B} \right) \right. \\ & \left. - (\hat{e} \cdot \kappa) \hat{e} \cdot \nabla (P_{\parallel h} + P_{\perp h}) \right] \\ & = \frac{-\varphi}{\omega} \int \frac{ds}{B} \left[\hat{e} \cdot \nabla \left(\frac{P_c}{B^2} \right) \hat{e} \cdot \nabla P_{\perp h} - \omega q_h B \hat{e} \cdot \nabla \left(\frac{n_h}{B} \right) \right]. \end{aligned} \quad (3.6)$$

Next, we consider the equation obtained by varying Eq. (3.2) with respect to φ^* . Again, the resonant denominator is expanded, the above form for B_{\parallel} is inserted, and φ is assumed constant over the hot electron region. Thus,

$$\begin{aligned}
& \underline{\mathbf{B}} \cdot \underline{\nabla} \left(\frac{\sigma k_{\perp}^2}{B^2} \underline{\mathbf{B}} \cdot \underline{\nabla} \varphi \right) + \frac{\omega^2 k_{\perp}^2}{V_A^2} \varphi + 2(\hat{\mathbf{e}} \cdot \underline{\kappa}) \hat{\mathbf{e}} \cdot \underline{\nabla} P_c \varphi \\
& = \left[(\hat{\mathbf{e}} \cdot \underline{\nabla} P_{\perp h}) \hat{\mathbf{e}} \cdot \underline{\nabla} \left(\frac{P_c}{B^2} \right) - q_h \omega B \hat{\mathbf{e}} \cdot \underline{\nabla} \left(\frac{n_h}{B} \right) \right] \varphi \\
& + \omega \left[(\hat{\mathbf{e}} \cdot \underline{\nabla} P_{\perp h}) \hat{\mathbf{e}} \cdot \underline{\nabla} \left(\frac{P_c}{B^2} \right) - q_h \omega B \hat{\mathbf{e}} \cdot \underline{\nabla} \left(\frac{n_h}{B} \right) \right] C \\
& - \omega^2 \int d^3 v \left(\frac{m_h}{\omega} \left[(\mu B_{\parallel} + \frac{q_h \varphi}{m_h}) - \frac{\omega_d}{\langle \omega_d \rangle} (\mu \langle B_{\parallel} \rangle + \frac{q_h \varphi}{m_h}) \right] \hat{\mathbf{e}} \cdot \underline{\nabla} F_h \right. \\
& \left. + C q_h \hat{\mathbf{e}} \cdot \underline{\nabla} F_h \left(\frac{\hat{\mathbf{e}} \cdot \underline{\nabla} P_{\perp h} / B - \langle \hat{\mathbf{e}} \cdot \underline{\nabla} P_{\perp h} / B \rangle}{\langle \hat{\mathbf{e}} \cdot \underline{\nabla} P_{\perp h} / B \rangle} \right) \right]. \tag{3.7}
\end{aligned}$$

Notice that the kinetic term vanishes if the equation is multiplied by $1/B$ and integrated over the hot electron region.

We can now obtain a simplified quadratic form by multiplying Eq. (3.7) by φ^*/B and integrating over the entire mirror cell,

$$\begin{aligned}
& - \int_{-L/2}^{L/2} \frac{ds}{B} (\sigma k_{\perp}^2 \left| \frac{d\varphi}{ds} \right|^2) + \int_{-L/2}^{L/2} \frac{ds}{B} \left[\frac{\omega^2 k_{\perp}^2}{V_A^2} + 2(\hat{\mathbf{e}} \cdot \underline{\kappa}) \hat{\mathbf{e}} \cdot \underline{\nabla} P_c \right] |\varphi|^2 \\
& = \langle M |\varphi|^2 \rangle - \frac{|\langle M \varphi \rangle|^2}{D}, \tag{3.8}
\end{aligned}$$

where

$$\begin{aligned}
 D \equiv & -(\hat{e} \cdot \nabla P_{\perp h} / B)^2 \frac{\omega^2}{k_{\perp}^2 V_A^2} + (\hat{e} \cdot \nabla P_{\perp h}) \hat{e} \cdot \nabla \left(\frac{P_c}{B^2} \right) \\
 & - \omega q_h B \hat{e} \cdot \nabla \left(\frac{n_h}{B} \right) - (\hat{e} \cdot \kappa) \hat{e} \cdot \nabla (P_{\perp h} + P_{\parallel h}), \\
 M \equiv & (\hat{e} \cdot \nabla P_{\perp h}) \hat{e} \cdot \nabla \left(\frac{P_c}{B^2} \right) - q_h \omega B \hat{e} \cdot \nabla \left(\frac{n_h}{B} \right),
 \end{aligned}$$

and now $\langle \alpha \rangle \equiv \int ds \alpha / B$. Some of the effects of φ varying along the field line have been included in this particular form. Eq. (3.7) is much easier to solve numerically than the full integro-differential equations and will be used to check the complete solutions in the limit in which Eq. (3.8) is valid, $\omega/\omega_d \ll 1$. However, to obtain an analytic dispersion relation, we assume φ is constant along the field line and $d\varphi/ds = 0$ in Eq. (3.8). As mentioned above, we do not expect φ to vary a great deal over the hot electron region so that the field line bending term can be balanced by the other contributions to the equation.

$$\int_{-L/2}^{L/2} \frac{ds}{B} \left[\frac{\omega^2 k_{\perp}^2}{V_A^2} + 2(\hat{e} \cdot \kappa)(\hat{e} \cdot \nabla P_c) \right] = - \frac{\langle M \rangle \langle N \rangle}{\langle D \rangle}, \quad (3.9)$$

with

$$N \equiv (\hat{e} \cdot \nabla P_{\perp h} / B)^2 \frac{\omega^2}{k_{\perp}^2 V_A^2} + (\hat{e} \cdot \kappa) \hat{e} \cdot \nabla (P_{\perp h} + P_{\parallel h}).$$

From this equation, we can get growth rates and marginal stability criteria for the magnetic compressional mode,^{36,38,59} the low-frequency hot electron interchange mode,^{24,25,58} the background pressure-driven interchange mode,⁶ and the interacting pressure-driven mode.^{53,54}

First, we examine the magnetic compressional mode by setting $\langle D \rangle = 0$. We can write this in the form

$$\omega^2 / \overline{k_{\perp}^2 V_A^2} + \omega / \overline{\omega_{db}} + \overline{D_1} = 0, \quad (3.10)$$

where we have defined

$$1 / \overline{k_{\perp}^2 V_A^2} \equiv \frac{\int \frac{ds}{B} \left(\frac{\hat{e} \cdot \nabla P_{\perp h}}{B} \right)^2 / k_{\perp}^2 V_A^2}{\int \frac{ds}{B} \left(\frac{\hat{e} \cdot \nabla P_{\perp h}}{B} \right)^2},$$

$$1 / \overline{\omega_{db}} \equiv \frac{\int \frac{ds}{B} q_h B \hat{e} \cdot \nabla \left(\frac{n_h}{B} \right)}{\int \frac{ds}{B} \left(\frac{\hat{e} \cdot \nabla P_{\perp h}}{B} \right)^2}.$$

$$\overline{\overline{D}}_1 \equiv \frac{\int \frac{ds}{B} [(\hat{e} \cdot \underline{\kappa}) \hat{e} \cdot \underline{\nabla} (P_{\perp h} + P_{\parallel h}) - (\hat{e} \cdot \underline{\nabla} P_{\perp h}) \hat{e} \cdot \underline{\nabla} (\frac{P_c}{B^2})]}{\int \frac{ds}{B} (\frac{\hat{e} \cdot \underline{\nabla} P_{\perp h}}{B})^2}$$

The mode is far from stability when $\omega/\omega_{db} \ll 1$; that is, the hot electrons are very energetic. In this case, the growth rate is given by

$$\omega^2 = - \overline{\overline{k}}_{\perp}^2 \overline{\overline{V}}_A^2 \overline{\overline{D}}_1. \quad (3.11)$$

However, if $(1/\omega_{db})^2 > 4\overline{\overline{D}}_1/\overline{\overline{k}}_{\perp}^2 \overline{\overline{V}}_A^2$, the mode is stable. The right-hand side of this inequality scales with the core density through V_A . Thus, we can have instability if the core density is too large. Also, note that if

$$\hat{e} \cdot \underline{\nabla} (\frac{P_c}{B^2}) > (\hat{e} \cdot \underline{\kappa}) \frac{\hat{e} \cdot \underline{\nabla} (P_{\perp h} + P_{\parallel h})}{\hat{e} \cdot \underline{\nabla} P_{\perp h}},$$

$\overline{\overline{D}}_1 < 0$ and there is no instability. But, as will be seen later, this is the same condition to destabilize the interacting pressure-driven interchange (the Nelson, Lee - Van Dam limit). An approximate criterion is that $\beta_c R/2\Delta_r > 1 + P'_{\parallel h}/P'_{\perp h}$ ($P' \equiv \hat{e} \cdot \underline{\nabla} P$).

Now, we consider the various interchange modes by assuming $\omega \ll k_{\perp} V_A (\Delta_b/R)^{1/2}$ (Δ_b is the radial scale length for the magnetic field) in Eq. (3.9), and thereby neglect $\omega^2/k_{\perp}^2 V_A^2$ in N and D. We can then write

$$\omega^2 + \Lambda = 0, \quad (3.12)$$

$$\Lambda \equiv \frac{\langle A \rangle}{\langle k_{\perp}^2 / V_A^2 \rangle} + \frac{\langle M \rangle \langle N(\omega=0) \rangle}{\langle W \rangle \langle k_{\perp}^2 / V_A^2 \rangle},$$

$$A \equiv 2(\hat{e} \cdot \underline{\kappa}) \hat{e} \cdot \underline{\nabla} P_c,$$

$$W \equiv (\hat{e} \cdot \underline{\nabla} P_{\perp h}) \hat{e} \cdot \underline{\nabla} \left(\frac{P_c}{B^2} \right) - \omega q_h B \hat{e} \cdot \underline{\nabla} \left(\frac{n_h}{B} \right) - (\hat{e} \cdot \underline{\kappa}) \hat{e} \cdot \underline{\nabla} (P_{\perp h} + P_{\parallel h}).$$

The low frequency hot electron interchange instability, analogous to the conventional MHD mode, can be obtained if we consider Eq. (3.12) in the limit $P_c \rightarrow 0$. It is stable if

$$\int \frac{ds}{B} (\hat{e} \cdot \underline{\kappa}) \hat{e} \cdot \underline{\nabla} (P_{\perp h} + P_{\parallel h}) > \frac{4 \left[\int \frac{ds}{B} q_h B \hat{e} \cdot \underline{\nabla} \left(\frac{n_h}{B} \right) \right]^2}{m_i \int ds \frac{k_{\perp}^2 n_i}{B^3}}; \quad (3.13)$$

that is, if the core plasma is dense enough. In the opposite limit, Λ becomes completely independent of ω , and we calculate a growth rate

$$\omega^2 = - \frac{\int \frac{ds}{B} (\hat{e} \cdot \underline{\kappa}) \hat{e} \cdot \underline{\nabla} (P_{\perp h} + P_{\parallel h})}{m_i \int ds \frac{k_{\perp}^2 n_i}{B^3}} \quad (3.14)$$

In order to examine the noninteracting background pressure-driven interchange mode, we assume that the hot electron interchange is far from instability [this requirement, Eq. (3.13), is also known as the decoupling condition]. Thus, Λ is again independent of ω . By noninteracting we mean that

$$\hat{e} \cdot \underline{\nabla} \left(\frac{P_c}{B^2} \right) \ll \hat{e} \cdot \underline{\kappa} \left(1 + \frac{\hat{e} \cdot \underline{\nabla} P_{\parallel h}}{\hat{e} \cdot \underline{\nabla} P_{\perp h}} \right);$$

in other words, the curvature contribution dominates the other terms in W . This mode is unstable in the limit that $\beta_h \rightarrow 0$, with a growth rate

$$\omega^2 = \frac{-2 \int \frac{ds}{B} (\hat{e} \cdot \underline{\kappa}) \hat{e} \cdot \underline{\nabla} P_c}{m_i \int ds \frac{k_{\perp}^2 n_i}{B^3}} \quad (3.15)$$

With finite β_h , we can obtain stability, $\Lambda < 0$, if

$$\begin{aligned} & \{ [2\langle(\hat{e}\cdot\kappa)\hat{e}\cdot\nabla P_c\rangle + \langle(\hat{e}\cdot\kappa)\hat{e}\cdot\nabla(P_{\perp h} + P_{\parallel h})\rangle] \langle(\hat{e}\cdot\nabla P_{\perp h})\hat{e}\cdot\nabla(\frac{P_c}{B^2})\rangle \\ & - 2\langle(\hat{e}\cdot\kappa)\hat{e}\cdot\nabla P_c\rangle \langle(\hat{e}\cdot\kappa)\hat{e}\cdot\nabla(P_{\perp h} + P_{\parallel h})\rangle \} \\ & \times [\langle(\hat{e}\cdot\nabla P_{\perp h})\hat{e}\cdot\nabla(\frac{P_c}{B^2}) - (\hat{e}\cdot\kappa)\hat{e}\cdot\nabla(P_{\perp h} + P_{\parallel h})\rangle]^{-1} < 0 \end{aligned} \quad (3.16)$$

Using the notation defined previously, this condition becomes approximately

$$\frac{\beta_{\perp h} + 2\beta_c - \frac{4\Delta_r}{R}}{\frac{\beta_c R}{2\Delta_r} - 1} < 0. \quad (3.17)$$

Thus, the noninteracting interchange is stable if

$$\beta_{\perp h} > \frac{4\Delta_r}{R} - 2\beta_c. \quad (3.18)$$

This is the familiar diamagnetic well condition discussed in Refs. 6 and 36. But, if $\beta_c R/2\Delta_r > 1$, Eq. (3.17) cannot be satisfied for any $\beta_{\perp h}$. At this point the core pressure is large enough to interact with the hot electron rings and offset their

stabilizing effect. The more precise criterion is that the denominator of Eq. (3.16) be positive,

$$\hat{e} \cdot \nabla \left(\frac{P_c}{B^2} \right) > \hat{e} \cdot \kappa \left(1 + \frac{\hat{e} \cdot \nabla P_{\parallel h}}{\hat{e} \cdot \nabla P_{\perp h}} \right); \quad (3.19)$$

this is the Nelson, Lee - Van Dam limit.^{53,54} When this mode is far from stability, we observe a growth rate

$$\omega^2 = - \frac{\langle \hat{e} \cdot \kappa \hat{e} \cdot \nabla (P_{\perp h} + P_{\parallel h} + 2P_c) \rangle}{\int \frac{ds}{B} \frac{k_{\perp}^2}{v_A^2}}; \quad (3.20)$$

now ω^2 scales as the total plasma pressure.

As mentioned previously, the condition to stabilize this mode is exactly the opposite of that needed to stabilize the magnetic compressional mode. However, we have neglected FLR effects. The analysis of Ref. 34 treats the case of finite but small Larmor radius with the result that both of these modes are stable if the FLR parameter is large enough.

3.3 Magnetic Compressional Mode

We now consider the numerical solution of the integral equation describing the magnetic compressional mode for a single cell of an axisymmetric multi-mirror system. In general, the coupled equations obtained from Eq. (3.2) by variations with respect to B_{\parallel}^* and φ^* must be solved simultaneously. Because of the large difference in frequency between the magnetic compressional mode and the interchange mode arising out of the φ equation, we do not expect this coupling to strongly affect the magnetic compressional mode. Thus, we solve here only one equation in B_{\parallel} and will study the coupled system in Sec. 3.4. A relatively simple solution, Eq. (3.10), arises in a deep diamagnetic well. However, for a moderate well, the simple solution is unjustified and a numerical solution of the integral equation is necessary. We find that smaller pressure gradients are required for stability than are needed with the simple theory. Study of the solutions leads one to believe that a description of the mode with the assumption that $B_{\parallel} = [C(\psi)/B]dP_{\perp h}/d\psi$ is accurate for growth rates if the subsequent integrals are not approximated further.

In Sec. 3.3.a, the numerical model is developed from the governing equations. Section 3.3.b presents some eigenvalues and eigenfunctions obtained from its solution. Finally, a summary of these results is given in Sec. 3.3.c.

3.3.a Numerical Model

Varying Eq. (3.2) with respect to B_{\parallel}^* and neglecting the coupling to the φ equation, we find

$$\begin{aligned}
 B_{\parallel} \left(1 + \frac{1}{B} \frac{\partial P_{\perp h}}{\partial B} + \beta_c - \frac{\omega^2}{k_{\perp}^2 v_A^2} \right) \\
 = m_h \int \frac{dE d\mu B}{|v_{\parallel}|} \mu^2 \left[\frac{\omega \frac{\partial F_h}{\partial E}(E, \mu, \psi) + \frac{m_h \ell}{q_h} \frac{\partial F_h}{\partial \psi}}{\omega - \langle \omega_d \rangle} \right] \langle B_{\parallel} \rangle, \quad (3.21)
 \end{aligned}$$

where

$$\langle \omega_d \rangle = \frac{\ell m_h}{q_h} \left[\mu \left\langle \frac{dB}{d\psi} \right\rangle + \left\langle \frac{v_{\parallel}^2 \kappa}{rB} \right\rangle \right] \equiv \langle \omega_{bh} \rangle + \langle \omega_{\kappa h} \rangle,$$

$$\langle \dots \rangle \equiv \frac{\int d\ell (\dots) / |v_{\parallel}|}{\int d\ell / |v_{\parallel}|},$$

$$\kappa = |(\hat{b} \cdot \nabla) \hat{b}|,$$

$$P_{\perp h} = m_h \int \frac{dE d\mu B^2}{|v_{\parallel}|} \mu F_h(E, \mu, \psi),$$

$$k_{\perp}^2 = \frac{\ell^2}{r^2} + \left(\frac{\partial S}{\partial \psi} \right)^2 |\nabla \psi|^2,$$

$$\nabla \psi \times \hat{\vartheta} = r \hat{B},$$

$$\frac{d}{d\psi} \equiv \frac{\nabla\psi \cdot \nabla}{|\nabla\psi|^2} \equiv \frac{\partial}{\partial\psi} \Big|_B + \frac{dB}{d\psi} \frac{\partial}{\partial B} \Big|_\psi.$$

Note that the core plasma is assumed to be isotropic.

In the limit that $|(1/B)dP_{\perp h}/d\psi| \gg |\kappa/r|$, this equation can be readily solved. In fact, to lowest order in κ , $B_{\parallel} \cong [C(\psi)/B]dP_{\perp h}/d\psi$. Expanding the resonant denominator of Eq. (3.21) with $\omega \ll \omega_{bh}, \omega_{\kappa h}$ leads to an equivalent expression for Eq. (3.10),

$$\int_0^{L/2} \frac{ds}{B} \left[\frac{dP_{\perp h}}{d\psi} \frac{d}{d\psi} \left(\frac{P_c}{B^2} \right) + \frac{q_h \omega B}{\ell} \frac{d}{d\psi} \left(\frac{n_h}{B} \right) - \frac{\kappa}{rB} \frac{d}{d\psi} (P_{\perp h} + P_{\parallel h}) - \frac{\omega^2}{k_{\perp}^2 v_A^2} \left(\frac{1}{B} \frac{dP_{\perp h}}{d\psi} \right)^2 \right] = 0. \quad (3.22)$$

The integral is carried out from the midplane of the cell to the mirror throat.

Of course, when $|(1/B)dP_{\perp h}/d\psi| \cong |\kappa/r|$, this solution is inappropriate and we must solve the equation numerically. For this purpose, we expand B_{\parallel} in a complete set of functions, f_n , of s , the length along a field line from the midplane,

$$B_{\parallel}(s) = \sum_{n=1}^{\infty} a_n f_n(s).$$

The solution yields a value for ω and gives the constant coefficients a_n .

When there is no coupling to the perturbed electrostatic potential, as is the case here, B_{\parallel} vanishes outside of the hot electron region. We assume B_{\parallel} to be even in s ; the symmetry of the system allows eigenfunctions that are even or odd. Then, it is reasonable to choose even functions that go through zero at the edge of the annulus and vanish outside of it:

$$f_n(s) = \begin{cases} \cos\left[\pi \frac{(n - 1/2)s}{s_c}\right] & 0 \leq s \leq s_c \\ 0 & s_c \leq s \leq L/2, \end{cases} \quad (3.23)$$

where $B(s_c) = B_c$. For comparison purposes, two other representations of B_{\parallel} are investigated. The single term representation,

$$B_{\parallel} = a_0 \frac{1}{B} \frac{dP_{\perp h}}{d\psi},$$

is clearly valid when $\omega/\langle\omega_d\rangle \ll 1$, since $B_{\parallel} \cong [C(\psi)/B] dP_{\perp h}/d\psi$ in that case. We will assess the accuracy of this approach for larger values of $\omega/\langle\omega_d\rangle$.

Also, a Gaussian test function,

$$B_{\parallel} = \exp\left[\frac{-(s - s_0)^2}{\Delta_s^2}\right] + \exp\left[\frac{-(s + s_0)^2}{\Delta_s^2}\right] \quad (3.24)$$

will be employed. s_0 is fixed and Δ_s , a complex number in general, is varied so as to minimize the quadratic form.

In order to obtain the eigenvalue ω we first multiply Eq. (3.21) by $B_{\parallel}/B(s)$ and integrate along the field line. Using the above expansion for B_{\parallel} , we then have

$$\sum_{k,j=1}^{\infty} a_k a_j Q_{kj}(\omega) = 0,$$

where

$$Q_{kj}(\omega) = \int_0^{L/2} \frac{ds}{B} [f_k(s) f_j(s) (1 + \frac{1}{B} \frac{\partial P_{\perp h}}{\partial B} + \beta_c - \frac{\omega^2}{k_{\perp}^2 v_A^2})] \\ - m_h \int_0^{L/2} \frac{ds}{B} \int \frac{dE d\mu}{|v_{\parallel}|} \mu^2 B \frac{(\omega \frac{\partial F_h}{\partial E} + \frac{m_h \ell}{q_h} \frac{\partial F_h}{\partial \psi})}{\omega - \langle \omega_d \rangle} \langle f_k \rangle \langle f_j \rangle.$$

Varying this expression with respect to a_i , we find

$$\sum_{j=1}^{\infty} a_j Q_{ij}(\omega) = 0,$$

for $i=1, \infty$. Then, ω is determined by requiring that these equations have a nontrivial solution. That is,

$$\det|Q_{ij}(\omega)| = 0. \quad (3.25)$$

Specifically, we take

$$F_h = \begin{cases} \frac{4\hat{P}_{\perp h}}{m_h \sqrt{2\pi} T^{7/2}} \frac{\left[1 - \frac{(\psi - \psi_0)^2}{\Delta\psi^2}\right] (\mu B_c - E) e^{-E/t}}{\left(1 - \frac{B_{\min}}{B_c}\right)^{3/2} \left(1 + \frac{4B_c}{B_{\min}}\right)} & \frac{E}{B_c} < \mu < \frac{E}{B_{\min}} \\ 0 & 0 < \mu < \frac{E}{B_c} \end{cases} \quad (3.26)$$

where $B_{\min} \equiv \min[B(s)] < B_c < B_{\max} \equiv \max[B(s)]$. Doing the appropriate integrals, the hot electron density and pressure can be obtained:

$$n_h = \frac{2\hat{P}_{\perp h}}{m_h T} \left[1 - \frac{(\psi - \psi_0)^2}{\Delta\psi^2}\right] \frac{B_c}{B} \frac{(1 - B/B_c)^{3/2}}{(1 - B_{\min}/B_c)^{3/2} (1 + 4B_c/B_{\min})}$$

$$\frac{1}{B} \frac{\partial n_h}{\partial B} = \frac{-2\hat{P}_{\perp h}}{m_h T} \left[1 - \frac{(\psi - \psi_0)^2}{\Delta\psi^2} \right] \frac{B_c}{B^3} \frac{(1 - B/B_c)^{1/2} (1 + \frac{1}{2} B/B_c)}{(1 - B_{\min}/B_c)^{3/2} (1 + 4B_c/B_{\min})}$$

$$P_{\perp h} = \hat{P}_{\perp h} \left[1 - \frac{(\psi - \psi_0)^2}{\Delta\psi^2} \right] \frac{(1 - B/B_c)^{3/2} (1 + 4B_c/B)}{(1 - B_{\min}/B_c)^{3/2} (1 + 4B_c/B_{\min})}$$

$$P_{\parallel h} = 2\hat{P}_{\perp h} \left[1 - \frac{(\psi - \psi_0)^2}{\Delta\psi^2} \right] \frac{B_c}{B} \frac{(1 - B/B_c)^{5/2}}{(1 - B_{\min}/B_c)^{3/2} (1 + 4B_c/B_{\min})}$$

$$\frac{1}{B} \frac{\partial P_{\perp h}}{\partial B} = -2\hat{P}_{\perp h} \left[1 - \frac{(\psi - \psi_0)^2}{\Delta\psi^2} \right] \frac{(1 - B/B_c)^{1/2} (\frac{3}{4} B^2 + BB_c + 2B_c^2)}{B_c B^3 (1 - B_{\min}/B_c)^{3/2} (1 + 4B_c/B_{\min})}$$

$$\frac{1}{B} \frac{\partial P_{\parallel h}}{\partial B} = -2\hat{P}_{\perp h} \left[1 - \frac{(\psi - \psi_0)^2}{\Delta\psi^2} \right] \frac{B_c}{B^3} \frac{(1 - B/B_c)^{3/2} (1 + \frac{3}{2} B/B_c)}{(1 - B_{\min}/B_c)^{3/2} (1 + 4B_c/B_{\min})}$$

The core pressure is assumed to be constant along a field line with the radial dependence written as

$$P_c(\psi) = \begin{cases} \hat{P}_c \left[1 - \frac{(\psi - \psi_0)^2}{\Delta\psi^2} \right] & \psi > \psi_0 \\ \hat{P}_c & \psi < \psi_0 \end{cases}$$

Finally, we express the vacuum magnetic field for a long-thin mirror cell as a function of s in the form

$$B_v(s) = B_{v\max} \left[(1 - 2\varepsilon) + \varepsilon \left(1 - \cos \frac{2\pi s}{L} \right) \right] \quad (3.27)$$

If $\underline{r}(s)$ describes the position vector of a point on a field line, the curvature is given by $\kappa = d^2 \underline{r} / ds^2$. In a cylindrically symmetric geometry, (r, ϑ, z) , this becomes $\kappa = d^2 r / ds^2 \hat{r} + d^2 z / ds^2 \hat{z}$. We will assume a long-thin system, $r/L \ll 1$, and note that $z = s + \vartheta(r/L)^2$. So, it is reasonable to take

$$|\kappa| \cong \frac{d^2 r}{ds^2} \quad (3.28)$$

Furthermore, the long-thin equilibrium condition can be written as

$$B^2(s) = B_v^2(s) - 2[P_{\perp h}(s) + P_c]$$

This implies that the finite pressure equilibrium does not change the curvature much from its vacuum value. Then, the magnetic flux is given by

$$\psi = \frac{B_v r^2}{2} + \mathcal{O}(\beta_h \Delta\psi).$$

By conservation of flux along a field line, we can then infer that

$$r^2(s) \cong r_0^2 B_{vmin} / B_v(s), \quad (3.29)$$

where $r_0 = r(s=0)$ and $B_{vmin} = B_v(s=0)$. Thus, Eqs. (3.27)-(3.29) yield

$$\frac{\kappa}{r} \cong - \frac{\epsilon 4\pi^2}{2L^2(1-2\epsilon)} \left(\frac{r}{r_0}\right)^2 \left[\cos \frac{2\pi s}{L} - \frac{3}{2} \frac{\epsilon}{1-2\epsilon} \left(\frac{r}{r_0}\right)^2 \sin^2 \frac{2\pi s}{L} \right]. \quad (3.30)$$

Using perpendicular pressure balance, these quantities give a value for the radial gradient of the field strength,

$$\frac{dB}{d\psi} = \frac{-\frac{1}{B} \frac{\partial P_{\perp h}}{\partial \psi} \Big|_B - \frac{1}{B} \frac{\partial P_c}{\partial \psi} \Big|_B + \frac{\kappa}{r} \left(1 + \frac{P_{\perp h} - P_{\parallel h}}{B^2}\right)}{1 + \frac{1}{B} \frac{\partial P_{\perp h}}{\partial B}}$$

Finally, the expression for k_1^2 given below Eq. (3.21) can now be written as

$$k_1^2(s) = \frac{\ell^2 B_v(s)}{r_0^2 B_{vmin}} + r_0^2 B_{min}^2 \left(\frac{\partial S}{\partial \psi} \right)^2 \frac{B^2(s)}{B_{min}^2} \frac{B_{vmin}}{B_v(s)}$$

$$\approx k_{10}^2 \frac{B^2(s)}{B_{min}^2} \frac{B_{vmin}}{B_v(s)},$$

when $r_0^4 / \ell^2 (\partial S / \partial \psi)^2 B_{min}^2 \gg 1$.

Normalizing the frequency, we can write the matrix elements of Eq. (3.25) as

$$Q_{ij}(y) = Q_{ij}^{(a)}(y) + Q_{ij}^{(b)}(y), \quad (3.31a)$$

$$Q_{ij}^{(a)} = \int_0^{L/2} \frac{ds}{B} [1 + \beta_c y^2 \left(\frac{\omega_k h_0}{k_{10}^2 v_A^2(0)} \right) \left(\frac{B_{min}}{B(s)} \right)^4] \frac{B_v(s)}{B_{vmin}}$$

$$+ \frac{1}{B} \frac{\partial P_{lh}}{\partial B} f_i(s) f_j(s), \quad (3.31b)$$

$$Q_{ij}^{(b)} = \alpha \int_1^{B_c/B_{min}} d\lambda \lambda^2 \langle f_i \rangle \langle f_j \rangle$$

$$\times ((\lambda-1) \left[\frac{2(\psi-\psi_0)}{\Delta\psi} + \frac{y \left(1 - \frac{(\psi-\psi_0)^2}{\Delta\psi^2} \right) \Delta_r}{R_0} \right] I^{(2)}(y, \lambda))$$

$$+ \frac{y \left(1 - \frac{(\psi - \psi_0)^2}{\Delta\psi^2} \right) \Delta_r}{R_0} I^{(1)}(y, \lambda) \}, \quad (3.31c)$$

with

$$I^{(1)}(y, \lambda) = \int_0^\infty \frac{dz z^{5/2} e^{-z}}{\Omega(y, \lambda, z)} = - \frac{\sqrt{\pi}}{c_1} \left[\frac{3}{4} + \frac{a}{2} + a^2 + a^{5/2} \cdot Z(a^{1/2}) \right],$$

$$I^{(2)}(y, \lambda) = \int_0^\infty \frac{dz z^{7/2} e^{-z}}{\Omega(y, \lambda, z)} = - \frac{15\sqrt{\pi}}{8c_1} + a I^{(1)}(y, \lambda),$$

where we define

$$a = c_2/c_1, \quad c_2 = \frac{\tau(\lambda)y\Delta_r}{R_0}, \quad \Omega(y, \lambda, z) = c_2 - zc_1,$$

$$c_1 = \frac{\Delta\psi}{B_c} \left[\lambda \left\langle \frac{1}{r} \frac{d^2 r}{ds^2} \left(1 + \frac{P_{\perp h}^{-P} \parallel h}{B^2} \right) \right\rangle + 2 \left\langle \frac{1}{r} \frac{d^2 r}{ds^2} \left(\frac{B_c}{B} - \lambda \right) \right\rangle \right. \\ \left. - \lambda \left\langle \frac{1}{B} \frac{dP_{\perp h}}{d\psi} + \frac{1}{B} \frac{dP_c}{d\psi} \right\rangle \right],$$

$$\langle \dots \rangle = \frac{1}{\sqrt{2}} \int_0^{s_T} \frac{ds(\dots)}{\sqrt{1 - \lambda B/B_c}},$$

$$B(s_T) = \lambda B_c, \quad \tau(\lambda) = \langle 1 \rangle,$$

$$\alpha = 2\left(\frac{2}{\pi}\right)^{1/2} \frac{\hat{P}_{\perp h}}{B_c^3 \left(1 - \frac{B_{\min}}{B_c}\right)^{3/2} \left(1 + \frac{4B_c}{B_{\min}}\right)}$$

$$\lambda = \mu B_c / E, \quad z = E/T, \quad y = \omega / \omega_{\kappa h 0}$$

$$\omega_{\kappa h 0} = \frac{\ell T}{r_0 R_0 \omega_{\text{cmin}}}, \quad \omega_{\text{cmin}} = \frac{q_h B_{\text{vmin}}}{m_h}$$

$$\Delta_r = \frac{\Delta\psi}{B_{\text{vmin}} r_0}$$

and R_0 is the radius of curvature at $s=0$, $R_0 = -[\kappa(s=0)]^{-1}$.

Once y is determined, the eigenfunctions can be found by fixing one of the coefficients and inverting the non-vanishing matrix to obtain the a_n 's. Some care must be exercised in calculating the integrals $I^{(1)}(y, \lambda)$ and $I^{(2)}(y, \lambda)$. $I^{(1)}$ can be rewritten as

$$\begin{aligned} I^{(1)}(y, \lambda) &= \int_0^{\infty} \frac{dz z^{5/2} e^{-z}}{c_2 - zc_1} \\ &= -\frac{\sqrt{\pi}}{c_1} \left(\frac{3}{4} + \frac{a}{2} + a^2 \right) \\ &\quad + \frac{a^{5/2}}{2c_1} \left(\int_{-\infty}^{\infty} \frac{du e^{-u^2}}{\sqrt{a} + u} + \int_{-\infty}^{\infty} \frac{du e^{-u^2}}{\sqrt{a} - u} \right); \end{aligned} \quad (3.32)$$

note that $u^2 = z$. The plasma dispersion function is defined by

$$Z(\zeta) \equiv \frac{1}{\sqrt{\pi}} \int_{-\infty}^{\infty} \frac{d\beta e^{-\beta^2}}{\beta - \zeta} \quad (3.33)$$

for $\text{Im } \zeta > 0$, and by its analytic continuation for $\text{Im } \zeta < 0$.⁷⁰

Thus, we write

$$I^{(1)}(y, \lambda) = -\frac{\sqrt{\pi}}{c_1} \left(\frac{3}{4} + \frac{a}{2} + a^2 \right) + \frac{a^{5/2}}{c_1} Z(\sqrt{a}) \quad (3.34)$$

If $\text{Im } \omega > 0$, clearly we should choose the sign of $a^{1/2}$ such that $\text{Im } a^{1/2} > 0$. On the other hand if $\text{Im } \omega < 0$, we require $\text{Im } a^{1/2} < 0$ so that the Z-function picks up a pole in the lower half plane, as we would expect from causality. If $\text{Im } \omega = 0$, the sign of $a^{1/2}$ is chosen so that $\text{Im } a^{1/2}$ is positive when $\omega + i\varepsilon$, $\varepsilon > 0$, $\varepsilon \ll 1$ is inserted into a instead. In those cases where $(\text{Re } c_2)c_1 < 0$, the result obtained is not the same as when $\varepsilon < 0$. However, in this instance there is no resonance ($\omega \neq \omega_d$), and we observe either an unstable ($\text{Im } \omega > 0$), or purely oscillatory ($\text{Im } \omega = 0$) mode. Thus there is no need for a continuous transition to damped roots.

3.3.b Results

Relevant values of the dimensionless quantities needed here are calculated using EBT-S parameters.⁵⁷ We take $B_{vmin} = 5$ kG (at the annulus location) and $B_{vmax} = 10$ kG to get a mirror ratio of 2. This corresponds to using $\epsilon = 1/4$ in Eq. (3.27). The length of a mirror cell is $L \sim 40$ cm, and the radius of the hot electron ring is $r_0 \sim 10$ cm; thus, $r_0/L = 1/4$. We can then calculate $R_0 = 16$ cm from Eq. (3.30). Assuming $\hat{P}_{lh}/B_{vmin}^2 = 0.2$ yields a maximum $\beta_h \sim 40\%$. The hot electron ring is presumed to extend halfway from midplane to the mirror throat, i.e., $s_c/L = 1/4$. In determining a value for $\omega_{kh0}^2/k_{10}^2 V_A^2(0)$, the azimuthal and radial mode numbers must be fixed. Following Ref. 36, we assume $k_{10}^2 r_0^2 = 400$ (corresponding to $k_{10} = 2/\Delta_r$ at $\Delta_r = 1$ cm). The hot electron temperature, T , is set equal to 500 keV. We will consider the following two cases:

$$(i) \quad \frac{\omega_{kh0}^2}{k_{10}^2 V_A^2(0)} = 0.2, \quad \text{and} \quad (ii) \quad \frac{\omega_{kh0}^2}{k_{10}^2 V_A^2(0)} = 0.014.$$

If we use $\ell = 3$ for the azimuthal mode number, these values correspond to core densities of $n_i = 2 \times 10^{13} \text{ cm}^{-3}$ and $1.3 \times 10^{12} \text{ cm}^{-3}$, respectively. The latter figure is typical of EBT-S experiments, while the former represents a reasonable regime for a more advanced

device. Note that even if we fix $n_i = 1.3 \times 10^{12} \text{ cm}^{-3}$, we can still obtain

$$\frac{\omega_{kh0}^2}{k_{10}^2 V_A^2(0)} \cong 0.2 \quad \text{if} \quad \ell = 11.$$

Regardless of the interpretation of the parameters in case (i), we will see that the mode is predicted to be far from marginal stability at drift reversal, and will give rise to some very interesting behavior when the particle drifts are not reversed. Finally, we take $\psi = \psi_0 + \Delta\psi/2$ in order to examine the behavior of the system in the middle of the pressure gradient region.

Since Eq. (3.22) provides a good approximation to the eigenvalue for $\omega/\langle\omega_d\rangle \ll 1$, it is used to obtain a starting point for other calculations. The value of $\langle\omega_d\rangle$ can be varied by altering the annulus thickness via the parameter $\Delta_{rm} = \Delta_r/r_0$; in particular, $\omega/\langle\omega_d\rangle \ll 1$ when $\Delta_{rm} \ll 1$. Following experimental estimates, previous theoretical investigations used $\Delta_r = 1 - 2 \text{ cm}$ (i.e., $\Delta_{rm} = 0.1 - 0.2$); more recent measurements show that Δ_r may be as large as 5 cm.^{31,32,71}

Figures 3.1 ($\omega_{kh0}^2/k_{10}^2 V_A^2(0) = 0.2$) and 3.2 ($\omega_{kh0}^2/k_{10}^2 V_A^2(0) = 0.014$) show the imaginary part of the eigenvalue as the parameter Δ_{rm} is scanned. Both of these figures contain curves generated by

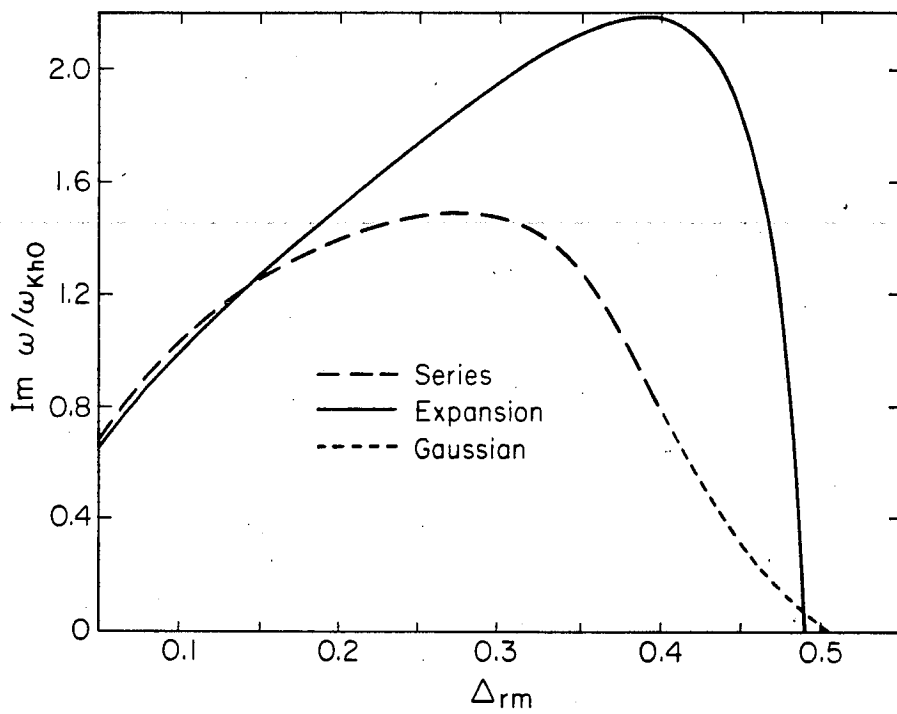


Fig. 3.1. Imaginary part of the eigenvalue plotted as a function of the parameter Δr_m with $\omega_{kh0}^2/k_{10}^2 v_A^2(0) = 0.2$. Curves representing a calculation with a ten term series expansion for $B_{||}$, the asymptotic expansion, Eq. (3.22), and a Gaussian test function (Eq. (3.24), with $s_0=0.04$), appear.

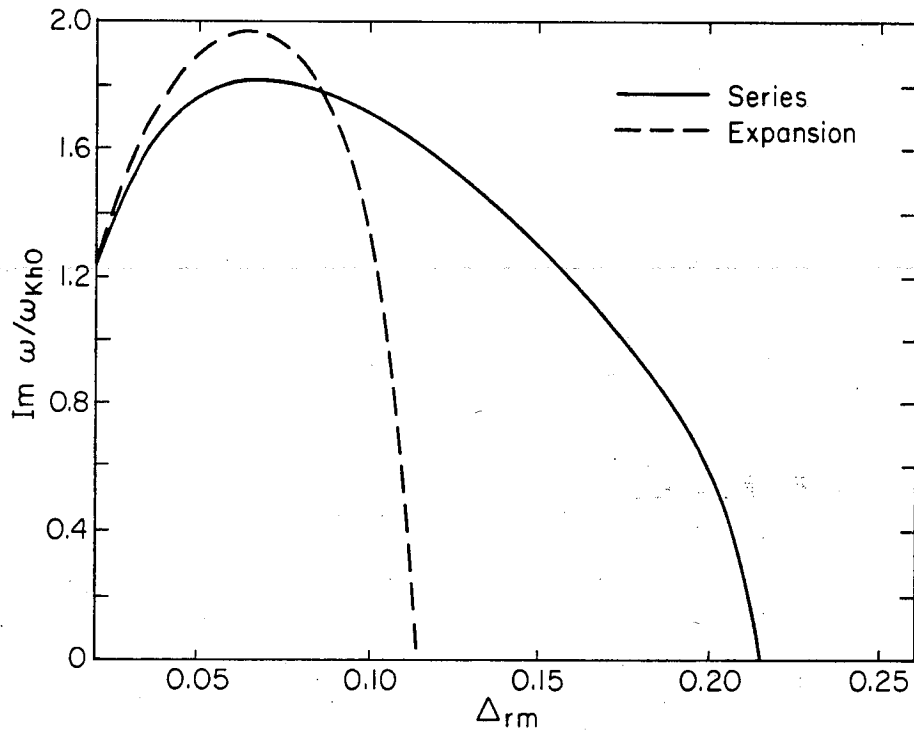


Fig. 3.2. Imaginary part of the eigenvalue plotted as a function of the parameter Δ_{rm} with $\omega_{kh0}^2/k_{10}^2 v_A^2(0) = 0.014$. Curves representing a calculation with a seven term series expansion for $B_{||}$ and with the asymptotic expansion, Eq. (3.22), appear.

using the asymptotic expansion, Eq. (3.22), and in each case, the results match quite well with the complete solution for $\Delta_{rm} \lesssim 0.1$, but differ significantly for larger ring widths. The errors increase as the scan proceeds due to a gradual decrease in the validity of the expansion of the resonant denominator. Also, it is apparent that Eq. (3.22) yields stable solutions for greater pressure gradients than the integral equation.

Since $\omega_{kh0}^2/k_{l0}^2 v_A^2(0)$ is proportional to n_i , the solutions of the integral equation indicate that a smaller core density will allow a larger pressure gradient before the magnetic compressional mode is destabilized. In particular, Fig. 3.2 suggests that $\Delta_r/r_0 \gtrsim 0.2$ is needed for the system to be stable. The very high density case, represented by Fig. 3.1, requires a considerably wider ring to be stable, $\Delta_r \gtrsim r_0/2$. There are other interesting effects occurring in this case; all of the calculations to follow assume $\omega_{kh0}^2/k_{l0}^2 v_A^2(0) = 0.2$.

Now, we fix the value of Δ_{rm} and scan over the core pressure, \hat{P}_c ($\beta_c \sim 2 \hat{P}_c/B_{vmin}^2$). Figure 3.3 shows the imaginary part of the eigenvalue for $\Delta_{rm} = 0.3$. In the plot, three curves appear, representing the results of using: $B_{||} = [C(\psi)/B] dP_{lh}/d\psi$, ten term cosine series, and the asymptotic expansion. All three of these methods indicate stability for $\beta_c \gtrsim 17\%$. From the results of Refs. 34, 36, and 64, it is known that the magnetic compressional mode is stable for all values of n_h/n_i if $\beta_c R_0/2\Delta_r > 1 + P_{||h}/P_{lh}$.

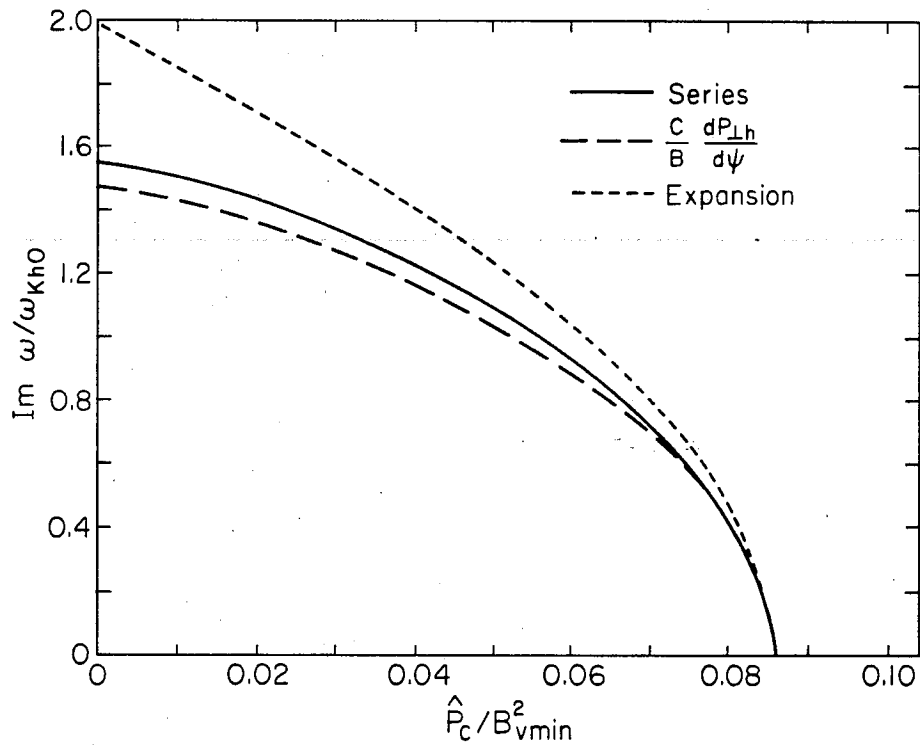


Fig. 3.3. Imaginary part of the eigenvalue plotted as a function of the parameter \hat{P}_c/B_{vmin}^2 with $\Delta_{rm}=0.3$. Three curves appear: one term representation, $B_{\parallel} = (C(\psi)/B)dP_{\perp h}/d\psi$; ten term cosine series; and the asymptotic expansion, Eq. (3.22).

But, since we consider here one particular nonzero value of n_h/n_i , the restriction on β_c is less severe, about half of what is required by $\beta_c R_0/2\Delta_r > 1$.

An analytic approach that is valid for arbitrary values of Δ_{rm} can be obtained in the manner described by Berk et al.³⁶ The authors employ a delta function distribution for the hot electrons in a local (no bounce averages) WKB approximation. If we take

$$F_h(p_{\parallel}, \mu) \propto \delta(p_{\parallel} - p_{\parallel 0}) \delta(\mu - \mu_0),$$

with $\beta_h \sim P_{\parallel h}/P_{\perp h} < 1$, we obtain a cubic dispersion relation for the magnetic compressional mode (we evaluate all quantities at midplane, $s=0$)

$$y^3 + a_2 y^2 + a_1 y + a_0 = 0, \quad (3.35)$$

where

$$a_2 = - \frac{B_{vmin}}{c_0 B_{min}} \left(r_0 R_0 \frac{dB}{d\psi} - P_{\parallel h}/P_{\perp h} \right),$$

$$a_1 = - (1 + \beta_c + \beta_{\perp h}) \frac{k_{\perp}^2 v_A^2(0)}{\omega_{kh0}^2},$$

$$a_0 = - \frac{B_{vmin}}{c_0 B_{min}} \frac{k_{\perp 0}^2 V_A^2(0)}{\omega_{kh0}^2} \left[1 + P_{\parallel h}/P_{\perp h} + R_0 r_0 B_{min} \frac{d}{d\psi} \left(\frac{P_c}{B^2} \right) \right],$$

and c_0 is a numerical factor relating μ_0 to the parameter T used in Eq. (3.26).

It is a straightforward procedure to calculate the marginally stable value of \hat{P}_c for a given value of Δ_{rm} . A calculation with the parameters used in Fig. 3.3 gives a value within 10% of that seen in the plot. Discrepancies of this size can then be attributed to the lack of field line averages and to differences in the distribution function. Note also that when $\beta_c R_0/2\Delta_r$ becomes larger than $1 + P_{\parallel h}/P_{\perp h}$, a_0 changes sign and forces the roots obtained by balancing the last three terms in Eq. (3.35) to be real for any value of $\omega_{kh0}^2/k_{\perp 0}^2 V_A^2(0)$. This is the origin of the criterion discussed in Refs. 34, 36 and 64. Returning now to Fig. 3.3, we note that the results obtained from using $B_{\parallel} = [C(\psi)/B]dP_{\perp h}/d\psi$ differ by less than 10% from those calculated with the ten term cosine series. The asymptotic expansion is considerably less accurate, as would be expected for such a large value of Δ_{rm} . However, these differences get smaller as \hat{P} increases, becoming negligible as marginal stability is approached. Similar behavior occurs at other values of Δ_{rm} .

Figures 3.4 and 3.5 show the field line dependence of B_{\parallel} in two cases. This is determined by the method described in Sec. 3.3.a. For comparison, we include a plot of $(1/B)dP_{\perp h}/d\psi$ as a function of s . We then see that the reason for the above trend is that $B_{\parallel}(s)$ converges toward $(1/B)dP_{\perp h}/d\psi(s)$ as the core pressure gets larger. Note that the single term result yields a good eigenvalue for $\hat{P}_c/B_{vmin}^2 = 0.002$ even though the eigenfunction differs considerably from the correct result.

We note that the degree of validity of $B_{\parallel} = [C(\psi)/B]dP_{\perp h}/d\psi$ is dependent on the extent to which³⁴

$$\left| \frac{1}{B} \frac{dP_{\perp h}}{d\psi} \right| > \left| \frac{\kappa\sigma}{r} - \frac{1}{B} \frac{dP_c}{d\psi} \right|. \quad (3.36)$$

Then it is clear that this approximate form of B_{\parallel} , as well as the expansion of the resonant denominator in Eq. (3.22), will become more accurate as the core pressure is increased. This explains the decreases in the errors seen in Figs. 3.3-3.5.

When the above inequality is well satisfied, the hot particle drifts are reversed from their vacuum values. For $\hat{P}_c=0$, this is the case for $\Delta_{rm} \leq 0.25$. However, $\Delta_{rm} = 0.3$ yields drifts in the same direction as in vacuum. But, it is clear from Eq. (3.36) that larger core pressures may also bring about drift

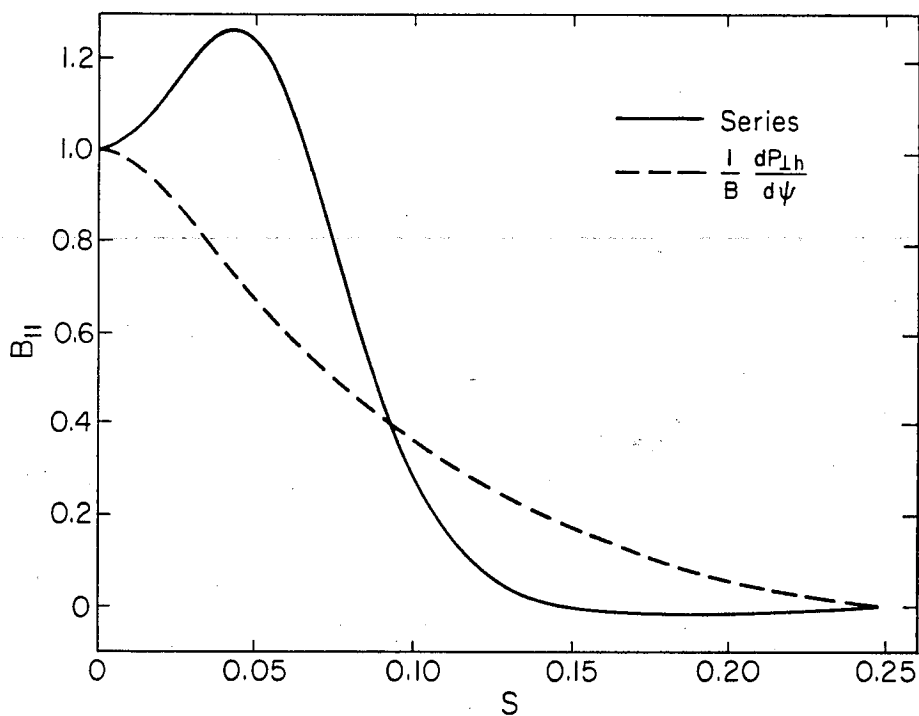


Fig. 3.4. Eigenfunction plotted as a function of the distance along the field line, s , for $\Delta_{rm}=0.3$ and $\hat{P}_c/B_{vmin}^2 = 0.002$. Two curves appear; one is the result of the ten term cosine series calculation; the other is a plot of $(1/B)dP_{||h}/d\psi$ provided for comparison.

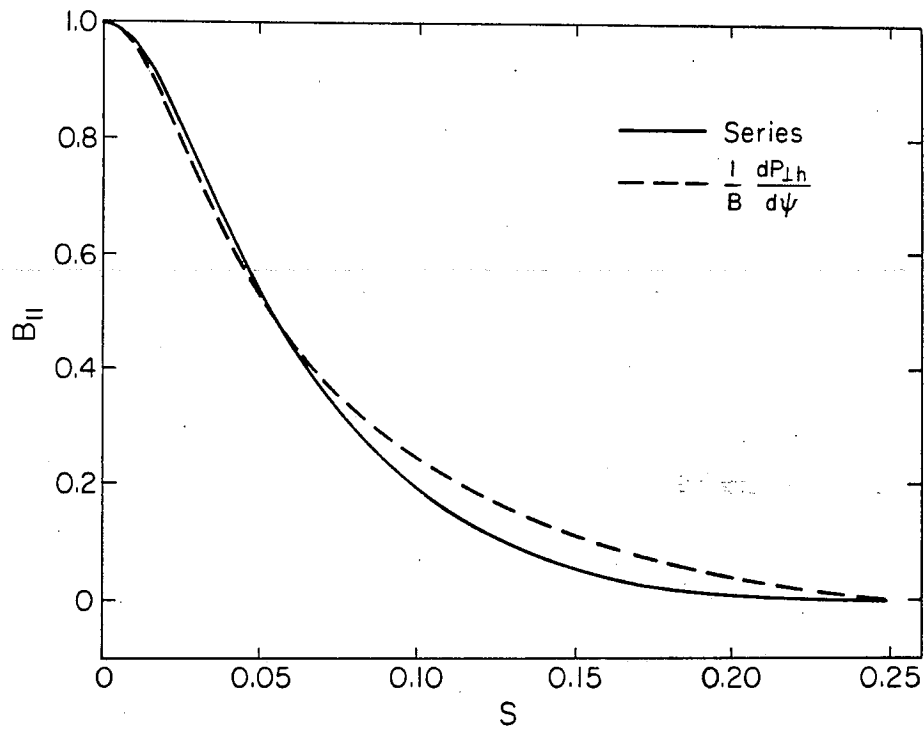


Fig. 3.5. Eigenfunction plotted as a function of the distance along the field line, s , for $\Delta_{rm}=0.3$ and $\hat{P}_c/B_{vmin}^2 = 0.084$. Two curves appear; one is the result of the ten term cosine series calculation; the other is a plot of $(1/B)dP_{||h}/d\psi$ provided for comparison.

reversal. This occurs in Fig 3.3 before the marginally stable point is reached; that is, Eq. (3.36) is then well satisfied.

Using the calculated coefficients a_n and eigenvalue ω , both sides of Eq. (3.21) can be computed as a function of the number of terms in the series N . In Fig. 3.6 we plot the negative logarithm of δ , defined as the absolute value of the difference between the right and left-hand sides of Eq. (3.21), for $N = 2 - 10$, and $\Delta_{rm} = 0.1, 0.2, 0.3$ and 0.4 . This is a measure of how well the expansion worked at each N . Clearly, $N=10$ represents an effectively converged series for $\Delta_{rm} = 0.1$ and 0.2 , but not for $\Delta_{rm} = 0.3$ and 0.4 . For $\Delta_{rm} > 0.4$, ten terms soon become insufficient to represent the eigenfunction, and we are not able to determine the marginally stable point at large core densities using this method. The single term representation, $B_{||} = [C(\psi)/B]dP_{||h}/d\psi$, also becomes ineffective at this point. For example, Fig. 3.7 shows the eigenfunction calculated using the ten terms with $\Delta_{rm} = 0.4435$ and $\hat{P}_c/B_{vmin}^2 = 0.002$. The peak near $s_0=0.07$ requires a more rapid variation along the field line than f_{10} is capable of providing. As a result, there is quite a bit of overshoot at large s where $B_{||}$ should be smoothly approaching zero.

At this point, the Gaussian test function of Eq. (3.24) proves very useful. The curve in Fig. 3.1 is extended past $\Delta_{rm} = 0.4$ by this approach. Matching results at $\Delta_{rm} = 0.4$ as closely as possible suggests setting $s_0 = 0.04$. We then calculate that the

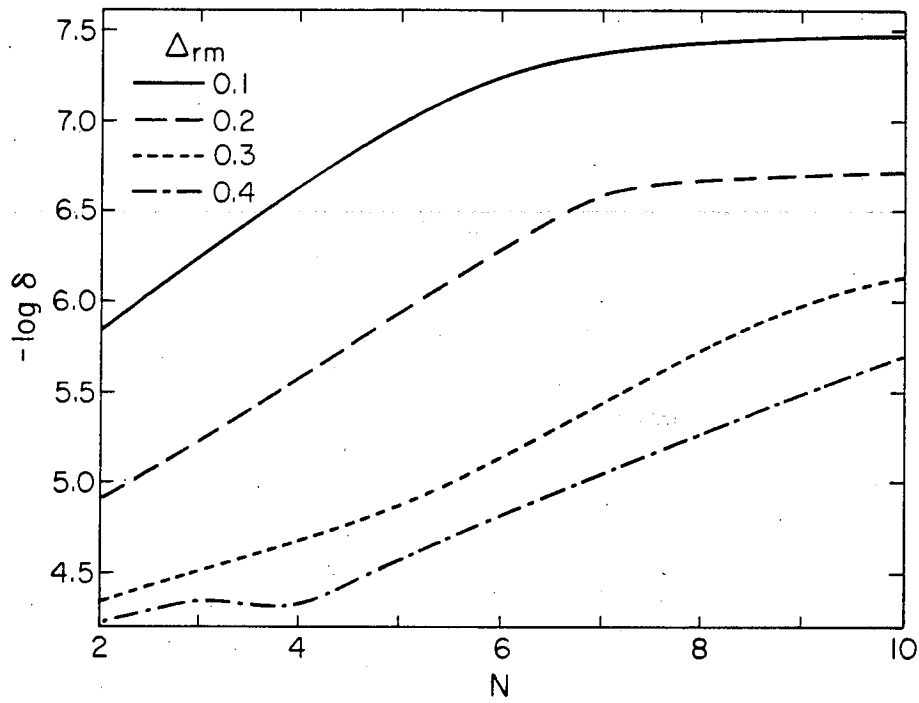


Fig. 3.6. Negative logarithm of δ , the difference between the right and left-hand sides of Eq. (3.21), evaluated with the values of ω and B_{\parallel} obtained by using an N term cosine series expansion for B_{\parallel} . Separate curves appear for $\Delta_{rm} = 0.1, 0.2, 0.3,$ and 0.4 .

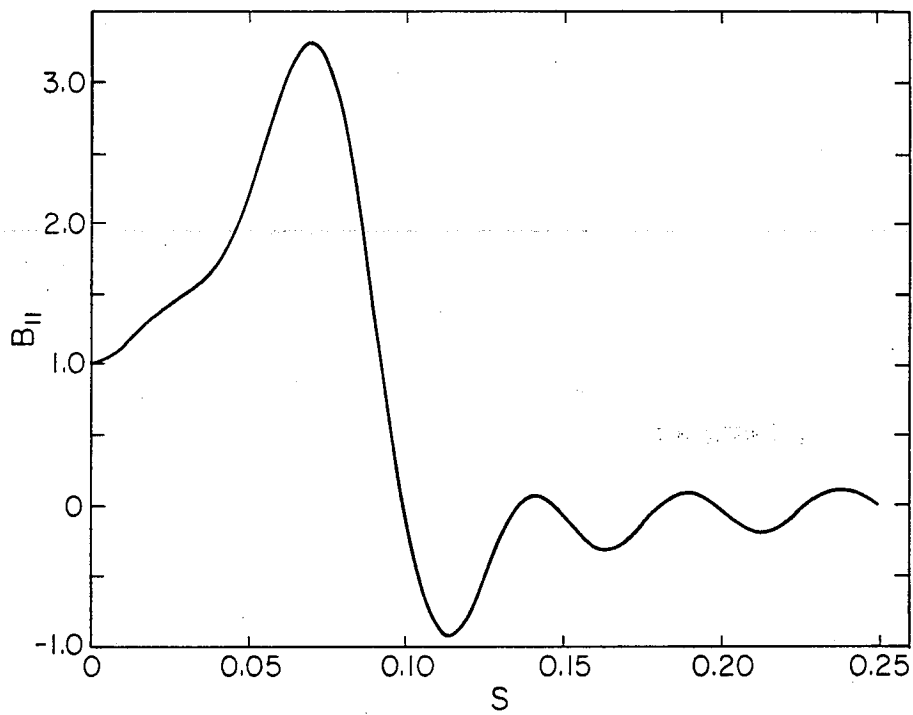


Fig. 3.7. Eigenfunction plotted as a function of the distance along the field line, s , for $\Delta_{rm} = 0.4435$ and $\hat{P}_c/B_{vmin}^2 = 0.002$. The ten term cosine series is used in the calculation.

mode stabilizes when $\Delta_{rm} \gtrsim 0.5$, and is damped from there on. Apparently, the change in sign of $\text{Im } \omega$ results from a change in the relative sizes of the $\omega(\partial F/\partial E)$ and $\partial F/\partial \psi$ terms in the kinetic integral. This behavior can be explained as follows. First, we note that $\text{Re } y = \text{Re}(\omega/\omega_{kh0}) < 0$ in all cases. When the average drift frequency $\langle \omega_d \rangle$ (a function of pitch angle λ) is normalized in the same manner, it is positive for drift reversed particles (small Δ_{rm}). In this case, if $\text{Im } \omega = 0$, $I^{(1)}$ and $I^{(2)}$ of Eq. (3.31c) are real, and it is possible to have purely oscillatory solutions, as in Fig. 3.2 for $\Delta_{rm} \gtrsim 0.2$. Here, the decreases in $\partial F/\partial \psi$ and $\langle \omega_d \rangle$ arising from the increase in Δ_{rm} gradually reduce the effect of the hot electrons and, hence, lower the growth rate.

However, $\langle \omega_d \rangle < 0$ for large Δ_{rm} , and there is a possibility of having particles resonate with the wave, $\text{Re } \omega = \langle \omega_d \rangle$. Due to the fact that all particle energies are allowed by the chosen hot electron distribution function, there is always a fraction of particles for which this is approximately true, and for this reason, there is always some imaginary contribution made by $I^{(1)}$ and $I^{(2)}$. To obtain marginal stability now, the $\partial F/\partial \psi$ term must be small enough to exactly cancel $\omega(\partial F/\partial E)$ in the kinetic integral, e.g., for $\Delta_{rm} \gtrsim 0.5$ in Fig. 3.1. Unlike the case in Fig. 3.2, the solutions at larger Δ_{rm} are not oscillatory, but damped.

The peak observed in Figs. 3.4 and 3.7 is a characteristic of the resonance. Apparently, the eigenfunction reaches a maximum value at a position along the field line near the turning point $s_T(\lambda)$ of the pitch angle λ which yields the average drift $\langle \omega_d \rangle_\lambda$ closest to being resonant with the wave frequency ω . As $\text{Im } \omega$ decreases, the peak becomes more pronounced. Thus, we expect the convergence of the cosine series to get worse as the mode stabilizes. The Gaussian test function was chosen to circumvent this problem and appears to do so effectively. As was mentioned before, increasing the core pressure towards marginal stability for $\Delta_{rm} = 0.3$ and 0.4 also gives rise to drift reversal. In that case, the resonance is removed, and convergence should improve.

3.3.c Summary

We have numerically solved the integral equation to determine the eigenvalues and eigenfunctions of the magnetic compressional mode; the results match those of the asymptotic expansion in the case of a deep diamagnetic well. The use of a trial function, $B_{\parallel} = [C(\psi)/B]dP_{\perp h}/d\psi$ is found to give accurate eigenvalues over a large range of parameter values (Fig. 3.3), although $B_{\parallel} = [C(\psi)/B]dP_{\perp h}/d\psi$ can at times differ considerably from the actual B_{\parallel} (Fig. 3.4).

In those cases where there is no drift reversal, and large core densities are present, a wave-particle resonance is predicted, causing the mode to be unstable unless the ring half-width is some significant fraction of the annulus radius. Numerically, it has the effect of reducing the rate of convergence of the expansion, Eq. (3.23) (Fig. 3.6); eventually, it makes solutions via that method impractical. Use of the Gaussian test function, Eq. (3.24), proves very helpful in following the mode to marginal stability in this case.

The real part of the frequency near marginal stability is on the order of the curvature drift frequency of the hot electrons: $\omega \sim 2\omega_{kh0}$ in Fig. 3.1, and $\omega \sim 4\omega_{kh0}$ in Fig. 3.2. With the parameters used in Sec. 3.3.b, we can calculate corresponding oscillation frequencies, $\omega/2\pi \sim 60$ and 120 MHz, respectively. Hiroe et al.⁷² recently reported experimental observations of instabilities with frequencies around 100 MHz as the ambient pressure was reduced from the T-mode regime; further reductions of the ambient pressure were accompanied by a drop in this frequency, peaking near 20 MHz at the T-M transition. Recent experimental determinations of radial width indicate that the radial scale length of the ring is near 5 cm in EBT-S.^{31,32,71} While the results shown in Fig. 3.1 predict the magnetic compressional mode to be near threshold when $\Delta_r = 5$ cm with a core density $n_i = 1.3 \times 10^{12}$ cm⁻³ and a mode number of $\ell=11$, the value of β_h used here (~40%)

yields at this ring width a total stored perpendicular energy some 4 - 8 times larger than the value of 30 J found experimentally. The experimental β_h should be lower by a corresponding factor (say, $\beta_h \sim 5 - 10\%$). Reducing $\hat{P}_{\perp h}/B_{vmin}^2$ accordingly will place the magnetic compressional mode well below the threshold for instability. Thus, it does not appear to be a likely candidate for the 100 MHz oscillations observed in EBT-S. On the other hand, it is still possible that the nonlinear properties of the magnetic compressional mode are causing a radial spreading of what would otherwise be a sharp gradient; transport phenomena are also a primary consideration in this matter.

Finally, an analytic approach employing a delta function distribution for the hot electron,^{34,36} is used to provide values of the core pressure and density at marginal stability. The results of the calculations are in good agreement with the numerical computations in the drift reversed situations. The condition for stability of the magnetic compressional mode with an arbitrary value of n_h/n_i then appears to be that $\beta_c R/2\Delta_r > 1 + P_{\parallel h}/P_{\perp h}$, even when $\beta_h R/2\Delta_r$ is not large. Of course, if this were the case, more familiar MHD modes could be unstable. In particular, note that this criterion requires a value of β_c above the Lee-Van Dam limit for stability of the interacting pressure-driven interchange. More generally, a given value of

n_h/n_i can be stable if the pressure scale length Δ_r is large enough.

3.4 Coupled Equations

We now consider the numerical solution of the coupled equations in φ and B_{\parallel} obtained from Eq. (3.2) by variations with respect to those variables (see also Ref. 73). The equilibrium discussed above in Sec. 3.3.a will be used here as well. In the deep diamagnetic well limit, it is reasonable to set $B_{\parallel} = [C(\psi)/B] dP_{\perp h}/d\psi$ and expand the resonant denominator to obtain a simpler equation, namely Eq. (3.8) derived in Sec. 3.2. However, when $|dP_{\perp h}/Bd\psi| \approx |\kappa/r|$, we must solve the complete integro-differential equations. To facilitate the solution, we expand B_{\parallel} and φ in complete sets of functions. We also make use of the fact that where $P_{\perp h} = 0$, B_{\parallel} is proportional to φ [see Eq. (3.4)]. So, now B_{\parallel} does not vanish outside the hot electron region, but its behavior is known. Namely, we write

$$B_{\parallel} = \sum_{n=1}^M b_n f_n(s) + \alpha(s) \sum_{n=1}^M a_n g_n(s), \quad (3.37a)$$

$$\varphi = \sum_{n=1}^M a_n g_n(s) \left(\frac{-\omega}{\ell dB/d\psi_0} \right), \quad (3.37b)$$

where

$$f_n(s) = \begin{cases} \cos\left[\frac{\pi(n-1/2)s}{s_c}\right] & 0 \leq s \leq s_c \\ 0 & s_c \leq s \leq L/2, \end{cases}$$

$$g_n(s) = \cos\left[(n-1)\frac{2\pi s}{L}\right] \quad 0 \leq s \leq L/2,$$

$$\alpha(s) \equiv -\frac{B}{dB/d\psi_0} \frac{d}{d\psi} \left(\frac{P_c}{B^2}\right),$$

$$\frac{dB}{d\psi_0} \equiv \frac{dB}{d\psi}(s=0).$$

In theory M should be taken to infinity, but of course will be finite here and used in the bookkeeping needed to solve these equations. A complete solution of the equations specifies the eigenvalue ω , and the Fourier coefficients a_n and b_n . Even eigenmodes are assumed, although the symmetry of the system allows odd perturbations as well. The distribution function, pressure profiles, and vacuum magnetic field function are as in Sec. 3.3.a. However, now we use a more complete expression for $k_{\perp}(s)$ since the azimuthal mode number ℓ will appear explicitly in the equations,

$$k_{\perp}^2(s) = \frac{\ell^2 B_{\nu}(s)}{r_0^2 B_{\nu\min}} + k_{\perp 0}^2 \frac{B^2(s) B_{\nu\min}}{E_{\min}^2 B_{\nu}(s)} \quad (3.38)$$

This reduces to the previous expression in the limit $\ell \rightarrow 0$.

After inserting the above forms for φ and B_{\parallel} into Eq. (3.2), varying with respect to each of the coefficients, a_i^* and b_i^* , for $i=1, M$ and applying the equilibrium, we get the matrix equations,

$$\begin{bmatrix} Q^{11} & Q^{12} \\ Q^{21} & Q^{22} \end{bmatrix} \begin{bmatrix} \tilde{b} \\ \tilde{a} \end{bmatrix} = 0, \quad (3.39)$$

where the elements of each of the four submatrices are

$$Q_{ij}^{11} = \int_0^{L/2} ds (A_1 + y^2 A_2) f_i f_j + \int_1^{B_c/B_{\min}} d\lambda C \langle \lambda f_i \rangle \langle \lambda f_j \rangle ; \quad i=1, M; j=1, M,$$

$$Q_{ij}^{12} = \left[\int_0^{L/2} ds (A_3 + y^2 A_4) f_i g_{j-M} - \int_1^{B_c/B_{\min}} d\lambda C \langle \lambda f_i \rangle \langle g_{j-M} \left(\lambda B \frac{d}{d\psi} \left(\frac{P_c}{B^2} \right) + D_r \right) \right] / (dB/d\psi_0);$$

$$i=1, M; j=M+1, 2M,$$

$$= Q_{ji}^{21}; \quad i=M+1, 2M; j=1, M,$$

$$Q_{ij}^{22} = \left(\int_0^{L/2} ds [(A_5 + y^2 A_6) g_{i-M} g_{j-M} + A_7 e_{i-M} e_{j-M}] \right. \\ \left. + \int_1^{B_c/B_{\min}} d\lambda C \langle g_{i-M} (\lambda B \frac{d}{d\psi} (\frac{P_c}{B^2}) + D_r) \rangle \right. \\ \left. \times \langle g_{j-M} (\lambda B \frac{d}{d\psi} (\frac{P_c}{B^2}) + D_r) \rangle \right) / (dB/d\psi_0)^2;$$

$$i=M+1, 2M; j=M+1, 2M;$$

$$\tilde{a}_i = a_{i-M}; \quad i=M+1, 2M,$$

$$\tilde{b}_i = b_i; \quad j=1, M.$$

The various fluid quantities are

$$A_1 = \frac{1}{B} \left(1 + \beta_c + \frac{1}{B} \frac{\partial P_{lh}}{\partial B} \right),$$

$$A_2 = - \frac{\Delta}{B} \frac{B_{\min}^2}{B^2} \frac{k_{10}^2 r_0^2}{k_1^2(s) r_0^2},$$

$$A_3 = - \left[B \frac{d}{d\psi} \left(\frac{P_c}{B^2} \right) \right] A_1 + \frac{1}{B} \left[B \frac{d}{d\psi} \left(\frac{P_c}{B^2} \right) + \frac{1}{B} \frac{\partial P_{lh}}{\partial \psi} \right],$$

$$A_4 = - \left[B \frac{d}{d\psi} \left(\frac{P_c}{B^2} \right) \right] A_2,$$

$$A_5 = \left[B \frac{d}{d\psi} \left(\frac{P_c}{B^2} \right) \right]^2 A_1 - 2 \left[B \frac{d}{d\psi} \left(\frac{P_c}{B^2} \right) \right] \frac{1}{B} \left[B \frac{d}{d\psi} \left(\frac{P_c}{B^2} \right) + \frac{1}{B} \frac{\partial P_{\perp h}}{\partial \psi} \right] \\ - \frac{1}{B} \left(\frac{dB}{d\psi} \left[B \frac{d}{d\psi} \left(\frac{P_c}{B^2} \right) + \frac{1}{B} \frac{\partial P_{\perp h}}{\partial \psi} \right] + \frac{\kappa}{r} \left[\frac{d}{d\psi} \left(\frac{P_c}{B} \right) + \frac{1}{B} \frac{\partial P_{\parallel h}}{\partial \psi} \right] \right),$$

$$A_6 = \left[B \frac{d}{d\psi} \left(\frac{P_c}{B^2} \right) \right]^2 A_2 - \frac{\Lambda}{B} \frac{B_{\min}^2}{B^2} \frac{k_{\perp 0}^2 r_0^2 k_{\perp}^2(s) r_0^2}{\ell^2 r_0^4},$$

$$A_7 = \frac{\sigma}{B} \frac{k_{\perp}^2(s) r_0^2}{\ell^2 r_0^2 L^2},$$

Also, note that

$$\Lambda \equiv \frac{\omega_{\kappa h 0}^2}{k_{\perp 0}^2 V_A^2(0)},$$

$$e_i \equiv L \frac{dg_i}{ds},$$

$$C = C_{\text{mul}} \left((\lambda-1) \left\{ \frac{2(\psi-\psi_0)}{\Delta\psi} + y \left[1 - \frac{(\psi-\psi_0)^2}{\Delta\psi^2} \right] \frac{\Delta r}{R_0} \right\} I^{(2)}(y, \lambda) \right)$$

$$+ y \left[1 - \frac{(\psi - \psi_0)^2}{\Delta\psi^2} \right] \frac{\Delta_r}{R_0} I^{(1)}(y, \lambda),$$

$$D_r = \lambda \frac{dB}{d\psi} + 2 \left(\frac{B_c}{B} - \lambda \right) \frac{\kappa}{r},$$

$$C_{mul} = \frac{4}{\sqrt{2\pi}} \frac{\hat{P}_{\perp h}}{B_c^3 \left(1 - \frac{B_{min}}{B_c} \right)^{3/2} \left(1 + \frac{4B_c}{B_{min}} \right)}$$

All other quantities are defined in Sec. 3.3.a. The eigenvalue y can be found by setting the determinant of the complete matrix Q in Eq. (3.39) to zero. Note that solving $\det|Q^{11}|=0$ recovers the purely magnetic mode.

We now want to examine three questions: (i) is it appropriate to set $\varphi=0$ in these equations when looking at the magnetic compressional mode?, (ii) how does the inclusion of full field-line dependence alter the diamagnetic-well stabilization criterion?, and (iii) how does it affect the Nelson, Lee - Van Dam limit?

We first consider a solution of Eq. (3.39) using the same parameters as in Fig. 3.3; this is curve (i) in Fig. 3.8. For comparative purposes, we also include curves representing the purely magnetic mode, curve (ii) in Fig. 3.8, and the solution of Eq. (3.8), curve (iii) (valid for a deep diamagnetic well). The

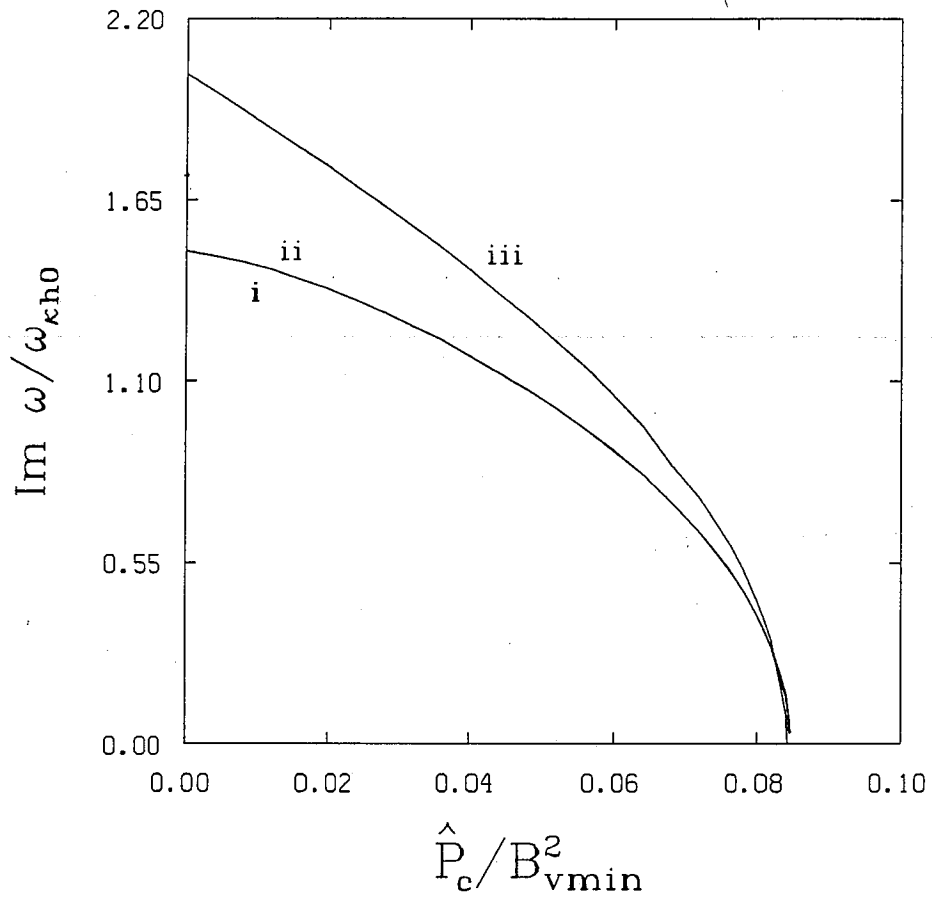


Fig. 3.8. Imaginary part of the eigenvalue for the magnetic compressional mode plotted as a function of the parameter \hat{P}_c/B_{vmin}^2 as in Fig. 3.3. Three curves appear: (i) solution of Eq. (3.39), (ii) solution of purely magnetic equation, and (iii) solution of asymptotic equation, Eq. (3.8).

azimuthal mode number was set at $\ell=6$. Despite the fact that \hat{P}_c (the coupling between B_{\parallel} and φ is proportional to \hat{P}_c) becomes significant with these parameters, the first two curves mentioned are virtually indistinguishable. For the same reasons described in connection with Fig. 3.3, the simpler result, Eq. (3.8), is relatively accurate, especially at large \hat{P}_c . From this we can conclude that the magnetic compressional mode is very well described by the purely magnetic equation. Again, the reason for the lack of significant coupling is the vast frequency difference between the magnetic compressional mode ($\omega \sim \omega_{kh0}$) and the interchange modes which arise from the φ equation ($\omega \ll \omega_{kh0}$).

Secondly, we consider diamagnetic-well stabilization of the background pressure-driven interchange mode by the hot electron pressure gradient. In Fig. 3.9, we assume $\hat{P}_c/B_{vmin}^2 = 0.002$, $\Lambda=0.063$, $\Delta_{rm}=0.1$, $k_{10}^2 r_0^2=400$, and $\ell=6$. To compare with the most basic criterion for stability, $\beta_h > 4\Delta_r/R - 2\beta_c$, we first calculate y as a function of \hat{P}_{1h} using Eq. (3.8), but evaluate all quantities at $s=0$ [curve (i) in Fig. 3.9]. The critical value obtained in this manner, $\hat{P}_{1h}/B_{vmin}^2=0.092$, yields a value of β_h relatively close to $4\Delta_r/R - 2\beta_c$. Curves (ii) and (iii) of Fig. 3.9 represent the solutions of Eq. (3.39), the full integro-differential equation, and of Eq. (3.8) including all field-line dependence, respectively. In this case, the simple result is quite accurate. The value of Δ_{rm} used here is small enough that the expansion of the resonant

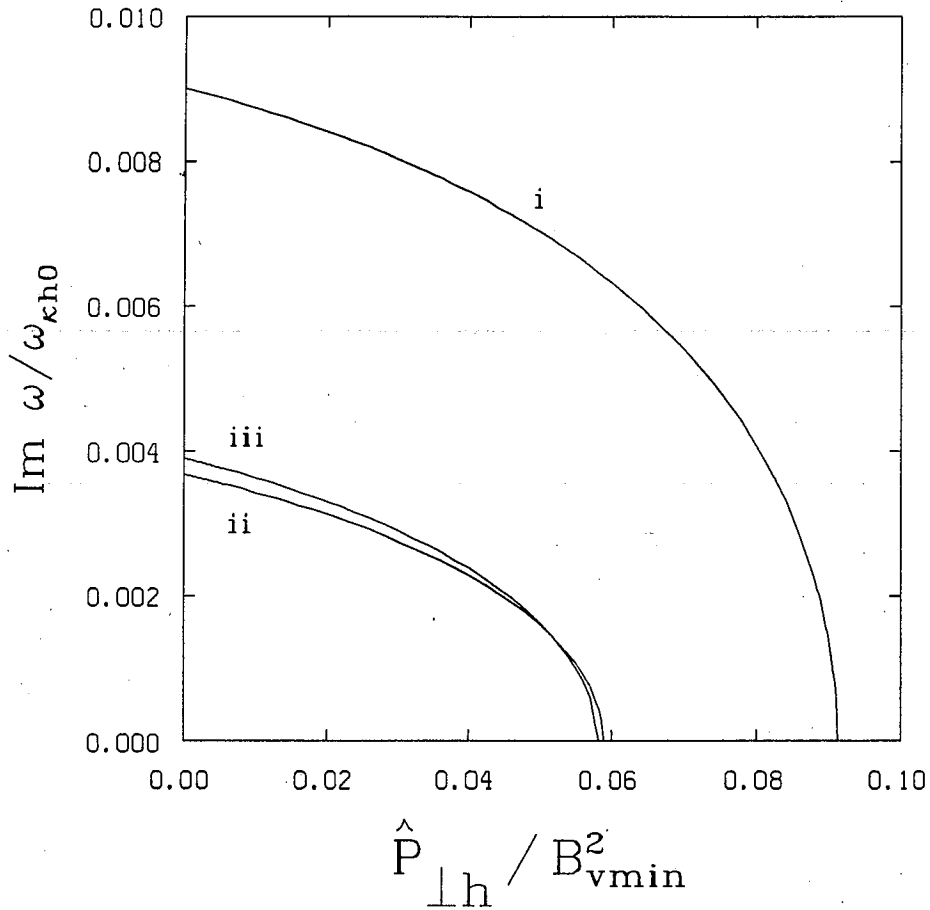


Fig. 3.9. Plot of the imaginary part of the eigenvalue for the background pressure-driven interchange as a function of $\hat{P}_{\perp h} / B_{vmin}^2$ for $\hat{P}_c / B_{vmin}^2 = 0.002$, $\Delta_{rm} = 0.1$. Three curves appear: (i) solution of asymptotic equation, Eq. (3.8), with all quantities evaluated at $s=0$, (ii) solution of Eq. (3.39), and (iii) solution of Eq. (3.8) with variations along the field line.

denominator employed in deriving Eq. (3.8) is quite valid, and we expect good agreement. We also note that the critical hot electron pressure ($\hat{P}_{\perp h}/B_{\text{vmin}}^2 \approx 0.06$) is significantly smaller than that obtained from the midplane evaluation, curve (i), as was the growth rate at $\hat{P}_{\perp h} = 0$. Since including field line variation brings in contributions from regions of more favorable curvature, this result is readily understood.

Finally, we look at the interacting pressure-driven interchange. Again, we first compare the simple local estimate of the limit on β_c , $\beta_c < 2\Delta_r/R$, with a midplane evaluation of Eq. (3.8). This result is represented by curve (i) in Fig. 3.10 where $\hat{P}_{\perp h}/B_{\text{vmin}}^2 = 0.12$, and all other quantities are as in Fig. 3.9. The critical value obtained in this manner, $\hat{P}_c/B_{\text{vmin}}^2 = 0.042$, yields a value of β_c close to $2\Delta_r/R$. The other two curves represent the eigenfrequencies obtained from solving the full equation, Eq. (3.39) [curve (ii) in Fig. 3.10], and Eq. (3.8) including field line dependence [curve (iii)]. Again, these two agree very well with one another because of the relatively small value of Δ_{rm} . Note that a smaller value of \hat{P}_c is required here to destabilize the mode than predicted by a midplane evaluation of Eq. (3.8) [curve (i)]; that is, the full equation is now more pessimistic than the local expression, although not by much. On the other hand, the growth rates obtained at larger values of \hat{P}_c are greater for the midplane evaluation curve. Since in this case the instability is

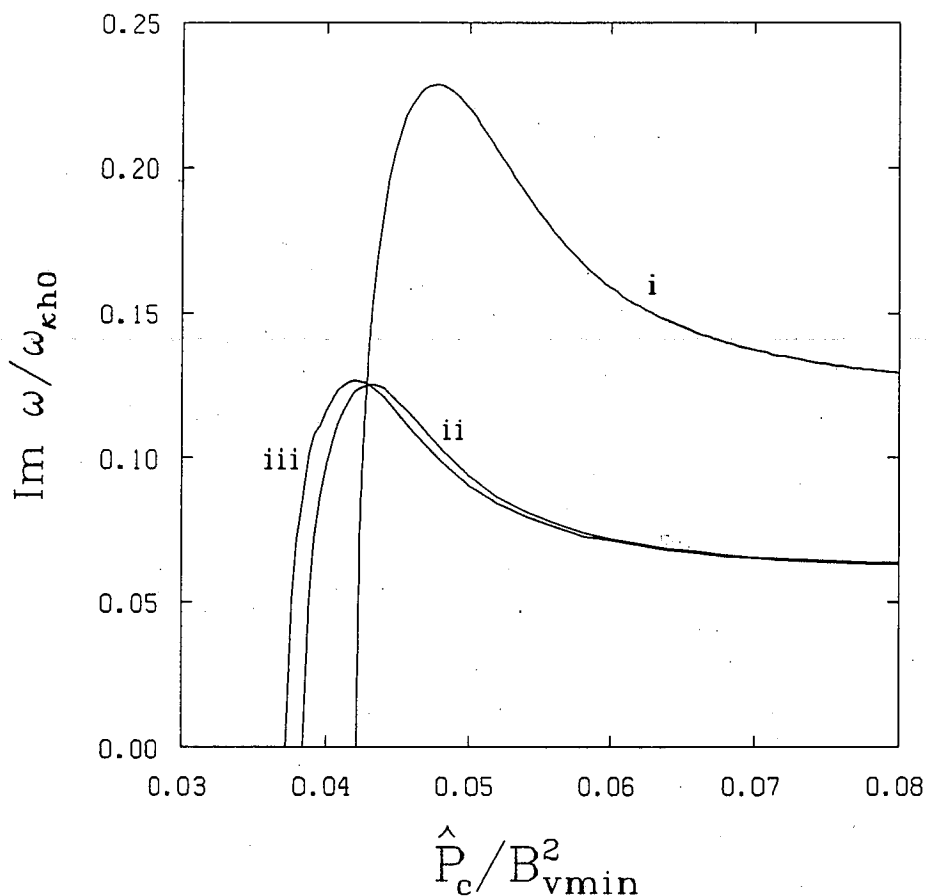


Fig. 3.10. Plot of the imaginary part of the eigenvalue for the interacting pressure-driven interchange mode as a function of \hat{P}_c/B_{vmin}^2 for $\hat{P}_{lh}/B_{vmin}^2=0.12$, and all other parameters are as in Fig. 3.9. Three curves appear: (i) solution of asymptotic equation, Eq. (3.8), with all quantities evaluated at $s=0$, (ii) solution of Eq. (3.39), and (iii) solution of Eq. (3.8) with variations along the field line.

driven by the product of total pressure gradient and curvature, we can again presume that the inclusion of favorable field-line curvature has lessened the severity of the instability.

CHAPTER IV

EFFECTS OF TRAPPED, ENERGETIC PARTICLES ON BALLOONING MODES IN TOKAMAKS

4.1 Introduction

It has long been known that effects beyond those embodied in MHD, such as FLR and pressure anisotropy, can have a significant effect on the stability of ballooning and interchange modes.^{33,74,75} Experimental reports of plasma pressures that may have been past the first stability boundary without indications of significantly decreased confinement^{76,77} motivated further investigations of kinetic effects in tokamak plasmas.^{78,79} These calculations predicted a stabilizing effect from FLR, but not one large enough to explain the experimental results. Tsang and Sigmar⁸⁰ suggested that the energetic particles introduced by neutral beam injection could provide the needed stabilization. Since then, other authors have looked at kinetic effects on ballooning modes, both due to the background plasma⁸¹ and the energetic species.^{69,82} More recently, it has been found that experimentally observed disruptive β limits^{83,84} match very closely

those predicted by newer MHD theories for ideal ballooning and kink modes.^{85,86}

The stabilizing influence of energetic beam ions was later suggested by Rosenbluth et al.³⁹ as a possible mechanism for reaching the second stability region of ballooning modes. Their results indicated that such an approach was viable, but the required temperatures of the ions would be quite high, of order 1 MeV. However, as was the case in the mirror geometry, the introduction of the energetic species brings with it the negative energy precessional mode.

That beam ions could have a destabilizing influence on tokamaks was first discovered in connection with perpendicular neutral beam injection experiments on PDX.⁸⁷ The resultant "fishbone" oscillations were observed to have a real frequency comparable to the precessional drift frequency ω_d , and were later explained theoretically as a precessional drift resonant destabilization of the internal kink mode.⁸⁸⁻⁹¹ An alternative interpretation has been described by Coppi and Porcelli.⁹² They contend that the fishbones are due to a core plasma mode with frequency $\omega \sim \omega_{*i}$ (ω_{*i} is the background plasma diamagnetic drift frequency) being destabilized by the dissipation arising from the mode - particle resonance, $\omega \sim \omega_d$, of the beam ions. Since it is observed in the PDX experiment that $\omega_{*i} \sim \omega_d$,^{87,92} the frequency

for the instability predicted by Coppi and Porcelli also closely matches that of the fishbone oscillations.

Subsequently, it was shown that a similar effect arises when the energetic particles interact with ballooning modes,^{69,93-95} and that the resultant instability was a good candidate for the high frequency precursor oscillations also observed in the PDX experiments.^{94,96} It should be noted that many of the conclusions regarding energetic species interacting with MHD modes can be applied qualitatively, if not quantitatively, to alpha particles arising in fusion reactions, as has been discussed by others.^{95,97-100} In particular, precessional drift-resonant alpha particles may have a deleterious effect on the stability of near-term breakeven experiments such as TFTR.^{95,100,101}

In this chapter, we consider again the numerical solution of the ballooning mode equations with kinetic effects, Eq. (3.1), appropriately modified for tokamak geometry. As in Chapter III, the integral terms and resonant denominator will be treated without approximation. A model distribution function describing particles trapped in the bad curvature region of the tokamak (deeply trapped) is assumed, and an appropriate large aspect ratio, low beta equilibrium is calculated analytically. The stability characteristics of the low frequency ($\text{Re } \omega \ll \omega_d$) MHD branch and the high frequency ($\text{Re } \omega \lesssim \omega_d$) precessional branch will be examined. Other instabilities may be present in the system; as one

example, we will consider energetic particle destabilization of the discrete eigenmodes set up by the toroidal coupling of neighboring poloidal harmonics in the shear Alfvén spectrum¹⁰² (gap modes). Conclusions regarding the prospects of using deeply trapped energetic particles to reach second stability are drawn in Sec. 4.3.d.

The last section of the chapter discusses the possibility of using energetic particle distributions that peak in the good curvature region of the tokamak (on the inside of the torus) to remove the resonant destabilization of the precessional mode. After describing the necessary alterations to the procedures outlined in Sec. 4.2, some results of using such a "sloshing ion" distribution containing only trapped particles will be presented. We will examine how this particular distribution can destabilize the shear Alfvén plane waves found "at infinity" in the ballooning mode equation and show that a second distribution containing both trapped and passing energetic particles removes this instability but gives rise to a different type of unstable solution to the same equation. Finally, a simple analytic treatment of the eigenmode equations is carried out in order to determine the requirements on the sloshing ion distribution needed for stability. In Sec. 4.4.f we summarize our results regarding sloshing ions and discuss possibilities for future work.

4.2 Basic Equations and Numerical Model

We return to Eq. (3.1), again assuming high mode number, low frequency ($\omega < \omega_d$), and high bounce frequency ($\omega_b \gg \omega_d, \omega$). Because of the periodicity constraints in the tokamak geometry, however, we must apply the ballooning mode transformation^{8,9} before an eikonal representation can be used. The result of this procedure is that the same equations must be solved, but the variable along the field, ψ , is extended to cover the range $-\infty < \psi < +\infty$. As described in Refs. 8 and 9, the actual eigenfunctions can be reconstructed using the functions obtained in the solution of the transformed equation. With these variations in mind, we set $\varphi = XB$ in Eq. (3.1) and vary with respect to φ^* and Q_L^* so that

$$\begin{aligned}
 & \mathbf{B} \cdot \nabla \left[\frac{\sigma |\nabla S|^2}{B^2} (\mathbf{B} \cdot \nabla \varphi) \right] + \sigma \mathbf{B} \hat{e} \cdot \underline{\kappa} (Q_L - \frac{\sigma}{\tau} \varphi \mathbf{B} \hat{e} \cdot \underline{\kappa}) \\
 & + \varphi \mathbf{e} \hat{e} \cdot \underline{\kappa} \left(\frac{\sigma}{\tau} \hat{e} \cdot \hat{\nabla} P_{\perp} + \hat{e} \cdot \hat{\nabla} P_{\parallel} \right) + \omega (\omega - \omega_{*i}) \frac{|\nabla S|^2}{V_A^2} \varphi \\
 & = m_h \int d^3v \frac{\omega - \omega_*}{\omega - \langle \omega_d \rangle} \frac{\partial F_h}{\partial E} v_{\parallel}^2 \hat{e} \cdot \underline{\kappa} (\langle v_{\parallel}^2 \hat{e} \cdot \underline{\kappa} \varphi + \mu Q_L \rangle), \quad (4.1a)
 \end{aligned}$$

and

$$\tau(Q_L - \frac{\sigma}{\tau} \phi B \hat{e} \cdot \underline{\kappa}) = m_h \int d^3v \frac{\omega - \omega_*}{\omega - \langle \omega_d \rangle} \frac{\partial F_h}{\partial E} \mu (\langle v_{\parallel}^2 \hat{e} \cdot \underline{\kappa} \phi + \mu Q_L \rangle), \quad (4.1b)$$

where ϕ represents the perturbed electrostatic potential, and Q_L is the parallel (to the equilibrium field) perturbed magnetic field in the Lagrangian frame. Note that we have dropped the Q_L contribution to the inertia term; since we will not be considering purely magnetic modes, it is not necessary and can be dropped using the ordering employed in deriving Eq. (3.1). Finally, a term representing the total ion diamagnetic drift has been included,

$$\omega_{*i} = \frac{-B}{m_i n_i} \sum_j \frac{\hat{e} \cdot \nabla P_{\perp j}}{\Omega_j}.$$

This follows from the result of Catto, Hastie, and Connor⁶⁷ if higher order finite Larmor radius terms (ω_g and ω_k in their work) are neglected.

Since the energetic particles are trapped in a rather shallow magnetic well, their parallel pressures and velocities are much smaller than the perpendicular values. In particular, it can be shown that $v_{\parallel}^2 \sim (r/R) v_{\perp}^2$ (r and R are the minor and major radii of the torus, respectively). These quantities then enter into the equation a factor of order $\sim r/R$ smaller than the dominant terms. Thus, we can reasonably neglect the parallel velocity and

pressure effects for the trapped particles, resulting in a significantly simplified set of equations,

$$\begin{aligned} \mathbf{B} \cdot \nabla \left[\frac{\sigma |\nabla S|^2}{B^2} (\mathbf{B} \cdot \nabla \varphi) \right] + \sigma \mathbf{B} \hat{e} \cdot \underline{\kappa} (Q_L - \frac{\sigma}{\tau} \varphi \mathbf{B} \hat{e} \cdot \underline{\kappa}) \\ + \varphi \hat{e} \cdot \underline{\kappa} \left(\frac{\sigma}{\tau} \hat{e} \cdot \hat{\nabla} P_{\perp} + \hat{e} \cdot \hat{\nabla} P_{\parallel, c} \right) + \omega (\omega - \omega_{*i}) \frac{|\nabla S|^2}{V_A^2} \varphi = 0, \end{aligned} \quad (4.2a)$$

$$\tau (Q_L - \frac{\sigma}{\tau} \varphi \mathbf{B} \hat{e} \cdot \underline{\kappa}) = m_h \int d^3 v \frac{\omega - \omega_*}{\omega - \langle \omega_d \rangle} \frac{\partial F_h}{\partial E} \mu^2 \langle Q_L \rangle. \quad (4.2b)$$

Because of the remaining integral term in Eq. (4.2b), these equations are still very difficult to solve analytically. However, some progress can be made if the trapped particles are assumed to be deeply trapped;^{95,100,103} that is, the bounce averages cover only a short distance along the field line, and we can assume for some variable, α : $\langle \alpha \rangle \approx \alpha(s=s_0)$, where s_0 is the center point of the bounce trajectory. Also evaluating the velocity integral can be facilitated if it is appropriate to assume $\omega \ll \langle \omega_d \rangle$. This procedure was implemented by Rosenbluth et al.³⁹ and by Connor et al.⁶⁹ to obtain a simplified numerical model. Their results indicated that the energetic particles could indeed stabilize the MHD-like ballooning modes ($\omega \ll \langle \omega_d \rangle$) and allow access to the second-stability region.¹⁶⁻¹⁹ Since we seek to treat modes having

$\omega \lesssim \langle \omega_d \rangle$ (the precessional drift-resonant instability) as well as the more familiar case in which $\omega \ll \langle \omega_d \rangle$, their approach is not valid. We would also like to be able to consider distribution functions containing large percentages of nearly marginally-trapped particles (sloshing ion distributions); thus, the deeply trapped approximation is not applicable either. As a result, we must numerically solve Eqs. (4.2a) and (4.2b) as they are written above.

Some simplicity is achieved by considering a large aspect ratio equilibrium in which the flux surfaces are shifted circles.^{8,9,16,17,39,104} If the plasma beta is small with a sharp gradient, reasonable results can be obtained analytically for the various equilibrium quantities needed. We write the magnetic field in the Clebsch form, $\underline{B} = \underline{\nabla}\psi \times \underline{\nabla}\beta$. ψ is the solution of the anisotropic equilibrium equation derived by Grad,¹⁰⁵

$$R^2 \underline{\nabla} \cdot (R^{-2} \underline{\nabla} \psi) + \underline{\nabla} \psi \cdot \underline{\nabla} \ln \sigma = - \frac{1}{\sigma^2} \frac{\partial G}{\partial \psi} - \frac{R^2}{\sigma} \frac{\partial P_{\parallel}}{\partial \psi}, \quad (4.3)$$

where R is the cylindrical coordinate representing the major radius of the torus, $G = 1/2(\sigma R B_T)^2$ (B_T is the toroidal component of the magnetic field; note that G is a function of ψ only), and $\sigma = 1 + (P_{\perp} - P_{\parallel})/B^2$. We will use a flux coordinate system (ψ, ϑ, ζ) to describe the equilibrium. The eikonal S is usually written in the form

$$S = n(q\psi - \zeta), \quad (4.4)$$

with

$$\underline{B} = \underline{\nabla}\psi \times \underline{\nabla}\beta = \underline{\nabla}\psi \times \underline{\nabla}(q\psi - \zeta);$$

we assume $\underline{\nabla}S = n\underline{\nabla}\beta$, although S is in general also a function of ψ . To determine an expression for $\underline{k}_\perp = \underline{\nabla}S$, we need to calculate $\underline{\nabla}\psi$ so that we can use Eq. (4.4). Equivalently, we can calculate $\underline{\nabla}\beta$. Clearly,

$$\underline{\nabla}\beta = \frac{\underline{B} \times \underline{\nabla}\psi}{|\underline{\nabla}\psi|^2} + \lambda \underline{\nabla}\psi, \quad (4.5)$$

and it can be shown³⁰ that λ is given by

$$\underline{B}_p \cdot \underline{\nabla}\lambda = \underline{\nabla} \cdot \left(\frac{B_T}{R} \frac{\underline{\nabla}\psi}{|\underline{\nabla}\psi|^2} \right), \quad (4.6)$$

where B_p is the poloidal component of the magnetic field.

To solve the equilibrium equation, we will assume large aspect ratio ($r/R \ll 1$), low β ($\beta \ll 1$), and localized gradients [$\Delta \equiv (\underline{\nabla} \ln P)^{-1} \ll r$], so that the flux surfaces are, to first

order in $\varepsilon=r/R$, shifted circles.^{8,9,16,17,39,104} We use a coordinate system in which $R = R_0 + r\cos\vartheta$ and expand ψ in powers of ε :

$$\psi(r, \vartheta) = \psi_0(r) + \psi_1(r, \vartheta) + \dots \quad (4.7)$$

In this coordinate system, $B_T \approx B_{T0}(1 - \varepsilon \cos\vartheta)$, $B_p = B_{p0}(r) + O(\varepsilon)$, $B_{p0} = (d\psi_0/dr)/R_0$, $B_p/B_T \sim O(\varepsilon)$, and the safety factor $q = rB_{T0}/R_0B_{p0} + O(\varepsilon)$. First, we note that the term $\nabla\psi \cdot \nabla \ln \sigma$ in Eq. (4.3) is $\sim \varepsilon^2$ smaller than $(R^2/\sigma)\partial P_{\parallel}/\partial\psi$, so that it may be dropped. Except in $G(\psi)$, we can set $\sigma=1$ due to the low β and short gradient scale length approximations. Using these results, we can now write

$$\begin{aligned} R^2 \nabla \cdot (R^{-2} \nabla \psi) = & - \frac{\partial}{\partial\psi} (G + R_0^2 P_c) - 2rR_0 \cos\vartheta \frac{\partial P_c}{\partial\psi} \\ & - R_0^2 \left(1 + 2\frac{r}{R_0} \cos\vartheta \right) \frac{\partial P_{\parallel h}}{\partial\psi} + O(\varepsilon^2). \end{aligned} \quad (4.8)$$

The subscript c refers to the isotropic core plasma, h to the energetic trapped component. We add and subtract

$$\frac{\partial P_{\parallel h}}{\partial\psi} = \frac{1}{2\pi} \int_0^{2\pi} d\vartheta \frac{\partial P_{\parallel h}}{\partial\psi}$$

in Eq. (4.8); it will be seen later that this allows $\psi_1(r, \vartheta)$ to be periodic in ϑ . So,

$$R^2 \nabla \cdot (R^{-2} \nabla \psi) = -\frac{\partial}{\partial \psi} (G + R_0^2 P_c) - R_0^2 \overline{\frac{\partial P_{\parallel h}}{\partial \psi}} \quad (4.9)$$

$$- 2rR_0 \cos \vartheta \frac{\partial P_c}{\partial \psi} - R_0^2 \left(\frac{\partial P_{\parallel h}}{\partial \psi} - \overline{\frac{\partial P_{\parallel h}}{\partial \psi}} \right) + O(\varepsilon^2),$$

where we have assumed that $\partial P_{\parallel h} / \partial \psi \sim \varepsilon \partial P_c / \partial \psi$; this follows from the trapped particle nature of the hot species with the understanding that $P_{\parallel h} \sim P_c$.

We define the lowest-order part of the right hand side of Eq. (4.9):

$$J(\psi) \equiv \frac{\partial}{\partial \psi} (G + R_0^2 P_c) + R_0^2 \overline{\frac{\partial P_{\parallel h}}{\partial \psi}}.$$

Then,

$$R^2 \nabla \cdot (R^{-2} \nabla \psi_0) = -J(\psi_0), \quad (4.10a)$$

and

$$R^2 \nabla \cdot (R^{-2} \nabla \psi_1) = -2rR_0 \cos \vartheta \frac{\partial P_c}{\partial \psi}(\psi_0)$$

$$- R_0^2 \left(\frac{\partial P_{\parallel h}}{\partial \psi} - \overline{\frac{\partial P_{\parallel h}}{\partial \psi}} \right) - \psi_1 \frac{\partial J}{\partial \psi}(\psi_0). \quad (4.10b)$$

It can be shown that the last term in Eq. (4.10b) is smaller than the others by a factor of Δ/r , and can be neglected in our approximation. Using similar orderings, we find that

$$\nabla \cdot \left(\frac{B_T \nabla \psi}{R |\nabla \psi|^2} \right) = \frac{1}{r R_0} \frac{\partial q}{\partial r} - \frac{B_{T0}}{R_0^3 B_{p0}^3} \frac{1}{r} \frac{\partial}{\partial r} \left(r \frac{\partial \psi_1}{\partial r} \right) + O\left(\varepsilon \frac{\Delta}{r}\right). \quad (4.11)$$

Then, from Eqs. (4.6), (4.10b) and (4.11),

$$\begin{aligned} \lambda = & \frac{1}{B_{p0} R_0} \frac{\partial q}{\partial r} (\vartheta - \vartheta_k) + \frac{2 B_{T0} r^2}{R_0^2 B_{p0}^3} \frac{\partial P_c}{\partial \psi} (\sin \vartheta - \sin \vartheta_k) \\ & + \frac{B_{T0} r}{R_0 B_{p0}^3} \int^{\vartheta} d\vartheta' \frac{\partial}{\partial \psi} (P_{\parallel h} - \overline{P_{\parallel h}}); \end{aligned} \quad (4.12)$$

here, ϑ_k is introduced as the origin of the integrations and represents the radial wavenumber. It will be convenient to write the trapped particle pressure functions in the form

$$P_{\parallel h}(\vartheta) = 2 \hat{P}_{\perp h} \rho(\psi) (r/R_0) p_{\parallel}(\vartheta) \quad (4.13a)$$

and

$$P_{\perp h}(\vartheta) = \hat{P}_{\perp h} \rho(\psi) p_{\perp}(\vartheta), \quad (4.13b)$$

with $p_{\perp}(\vartheta=0)=1$, $p_{\parallel, \perp}(|\vartheta \bmod 2\pi| > \vartheta_0) \equiv 0$, and $\rho(\psi)$ containing all of the radial dependence. It follows that

$$\lambda \nabla \psi = \frac{q}{r} \{ S(\vartheta - \vartheta_k) - \alpha_c (\sin \vartheta - \sin \vartheta_k) - \alpha_h [g(\vartheta) - g(\vartheta_k)] \} \hat{r} + O(\varepsilon), \quad (4.14)$$

where

$$S \equiv \frac{r}{q} \frac{\partial q}{\partial r},$$

$$\alpha_c \equiv - \frac{2r^2}{B_{p0}} \frac{\partial P_c}{\partial \psi},$$

$$\alpha_h \equiv - \frac{2r^2}{B_{p0}} \hat{P}_{\perp h} \frac{\partial \rho}{\partial \psi},$$

$$g(\vartheta) = \begin{cases} p(\tilde{\vartheta}) - \frac{\tilde{\vartheta}}{\pi} p(\vartheta_0) & 0 < \tilde{\vartheta} < \vartheta_0 \\ (1 - \frac{\tilde{\vartheta}}{\pi}) p(\vartheta_0) & \vartheta_0 < \tilde{\vartheta} < 2\pi - \vartheta_0 \quad \tilde{\vartheta} = \vartheta \bmod 2\pi, \\ (\frac{2\pi - \tilde{\vartheta}}{\pi}) p(\vartheta_0) - p(2\pi - \tilde{\vartheta}) & 2\pi - \vartheta_0 < \tilde{\vartheta} < 2\pi \end{cases}$$

and

$$p(\vartheta) = \int_0^{\vartheta} d\vartheta' p_{\parallel}(\vartheta').$$

Finally,

$$\nabla\beta = \frac{g}{r} [\hat{\vartheta} + h(\vartheta)\hat{r}], \quad (4.15)$$

$$\text{with } h(\vartheta) = S(\vartheta - \vartheta_k) - \alpha_c(\sin\vartheta - \sin\vartheta_k) - \alpha_h[g(\vartheta) - g(\vartheta_k)].$$

The next section of this chapter will examine trapped particle distributions that are peaked near $\vartheta=0$. We will model this situation using the same distribution function as in Chapter III; namely,

$$F_h[\mu, E, \psi(r)] = \begin{cases} \alpha_F \left[1 - \frac{(r-r_0)^2}{\Delta r^2} \right] (\mu B_c - E) e^{-E/t} & \frac{E}{B_c} < \mu < \frac{E}{B_{\min}} \\ 0 & 0 < \mu < \frac{E}{B_c} \end{cases} \quad (4.16)$$

where

$$\alpha_F = \frac{4\hat{P}_{1h}}{m_h \sqrt{2\pi T}^{7/2}} \frac{1}{\left(1 - \frac{B_{\min}}{B_c}\right)^{3/2} \left(1 + \frac{4B_c}{B_{\min}}\right)},$$

$B_{\min}=B(\vartheta=0)$, $B_c=B(\vartheta=\vartheta_0)$, and ϑ_0 represents the maximum extent of the hot particles in $\vartheta \bmod 2\pi$. The expressions for the various moments of this distribution are as in Chapter III; in particular, note that to within factors of order ε , $p_{\perp}(\vartheta) \approx (\cos\vartheta - \cos\vartheta_0)^{3/2} / (1 - \cos\vartheta_0)^{3/2}$.

Before inserting these equilibrium functions into Eqs. (4.2a) and (4.2b), we note that numerical solution of the equations will be simplified if we change to new variables,

$$\delta Q \equiv Q_L - \frac{\sigma}{\tau} \varphi B \hat{e} \cdot \underline{\kappa}$$

$$\phi \equiv (1+h^2)^{1/2} \varphi;$$

note that $\delta Q=0$ in regions where there are no energetic particles.

Thus, Eqs. (4.2a) and (4.2b) become

$$\begin{aligned} D_{op} \phi &\equiv \sigma \frac{d^2 \phi}{d\vartheta^2} - \frac{\sigma \phi}{1+h^2} \left[\frac{(dh/d\vartheta)^2}{(1+h^2)} + h \frac{d^2 h}{d\vartheta^2} \right] + \left(\frac{d\phi}{d\vartheta} - \frac{h \frac{dh}{d\vartheta} \phi}{1+h^2} \right) \frac{d\sigma}{d\vartheta} \\ &+ \frac{\phi}{(1+h^2)} D(\vartheta) \left\{ \frac{\alpha_c}{2} \left(1 + \frac{\sigma}{\tau} \right) + \frac{\alpha_h}{2} \frac{\sigma}{\tau} p_{\perp}(\vartheta) \right\} + \frac{q^2 R_0^2}{V_A^2} \omega (\omega - \omega_{*i}) \phi \\ &= - \frac{qrR_0 \sigma D(\vartheta)}{(1+h^2)^{1/2}} \delta Q, \end{aligned} \quad (4.17a)$$

and

$$\tau \delta Q = m_h \int d^3v \frac{\omega - \omega_*}{\omega - \langle \omega_d \rangle} \mu^2 \frac{\partial F_h}{\partial E} \left[\langle \delta Q \rangle + \frac{q}{r R_0} \langle \frac{\sigma}{\tau} \frac{D(\vartheta) \phi}{(1+h^2)^{1/2}} \rangle \right], \quad (4.17b)$$

where $D(\vartheta) = \cos \vartheta + h(\vartheta) \sin \vartheta$. We write ω_{*i} as

$$\omega_{*i} = -\omega_{*0} \left(\alpha_c + 2 \frac{Z_i m_h}{Z_h m_i} \left\{ \frac{(1-\tau)}{\tau} [\alpha_c - 2\sigma q^2 D(\vartheta)] + \frac{\alpha_{h\perp} P_{\perp}(\vartheta)}{\tau} \right\} \right),$$

$$\frac{\omega_{*0}}{\omega_A} = \frac{n V_A}{4r \Omega_i}, \quad \omega_A = \frac{V_A}{q R_0}.$$

To solve Eqs. (4.17a) and (4.17b), we expand δQ and ϕ ,

$$\delta Q = \sum_{\ell=1}^{\infty} q_{\ell} f_{\ell}(\vartheta) \quad (4.18a)$$

$$\phi = \phi_h(\vartheta) + \sum_{\ell=1}^{\infty} q_{\ell} \phi_{\ell}(\vartheta), \quad (4.18b)$$

with

$$f_{\ell}(\vartheta) \equiv \begin{cases} \cos \left[(2\ell-1) \frac{\pi \tilde{\vartheta}}{2\vartheta_0} \right] & |\tilde{\vartheta}| < \vartheta_0 \\ 0 & |\tilde{\vartheta}| > \vartheta_0 \end{cases} \quad \tilde{\vartheta} = \vartheta \bmod 2\pi;$$

ϕ_h and the ϕ_ℓ 's are found by integrating

$$D_{op} \phi_h = 0, \quad (4.19a)$$

$$D_{op} \phi_\ell = \frac{qrR_0 D(\vartheta)}{(1+h^2)^{1/2}} \delta Q \quad (4.19b)$$

over each 2π region in the range of ϑ , $0 < \vartheta < \infty$. Eq. (4.19a) is integrated with $\phi_h = \phi$ and $d\phi_h/d\vartheta = d\phi/d\vartheta$ at the beginning of an integration over one period. The same is done with Eq. (4.19b), but $\phi_\ell = 0$ and $d\phi_\ell/d\vartheta = 0$ are employed as initial values.

Once the functional forms of ϕ_h and ϕ_ℓ are known, they can be used to calculate the matrix elements of a set of linear equations for the q_ℓ 's obtained from Eq. (4.17b). Namely,

$$\sum_{\ell=1}^N q_\ell A_{\ell\ell'} = B_{\ell'}, \quad (4.20a)$$

$$A_{\ell\ell'} = \int_0^{\vartheta_0} d\vartheta \frac{\tau B_c}{B} f_{\ell} f_{\ell'}$$

$$+ \frac{\alpha_h}{5(1-\cos\vartheta)^{3/2} q^2 \epsilon^2} \int_1^{\lambda_m} d\lambda \lambda^{3/2} \left(\frac{\Delta_r}{R} \left[1 - \frac{(r-r_0)^2}{\Delta_r^2} \right] \frac{\omega}{\omega_{d0}} \right)^{5/2}$$

$$+ (\lambda-1) \left(\frac{\omega}{\omega_{d0}} \frac{\Delta_r}{R} \left[1 - \frac{(r-r_0)^2}{\Delta_r^2} \right] + 1 \right) I_{7/2}$$

$$\bar{f}_\ell + \frac{\overline{\phi_{\ell\tau} \frac{\sigma}{q}^2 D(\vartheta)}}{(1+h^2)^{1/2}} \quad (4.20b)$$

$$B_{\ell'} = - \frac{\alpha_h}{5(1-\cos\vartheta)^{3/2} q^2 \varepsilon^2} \int_1^{\lambda_m} d\lambda \lambda^{3/2} \left\{ \frac{\Delta_r}{R} \left[1 - \frac{(r-r_0)^2}{\Delta_r^2} \right] \frac{\omega}{\omega_{d0}} I_{5/2} \right.$$

$$\left. + (\lambda-1) \left(\frac{\omega}{\omega_{d0}} \frac{\Delta_r}{R} \left[1 - \frac{(r-r_0)^2}{\Delta_r^2} \right] + 1 \right) I_{7/2} \right\}$$

$$\times \bar{f}_\ell + \frac{\overline{\phi_{h\tau} \frac{\sigma}{q}^2 D(\vartheta)}}{(1+h^2)^{1/2}} \quad (4.20c)$$

where we have defined

$$\lambda_m = \frac{1 - \varepsilon \cos\vartheta}{1 - \varepsilon}, \quad \lambda = \frac{\mu B_c}{E} = \frac{1 - \varepsilon \cos\vartheta_0}{1 - \varepsilon \cos[\vartheta_T(\lambda)]}, \quad \omega_{d0} = \frac{nqT}{rR\Omega_h}$$

Ω_h = hot particle cyclotron frequency,

$$\bar{\alpha} \equiv \frac{1}{2} \int_{-\vartheta_T(\lambda)}^{\vartheta_T(\lambda)} d\vartheta \frac{\alpha(\vartheta)}{\sqrt{\cos\vartheta - \cos\vartheta_T}}$$

$$I_{5/2} = \frac{1}{\sqrt{\pi}} \int_0^{\infty} \frac{dz z^{5/2} e^{-z}}{I_1 \frac{\omega}{\omega_{d0}} + \lambda z f(\lambda)},$$

$$I_{7/2} = \frac{1}{\sqrt{\pi}} \int_0^{\infty} \frac{dz z^{7/2} e^{-z}}{I_1 \frac{\omega}{\omega_{d0}} + \lambda z f(\lambda)}.$$

Using the methods described in Chapter III, we can calculate

$$\frac{1}{\sqrt{\pi}} \int_0^{\infty} \frac{dz z^{5/2} e^{-z}}{a - z} = - \left[\frac{3}{4} + \frac{a}{2} + a^2 + a^{5/2} Z(a^{1/2}) \right],$$

$$\frac{1}{\sqrt{\pi}} \int_0^{\infty} \frac{dz z^{7/2} e^{-z}}{a - z} = - \left[\frac{15}{8} + \frac{3a}{4} + \frac{a^2}{2} + a^3 + a^{7/2} Z(a^{1/2}) \right].$$

$f(\lambda)$ and I_1 arise in calculating $\langle \omega_d \rangle / \omega_{d0}$ and can be expressed as

$$f(\lambda) = I_2 + S I_3 - \alpha_c \left(I_4 + \frac{I_1 + I_1'}{2q^2} \right) - \alpha_h \left(I_5 + \frac{1}{2q^2} I_6 \right), \quad (4.21)$$

with

$$I_1 = \int_0^{\vartheta_T} \frac{d\vartheta}{\sqrt{\cos\vartheta - \cos\vartheta_T}} = \sqrt{2} K(k),$$

$$I_1' = \int_0^{\vartheta_T} \frac{d\vartheta}{\sqrt{\cos\vartheta - \cos\vartheta_T}} \frac{1 - \tau}{\tau} \rightarrow 0,$$

$$I_2 = \int_0^{\vartheta_T} \frac{d\vartheta \cos\vartheta \sigma/\tau}{\sqrt{\cos\vartheta - \cos\vartheta_T}} \rightarrow \sqrt{2}[2E(k) - K(k)],$$

$$I_3 = \int_0^{\vartheta_T} \frac{d\vartheta \vartheta \sin\vartheta \sigma/\tau}{\sqrt{\cos\vartheta - \cos\vartheta_T}} \rightarrow 4\sqrt{2}[(k^2 - 1)K(k) + E(k)],$$

$$I_4 = \int_0^{\vartheta_T} \frac{d\vartheta \sin^2\vartheta \sigma/\tau}{\sqrt{\cos\vartheta - \cos\vartheta_T}} \rightarrow \frac{4\sqrt{2}}{3} [(1 - k^2)K(k) + (2k^2 - 1)E(k)],$$

$$I_5 = \int_0^{\vartheta_T} \frac{d\vartheta \sin\vartheta g(\vartheta) \sigma/\tau}{\sqrt{\cos\vartheta - \cos\vartheta_T}},$$

and

$$I_6 = \int_0^{\vartheta_T} \frac{d\vartheta p_{\perp}(\vartheta)}{\sqrt{\cos\vartheta - \cos\vartheta_T}} \frac{1}{\tau}.$$

$E(k)$ and $K(k)$ are the elliptic integrals defined by

$$E(k) = \int_0^{\pi/2} d\gamma (1 - k^2 \sin^2\gamma)^{1/2},$$

and

$$K(k) = \int_0^{\pi/2} \frac{d\gamma}{(1 - k^2 \sin^2\gamma)^{1/2}},$$

where $k = \sin(\vartheta_T/2)$. The arrows above indicate that the closed-form

expressions are valid only in the limit $\sigma=\tau=1$. In general, these quantities must be computed numerically.

We now describe the boundary conditions to be applied at infinity. The integrations of Eqs. (4.17a) and (4.17b) are started at some large value of ϑ , $\vartheta_m=2\pi m$, $m=\text{integer}$. The secular term in $h(\vartheta)$ is evaluated at ϑ_m ,

$$h(\vartheta) \approx S(\vartheta_m - \vartheta_k) - \alpha_c(\sin\vartheta - \sin\vartheta_k) - \alpha_h[g(\vartheta) - g(\vartheta_k)]; \quad (4.22)$$

a valid approximation for $|\vartheta - \vartheta_m| < 2\pi$ and $\vartheta_m \gg 2\pi$. Thus, with an error of order $1/\vartheta_m$, the coefficients of the differential equation (4.17a) are purely periodic so that Floquet theory^{106,107} can be applied; the solutions must be of the form

$$\phi(\vartheta) = \hat{\phi}(\vartheta)e^{ik\vartheta}, \quad (4.23)$$

with $\hat{\phi}(\vartheta)$ a function of period 2π , and k some complex constant. Note that k is actually a function of ϑ_m , $k(\vartheta_m)$, as is the function $\hat{\phi}(\vartheta)$. However, in the limit $\vartheta_m \rightarrow \infty$, k becomes a constant. This suggests an analogy with WKB theory in which the solution can be expressed in the form

$$\phi(\vartheta) = \hat{\phi}(\vartheta)\exp\left[i\int^{\vartheta} k(\vartheta')d\vartheta'\right], \quad (4.24)$$

where now $\hat{\phi}$ is roughly periodic with period 2π and changes over larger scale lengths. If we write

$$\int^{\vartheta} k(\vartheta') d\vartheta' = \int^{\vartheta_m} k(\vartheta') d\vartheta' + \int_{\vartheta_m}^{\vartheta} k(\vartheta') d\vartheta',$$

treat the first piece as a constant, and expand $k(\vartheta')$ about ϑ_m , we get

$$\int_{\vartheta_m}^{\vartheta} k(\vartheta') d\vartheta' \cong k(\vartheta_m) \cdot (\vartheta - \vartheta_m) + \frac{(\vartheta - \vartheta_m)^2}{2} \left. \frac{dk}{d\vartheta} \right|_{\vartheta_m} + \dots \quad (4.25)$$

The first term is the piece we pick up in expressing $\phi(\vartheta)$ as in Eq. (4.23) and provides a local approximation to the global WKB-like solution at ϑ_m .

To calculate k , we first integrate Eqs. (4.17a) and (4.17b), using Eq. (4.22) for $h(\vartheta)$, over $\vartheta_{m-} \equiv \vartheta_m - \pi$ to $\vartheta_{m+} \equiv \vartheta_m + \pi$ starting with $\phi(\vartheta_{m-})=0$, $\frac{d\phi}{d\vartheta}(\vartheta_{m-})=1$, and label the resulting values at ϑ_{m+} , $\phi_1 \equiv \phi(\vartheta_{m+})$, $\phi'_1 \equiv \frac{d\phi}{d\vartheta}(\vartheta_{m+})$. Similarly, we integrate from $\vartheta_{m+} \rightarrow \vartheta_{m-}$ with $\phi(\vartheta_{m+})=0$, $\frac{d\phi}{d\vartheta}(\vartheta_{m+})=1$ to get $\phi_2 \equiv \phi(\vartheta_{m-})$ and $\phi'_2 \equiv \frac{d\phi}{d\vartheta}(\vartheta_{m-})$. Using the expression for ϕ given in Eq. (4.23), it can be shown that

$$k(\vartheta_m) = \frac{i}{2\pi} \ln \left\{ \frac{(\phi'_2 - \phi_2 \frac{\phi'_1}{\phi_1}) \pm [(\phi'_2 - \phi_2 \frac{\phi'_1}{\phi_1})^2 + 4\phi_2/\phi_1]^{1/2}}{2} \right\}, \quad (4.26)$$

and we actually obtain two values for $k(\vartheta_m)$. We will be interested in temporally growing modes, so a spatially damped response is generally appropriate, $\text{Im } k > 0$. We check to see that this choice also yields outgoing waves, $\text{Re}(\partial\omega/\partial k) > 0$. These two criteria are usually compatible; if they are not, we need a special treatment, as discussed in Sec. 4.4.c. We can then find a value for $d(\ln\phi)/d\vartheta$ at ϑ_{m-} , the boundary condition at infinity we need to begin the actual integrations.

At this point, we reintroduce the secular term in $h(\vartheta)$, and go through the procedure previously described to find ϕ_h , the ϕ_1 's and q_1 's over the range $\vartheta = (2m-1)\pi$ to $(2m-3)\pi$. This process is repeated until the origin is reached. We set $\vartheta_k = 0$ and look for even eigenmodes. That is, the boundary condition we enforce at $\vartheta = 0$ is $d(\ln\phi)/d\vartheta = 0$. Odd eigenmodes could also be examined, but we do not expect them to be very interesting for two reasons. First, the most unstable MHD mode should peak near $\vartheta = 0$, at least for small values of the core pressure gradient.¹⁶ Secondly, the bounce average of ϕ in Eq. (4.17b) will vanish for $|\vartheta| \leq \vartheta_0$; hence, $\delta Q = 0$ in this region. Since this ought to be the area in which the hot particles have the greatest effect, the high frequency branch will not be as noticeable as with even modes. The eigenfrequency ω is obtained via a shooting technique. For given ω , Eqs. (4.17a) and (4.17b) are integrated from $\vartheta = \vartheta_m$ to $\vartheta = 0$; $d(\ln\phi)/d\vartheta(\vartheta = 0)$ is then a function of ω . A zero of this function is sought with a secant

method. Note that with $\alpha_h=0$, Eq. (4.17a) reduces to the standard MHD ballooning equation. For this reason, we often start at $\alpha_h=0$ with a known value of $\omega=i\gamma_{\text{MHD}}$ and increase α_h in small steps using the previous root as a guess for the eigenfrequency at the next point.

4.3 Deeply Trapped Particles

In this section we examine cases in which the particles are confined close to the minimum magnetic field region of the tokamak. For example, this is the sort of distribution that would be introduced by near-perpendicular neutral beam injection. However, perpendicular injection on PDX¹⁰⁸ led to the "fishbone" oscillations⁸⁷ which appear to be due to a precessional drift resonance of the energetic particles with the internal kink mode.⁸⁸⁻⁹¹ We will examine the effects these resonances have on high-mode-number ballooning modes in addition to the impact of the energetic particles on the nonresonant MHD ballooning mode.

Some of the parameters required to specify the problem will be fixed. Namely, we set $S=0.6$, $\alpha_c=0.8$, $r/R_0=0.2$, $r = r_0 + \Delta_r/2$, $q=2$, $m_i=m_h$, and $q_i=q_h$. These choices were made to aid comparisons with similar theoretical work published previously.^{69,93,95} The remaining parameters are ϑ_0 , ω_{d0}/ω_A , ω_{*0}/ω_{d0} , α_h , and Δ_r/r . The latter four will be varied in a systematic fashion to allow us an

understanding of how they affect the stability of the system. Note that only ω_{d0}/ω_A involves mode number. We can get an idea of what values are reasonable by using PDX-like parameters^{87,94} to estimate ω_{d0}/ω_A and ω_{*0}/ω_{d0} . With $T_i = 3$ keV, $n_i = 3 \times 10^{13}$ cm⁻³, $B = 2$ T,

$$\frac{\omega_{*0}}{\omega_{d0}} \cong (0.28) \left(\frac{100}{T_h/T_i} \right)$$

and

$$\frac{\omega_{d0}}{\omega_A} \cong (0.08) n \left(\frac{T_h}{100 \text{ keV}} \right);$$

so, for $n=10$ and $T_h = 120$ keV, one obtains $\omega_{d0}/\omega_A \cong 1$.

The ratio Δ_r/r was an expansion parameter in the equilibrium calculation; thus, we cannot allow it to be too large. In the limit of an infinitely sharp gradient, we have $\Delta_r/r \rightarrow 0$, $\hat{P}_{lh} \rightarrow 0$, but $\alpha_h \neq 0$. Although unrealistic, this limit simplifies the equations significantly. In most instances, we will simply take $\Delta_r/r=0$ and $\omega_{*0}/\omega_{d0}=0$. Unlike procedures employed elsewhere,^{69,93,95} we will raise α_h from zero, keeping α_c constant. This is a reasonable way of describing the evolution of the system as neutral beam particles are injected.

4.3.a Growth Rates of Instabilities

Figs. 4.1 and 4.2 show the imaginary and real parts of the eigenfrequency, respectively, as α_h is varied for four values of ω_{d0}/ω_A : namely, $\omega_{d0}/\omega_A =$ (i) 0.01, (ii) 0.4, (iii) 0.7, and (iv) 2.0. Also, $\nu_0=0.8955$, $\omega_{*i}/\omega_{d0}=0$, and $\Delta_r/r=0$. Since ω_{d0}/ω_A is proportional to the energetic particle temperature, and α_h is proportional to the energetic particle pressure, varying α_h at constant ω_{d0}/ω_A implies a change in the hot species density. Case (i) represents the introduction of very low energy, MHD-like, trapped particles. Kinetic effects are small in this case. The increase in the growth rate is due to the increased pressure available to drive the instability; the real part of the frequency is hardly affected at all. Note that the use of the high bounce frequency ordering may be inappropriate for this case; it is included here for purposes of comparison.

Curve (ii) of Figs. 4.1 and 4.2 describes the effects of particles with significantly more energy. Their stabilizing effect is seen at small α_h , but is overcome by the destabilizing influence of the drift resonance ($\text{Re } \omega \sim \omega_d$) at larger values. Consequently, $\text{Im } \omega$ increases with α_h for $\alpha_h \gtrsim 1.3$, and $\text{Re } \omega$ becomes significant compared to ω_d . By further increasing ω_{d0}/ω_A [curve (iii)], the distinction between these two modes becomes clearer. First, we see that we can completely stabilize the MHD ballooning mode ($\text{Re } \omega \ll \omega_d$) just before the higher frequency precessional

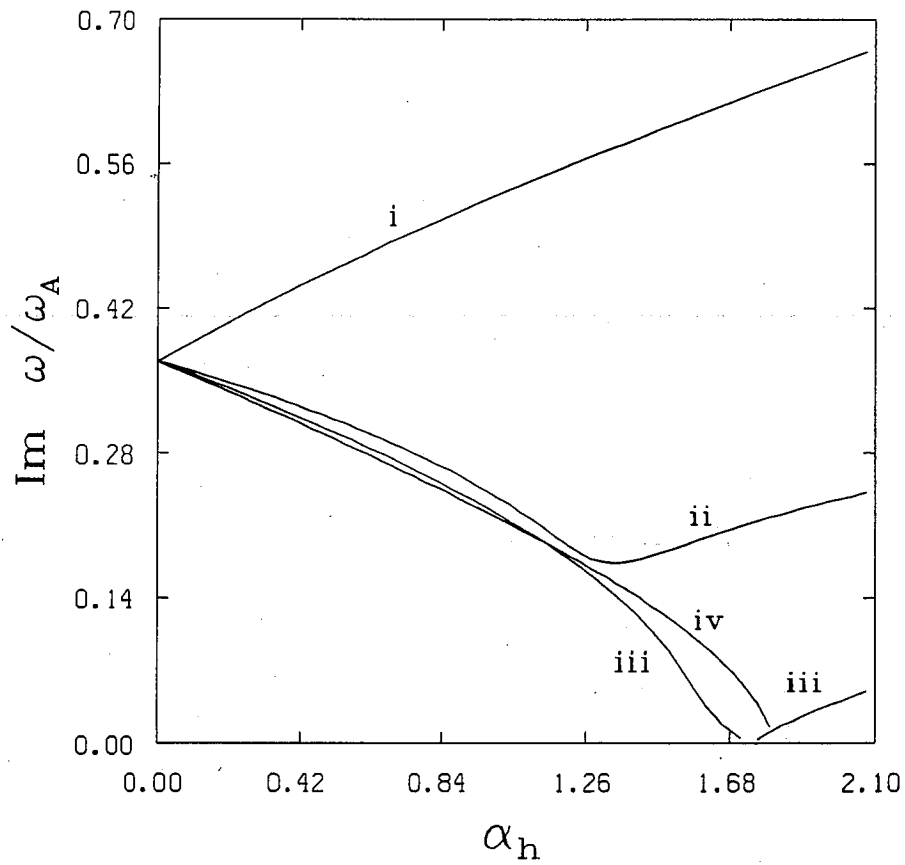


Fig. 4.1. Imaginary part of the eigenvalue plotted as a function of α_h for four values of the parameter ω_{d0}/ω_A : (i) $\omega_{d0}/\omega_A = 0.01$, (ii) $\omega_{d0}/\omega_A = 0.4$, (iii) $\omega_{d0}/\omega_A = 0.7$, and (iv) $\omega_{d0}/\omega_A = 2.0$.

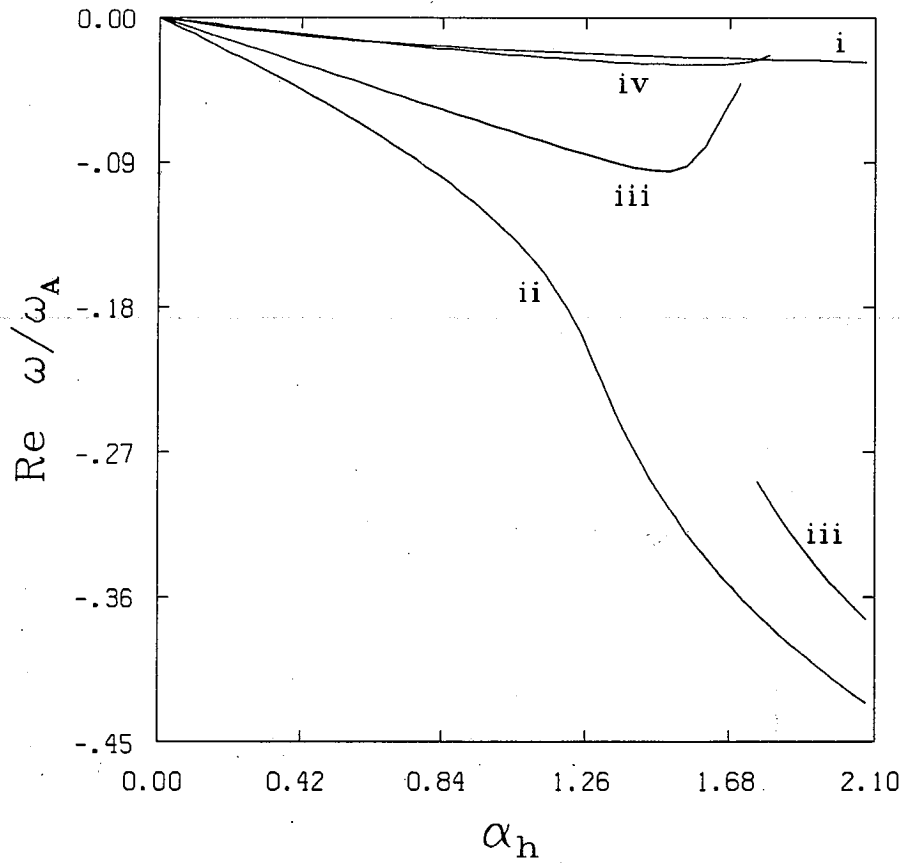


Fig. 4.2. Real part of the eigenvalue plotted as a function of α_h for four values of the parameter ω_{d0}/ω_A : (i) $\omega_{d0}/\omega_A = 0.01$, (ii) $\omega_{d0}/\omega_A = 0.4$, (iii) $\omega_{d0}/\omega_A = 0.7$, and (iv) $\omega_{d0}/\omega_A = 2.0$.

mode becomes unstable. Note the difference in the real parts of the frequencies for these two modes at $\alpha_h = 1.7$.

Finally, in case (iv) we consider very high energy particles (using the PDX values with a mode number, $n=10$, this corresponds to $T_h \approx 240$ keV). We can again completely stabilize the low frequency root, but now there is some distance in α_h before the other mode becomes unstable. The existence of such a stable window has been noted by others.^{69,93} However, instabilities that we have not considered here may be present inside this window (e.g., the gap modes described in Sec. 4.3.c).

In those situations where $\omega \ll \omega_d$ and $\vartheta_0 \lesssim \pi/2$, it can be seen that the contribution arising from the kinetic term, Eq. (4.17b), almost exactly cancels the hot particle contribution to the instability drive term in Eq. (4.17a).^{69,95} Furthermore, as long as α_c is nonzero and $\phi(\vartheta=0)$ is a local maximum of the eigenfunction, the portion of the kinetic contribution which is not cancelled by the fluid term proportional to α_h counteracts the destabilizing influence of the core pressure piece of the instability drive. Due to the stabilizing shear effects present in a tokamak, the requirements on α_h to do this effectively are not as strict as in a shear-free system such as EBT where the energetic particle pressure gradient must be sufficient to reverse the local magnetic field gradient.

The high frequency ($\omega \lesssim \omega_d$) instability is introduced as a result of the negative energy character of the hot particle precessional mode⁴²⁻⁴⁵ arising out of the kinetic term in Eq. (4.17b). By coupling this mode to positive energy waves or positive dissipation, the negative energy wave can be destabilized; here, the outgoing-wave boundary condition plays the part of positive dissipation.¹⁰⁹ The strength of the coupling is proportional to α_h ($\delta Q \propto \alpha_h$); so, the growth rate of this mode tends to increase as the hot particle pressure gradient is raised.

However, at the same time, the resonant character of the kinetic term provides a source of negative dissipation since $\partial F / \partial \psi < 0$ in the region being studied.¹¹⁰ The stability of the high frequency mode is determined by the balance between the positive and negative dissipation. At low energetic particle temperatures, the former, depending mostly on properties of the background plasma, prevails and gives rise to instability if α_h is large enough. By raising the energy of the trapped particles, the balance is altered favorably, causing a drop in or even a disappearance of the growth rate. A more quantitative analytic description of this instability will be given in Sec. 4.4.d.

4.3.b Stability Window

The fact that the mechanism for stabilizing the MHD ballooning root becomes insensitive to the value of ω_{d0}/ω_A above some threshold while the high frequency branch continues to be greatly affected allows a stability window in α_h to appear for these two modes as we raise ω_{d0}/ω_A . We now investigate quantitatively how the width of that window depends on the parameters ω_{d0}/ω_A , Δ_r/r and ω_{*0}/ω_{d0} . First, we choose a base value of $\omega_{d0}/\omega_A = 1.06$ and set $\varphi_0 = 0.785$. As shown in Fig. 4.3, this provides a region of reasonable size in which both modes are stable.

We can plot marginally stable trajectories in parameter space for each of these modes by fixing $\gamma \equiv \text{Im } \omega/\omega_A$ at some small value, say, 10^{-3} , and then solving for the corresponding $\text{Re } \omega/\omega_A$ and α_h needed to satisfy the boundary conditions. Initial points can be obtained by inspection of Fig. 4.3; guesses for the solutions at subsequent parameter values are then made by extrapolation from the previous points.

In Figs. 4.4 - 4.6, such plots are shown for various values of ω_{d0}/ω_A , Δ_r/r and ω_{*0}/ω_{d0} . The stable and unstable regions are labeled accordingly. As expected from the above discussion, increasing ω_{d0}/ω_A widens the stable window rapidly; while lowering it can close the window completely, as seen originally in Fig. 4.1.

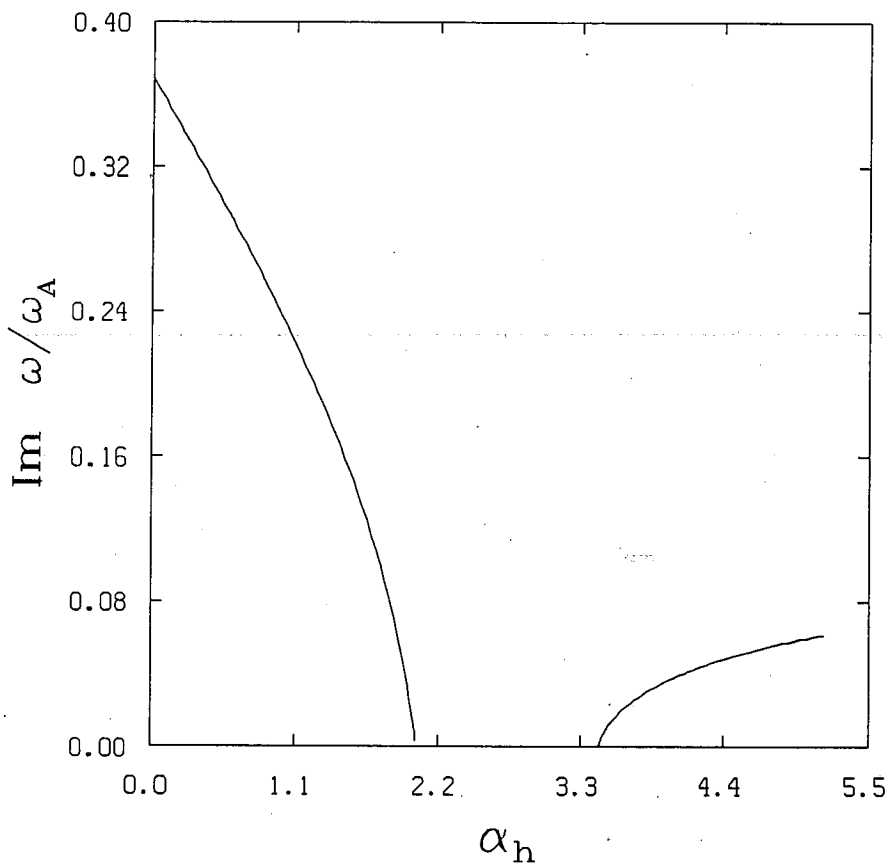


Fig. 4.3. Imaginary part of the eigenvalue plotted as a function of α_h for low-frequency, MHD (small α_h) and high-frequency, precessional (large α_h) branches with $\omega_{d0}/\omega_A=1.06$.

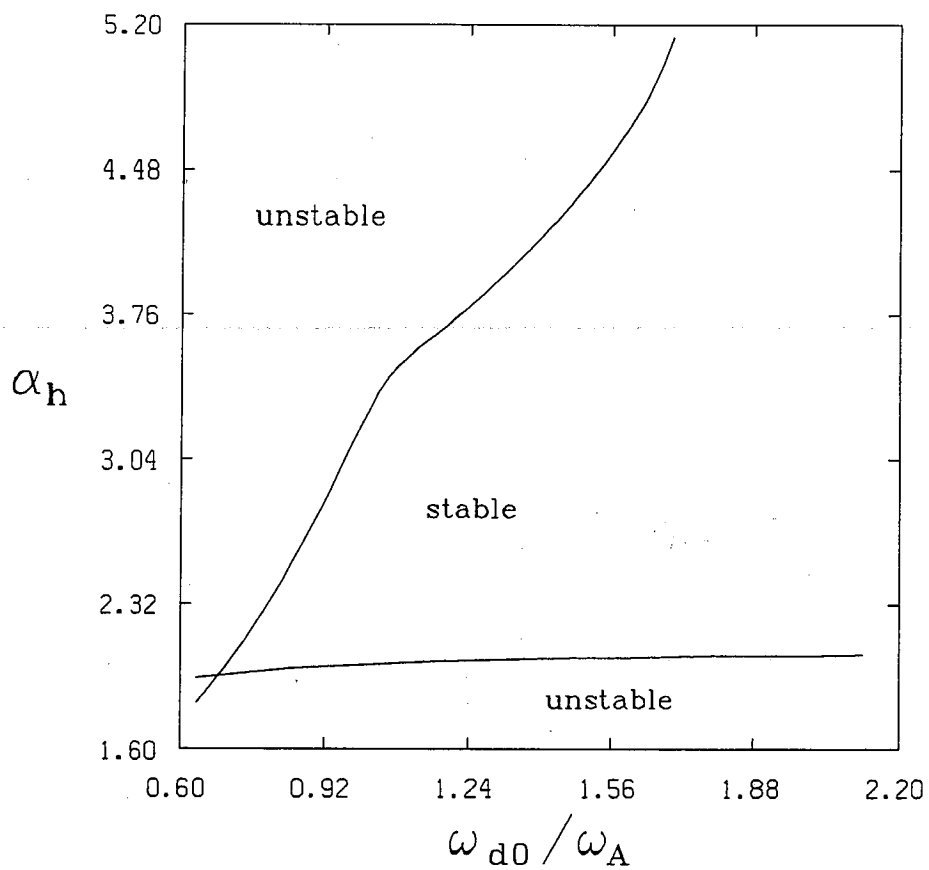


Fig. 4.4. Marginally stable ($\text{Im } \omega/\omega_A = 10^{-3}$) values of α_h for low-frequency, MHD (small α_h) and high-frequency, precessional (large α_h) branches as ω_{d0}/ω_A is varied.

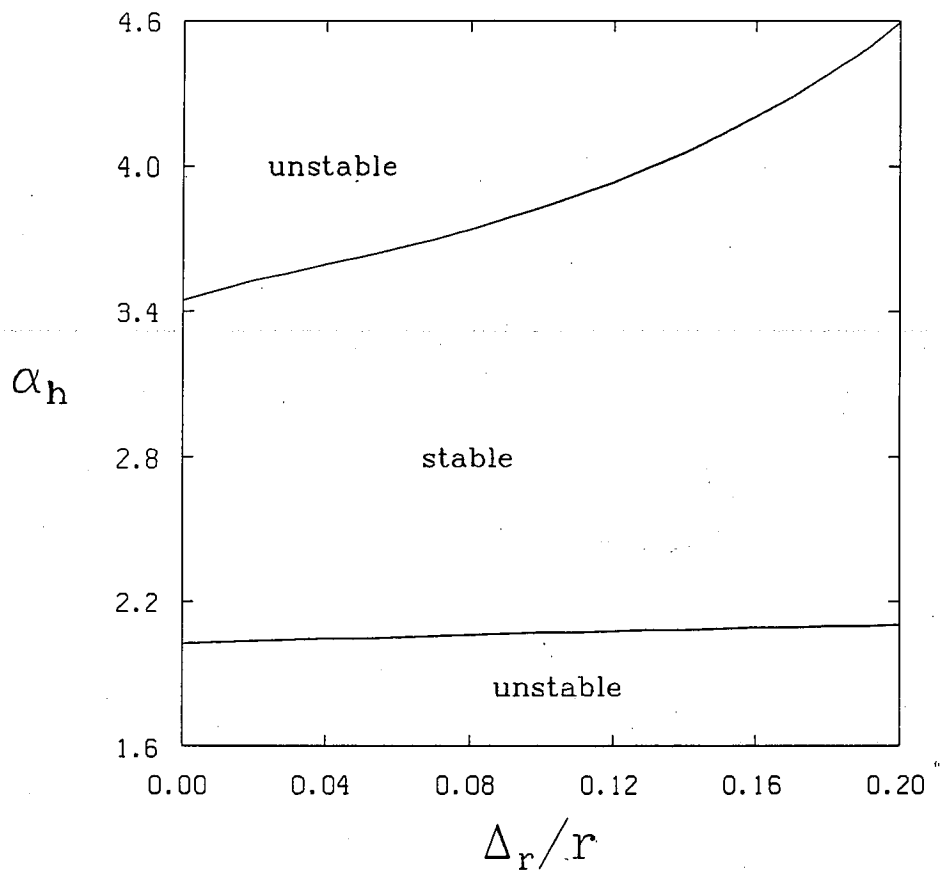


Fig. 4.5. Marginally stable ($\text{Im } \omega/\omega_A = 10^{-3}$) values of α_h for low-frequency, MHD (small α_h) and high-frequency, precessional (large α_h) branches as Δ_r/r is varied.

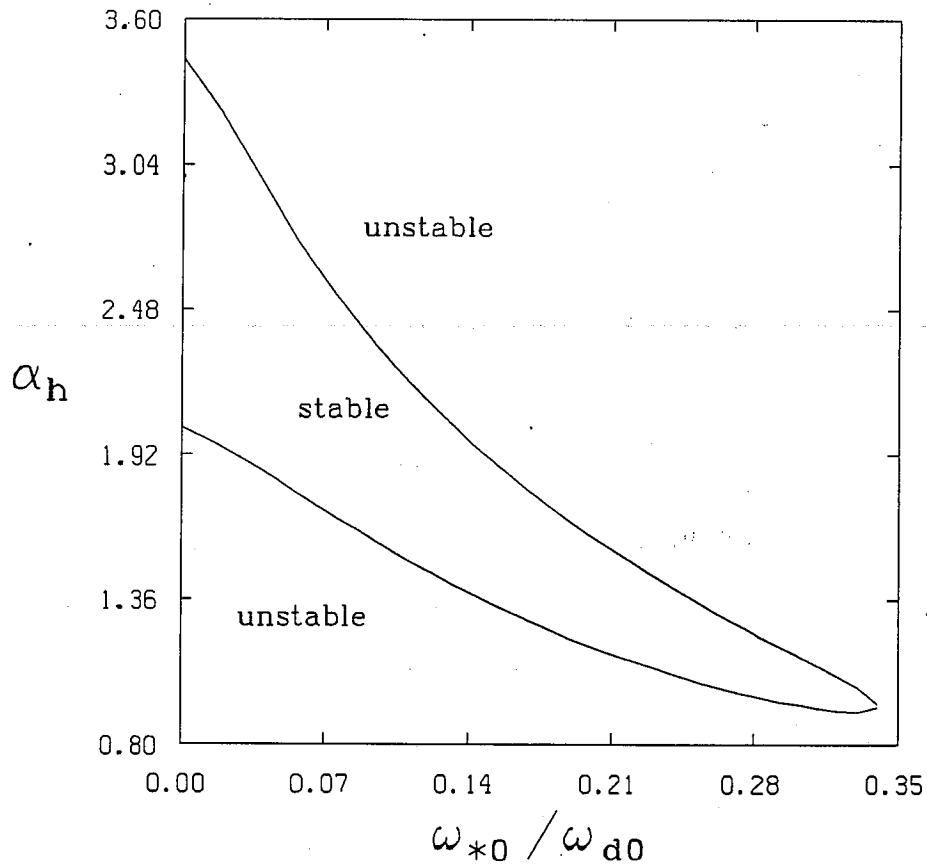


Fig. 4.6. Marginally stable ($\text{Im } \omega/\omega_A = 10^{-3}$) values of α_h for low-frequency, MHD (small α_h) and high-frequency, precessional (large α_h) branches as ω_{*0}/ω_{d0} is varied.

Heretofore, we had considered only cases in which $\Delta_r/r=0$. This effectively sets $\beta_h=0$, $\sigma=\tau=1$, but retains a finite pressure gradient. One important effect of having $\Delta_r/r \neq 0$ occurs in $\omega_d \propto 1/\tau$ [see Eq. (4.21)]. We know from looking at Fig. 4.4 that the critical α_h for the stabilization of the ballooning root is largely independent of the value of ω_{d0} and, hence, of ω_d (since ω_{d0} appears in ω_d only) for $\omega_{d0} \geq 0.6$. Thus, any change in the low frequency marginal stability point with Δ_r/r must be due to the $\omega \partial F_h / \partial E$ term in Eq. (4.17b) or to the σ/τ factors in the curvature drive term. Fig. 4.5 then tells us that these effects have little impact on the calculation. On the other hand, Fig. 4.4 suggests that increasing ω_d by raising ω_{d0} improves the stability of the high frequency branch. Reducing τ by raising Δ_r/r at constant α_h and ω_{d0} will also increase ω_d . Provided the other effects on the coefficients of the differential equation are small, we should see the critical α_h for the precessional mode go up with Δ_r/r , as indicated by Fig. 4.5. The effect over the range $\Delta_r/r = 0 - 0.2$ is not very drastic; $\Delta_r/r=0$ is the most pessimistic value. Consequently, it would be reasonable to leave $\Delta_r/r=0$ in subsequent calculations.

Finally, in Fig. 4.6, we examine the effects of ω_{*i} . Two things occur. First, with a nonzero ω_{*i} , the MHD growth rate is reduced,

$$\gamma_{\text{MHD}}' = (\gamma_{\text{MHD}}^2 - \omega_{*i}^2/4)^{1/2}. \quad (4.27)$$

As a result, a smaller amount of α_h is needed to stabilize the low frequency root. Second, when marginal stability is reached, ω has some significant real part due to ω_{*i} ; this improves the coupling of the background plasma to the negative energy wave. Thus, the critical α_h for the precessional modes drops as ω_{*i} is increased. Unfortunately, the latter process occurs more rapidly, and the window closes off for $\omega_{*0}/\omega_{d0} \gtrsim 0.34$. However, the growth rates for large α_h are smaller than those found with $\omega_{*0}/\omega_{d0} = 0$. For example, we find $\text{Im } \omega/\omega_A \lesssim 0.03$ for $\alpha_h \gtrsim 0.6$ when $\omega_{*0}/\omega_{d0} = 0.33$.

From Figs. 4.4 - 4.6, we conclude that we can find a stable window of operation if $\omega_{d0}/\omega_A \gtrsim 0.7$ and $\omega_{*0}/\omega_{d0} \lesssim 0.34$. Recall that ω_{d0}/ω_A is proportional not only to the energetic particle temperature, but also to the toroidal mode number. It is for this reason that ω_{*0}/ω_{d0} rather than ω_{*0}/ω_A is used as an input parameter; this ratio is independent of mode number. We can think of ω_{*i}/ω_d as being proportional to T_c/T_h , the core to trapped particle temperature ratio. Recalling the representative value calculated previously, $\omega_{*0}/\omega_{d0} \approx 28 T_c/T_h$, we see that to open the window effectively, we need $T_h/T_c \sim 200$. With $T_c = 3$ keV, we must have $T_h \sim 600$ keV.

On the other hand, ω_{d0}/ω_A can be reduced simply by choosing a smaller toroidal mode number. There is a limit to this; namely, n cannot be so small as to invalidate the high mode number assumption made in deriving the equations. But, by raising T_h sufficiently, we can insure that a stable window is present. For example, with $T_h = 600$ keV and $\omega_{d0}/\omega_A = 0.08 n$ ($T_h/100$ keV), as calculated previously, we see that $\omega_{d0}/\omega_A > 1$ except for $n \leq 2$; mode numbers $n \leq 2$ should be treated by other methods. Unfortunately, particles with energies of this magnitude would be hard to create with present technology. However, one should keep in mind that the alpha particles born in fusion reactions start with energies larger than this (3.5 MeV in the D-T reaction). Their effects have been considered in more detail by other authors.^{95,100}

Now, it is apparent that we can find parameters for which both the low and high frequency modes are stable. We must then investigate whether or not other unstable modes might be present. Including other interactions of the background plasma with trapped species could still provide positive energy waves or positive dissipation capable of destabilizing the negative energy precessional mode.

4.3.c Gap Modes

We will consider a different type of eigenmode that can also be described by Eqs. (4.17a) and (4.17b) and show that it can be destabilized through interactions with the energetic trapped particles. When the variation of the magnetic field strength on a magnetic surface is included in a theoretical model of axisymmetric toroidal plasma, neighboring poloidal harmonics of the continuous shear Alfvén spectrum couple together and break it into bands of continuous spectra.¹¹¹⁻¹¹³ Cheng, Chen, and Chance¹⁰² have shown, using the high- n ballooning formalism, that a discrete, stable eigenmode exists within the gap between these bands. Subsequently, Cheng and Chance¹¹⁴ described a similar treatment valid for low- n modes.

If we set $\alpha_c = \alpha_h = 0$ in Eq. (4.17a), we obtain¹⁰² approximately,

$$\left[\frac{d^2}{d\vartheta^2} + \frac{\omega^2}{\omega_A^2} (1 + 2\epsilon \cos\vartheta) - \frac{S^2}{(1+S^2\vartheta^2)^2} \right] \phi = 0. \quad (4.28)$$

The factor $2\epsilon \cos\vartheta$ comes from the field line variation of V_A^2 in the inertia term. Note that when $S=0$, Eq. (4.28) assumes the form of the Mathieu equation,

$$\frac{d^2 y}{dv^2} + (a - 2q \cos 2v) y = 0, \quad (4.29)$$

with $a = 4\Omega^2$, $q = -4\Omega^2 \varepsilon$. Solutions of this equation are well known.¹⁰⁷ At each value of q , there exists an infinite number of pairs of characteristic values for a , labeled by $m=1,2,3,\dots$, such that $a \approx m^2$ (for small q); the gap between the members of each pair is of order q^m . In more appropriate terms, the gaps are of width $\sim \varepsilon^m$ about $|\omega/\omega_A| = m/2$. Outside of the gaps, Eq. (4.29) has well-behaved continuum solutions, while inside the gaps, the solutions diverge as $v \rightarrow \infty$. The main result of Cheng, Chen, and Chance¹⁰² is that the contribution of $S^2/(1+S^2 v^2)^2$ to Eq. (4.28) allows a stable toroidal shear Alfvén wave to exist inside the gap. For example, the lowest order (with $\varepsilon \ll 1$) solution lies between

$$\frac{1}{4(1+\varepsilon)} < \Omega^2 < \frac{1}{4(1-\varepsilon)}$$

for even parity solutions with $S \ll 1$, they obtained¹⁰²

$$\frac{\omega}{\omega_A} = \pm \frac{1}{2} \left(1 + \varepsilon \frac{[(1 - S^2 \pi^2/32)^2 - S^2 \pi^2/16]}{[(1 - S^2 \pi^2/32)^2 + S^2 \pi^2/16]} \right)^{-1/2}. \quad (4.30)$$

We will first show analytically that the hot particle resonance can destabilize this mode for arbitrarily small α_h , and then proceed to examine various aspects of these "gap modes" numerically.

Here we consider even modes with $S \ll 1$ and order $\alpha_h \sim S^2$ so that we may do a perturbation analysis on the known result, Eq. (4.30). To lowest order in α_h , we need only solve

$$\begin{aligned} & \left[\frac{d^2}{d\vartheta^2} + \frac{\omega^2}{\omega_A^2} (1 + 2\varepsilon \cos\vartheta) - \frac{S^2}{(1 + S^2 \vartheta^2)^2} \right] \phi \\ &= \frac{(\cos\vartheta + S\vartheta \sin\vartheta)}{(1 + S^2 \vartheta^2)^{1/2}} m_h \int \frac{dE d\mu B}{|v_{\parallel}|} \frac{\omega_*}{\omega - \langle \omega_d \rangle} \mu^2 \frac{\partial F_h}{\partial E} \\ & \ll \phi_q^2 \frac{(\cos\vartheta + S\vartheta \sin\vartheta)}{(1 + S^2 \vartheta^2)^{1/2}} >. \end{aligned} \quad (4.31)$$

Note that we have dropped the fluid-type pressure gradient-curvature term for the hot particles here; it should have little effect on these modes. To further simplify the analysis, we assume that the energetic particles contribute only for $|\vartheta| < \vartheta_0$; that is, only in the first period of ϑ , near the maximum of ϕ .

Cheng, Chen, and Chance employed the method of asymptotic matching to integrate Eq. (4.28). Defining $x = S\vartheta$, the four regions needed are: (i) $x \sim 1$, (ii) $x \sim \varepsilon^{-1/4}$, (iii) $x \sim \varepsilon^{-1/2}$, and (iv) $x \sim \varepsilon^{-1}$.

If we restrict ϑ_0 such that $S(\pi + \vartheta_0) < \varepsilon^{-1/4}$, the trapped particle contribution is important only in region (i). Since $S \ll 1$ and $\varepsilon \ll 1$ are assumed, this condition is easily satisfied. The contribution of the kinetic term to first order in S^2 and, hence, in α_h , must then be calculated. The lowest order solution in S for ϕ ($\propto \cos(\vartheta/2)$) is used in the bounce average appearing in Eq. (4.31), and the value of ω given by Eq. (4.30) is inserted in the resonant denominator. Finally, the total solution in region (i) is joined onto region (ii), etc. to form a dispersion relation. In this manner we obtain

$$\frac{\omega}{\omega_A} = \pm \frac{1}{2} \left\{ 1 + \varepsilon \frac{[(1 - \frac{S^2 \pi^2}{32} - \hat{\alpha}_h S^2)^2 - 9(\frac{\pi S^2}{12} + \hat{\alpha}'_h S^2)^2 / S^2]}{[(1 - \frac{S^2 \pi^2}{32} - \hat{\alpha}_h S^2)^2 + 9(\frac{\pi S^2}{12} + \hat{\alpha}'_h S^2)^2 / S^2]} \right\}^{-1/2}, \quad (4.32)$$

where

$$\hat{\alpha}_h = I \frac{\pi}{2S} \left[\frac{\pi}{2} - \tan^{-1} \pi S - \frac{(\pi + \vartheta_0)S}{1 + (\pi + \vartheta_0)^2 S^2} \right],$$

$$\hat{\alpha}'_h = I \frac{\pi}{3S},$$

$$I = \frac{2\alpha_h}{5\pi\varepsilon^2(1 - \cos\vartheta_0)^{3/2}} \int_1^{B_c/B_{\min}} d\lambda \lambda^{3/2} (\lambda - 1) I_c^2 I_{7/2},$$

$$I_c = \int_0^{\vartheta_T} \frac{d\vartheta \cos(\vartheta/2) (\cos\vartheta + S\vartheta \sin\vartheta)}{\sqrt{\cos\vartheta - \cos\vartheta_T} (1 + S^2\vartheta^2)^{1/2}}$$

and all other quantities are as defined in Sec. 4.2. Note that the terms multiplying I in the expressions for $\hat{\alpha}_h$ and $\hat{\alpha}'_h$ represent the integration of the ϑ dependence of the kinetic integral.

If we assume $\text{Im } \omega \ll \text{Re } \omega \approx -\omega_A/2$ and $\text{Re } \omega \cdot \omega_d > 0$, we can show that $S^2 \hat{\alpha}_h \equiv \hat{\alpha}_{hr} - i \hat{\alpha}_{hi}$ and $S^2 \hat{\alpha}'_h \equiv \hat{\alpha}'_{hr} - i \hat{\alpha}'_{hi}$, where $\hat{\alpha}_{hr}$, $\hat{\alpha}'_{hr}$, $\hat{\alpha}_{hi}$, $\hat{\alpha}'_{hi}$ are all positive. Then, we have approximately

$$\frac{\omega}{\omega_A} \approx - \left| \frac{\omega_0}{\omega_A} \right| \left(1 - 2i\varepsilon \frac{\omega_0^2}{\omega_A^2} \frac{[3\pi \hat{\alpha}'_{hi} (1 - \frac{\pi^2 S^2}{32})^2 + \hat{\alpha}_{hi} \frac{\pi^2 S^2}{4}]}{[(1 - \frac{\pi^2 S^2}{32})^2 + \frac{\pi^2 S^2}{16}]^2} \right), \quad (4.33)$$

where ω_0/ω_A is given by Eq. (4.30). For $\alpha_h \neq 0$, we have $\text{Im } \omega/\omega_A > 0$; that is, instability for arbitrarily small α_h .

By including the $2\varepsilon \cos\vartheta$ modulation of the inertia term, these results can be demonstrated numerically and then extended to regimes in which the analytic expressions are inappropriate. A couple of values of α_h and S were used to compare ω as obtained from Eq. (4.32) with that found by using the shooting code; in all cases the outcome was favorable. Figs. 4.7 and 4.8 show the effects of first raising α_h from zero at $\alpha_c=0$ [curve (i)], and then allowing α_c to be nonzero at $\alpha_h \approx 2.0$ [curve (ii)]. For these two

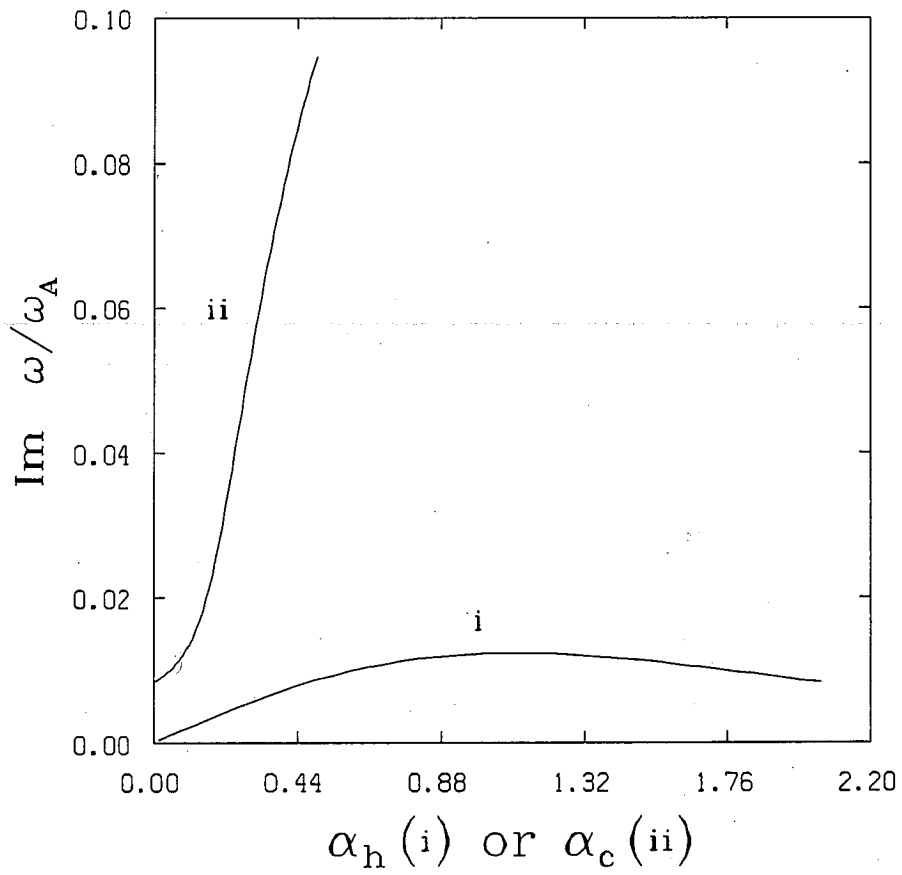


Fig. 4.7. Imaginary part of the eigenvalue for the gap mode near $\omega/\omega_A=0.5$ as α_h [curve (i), $\alpha_c=0$], and α_c [curve (ii), $\alpha_h=2$.] are varied.

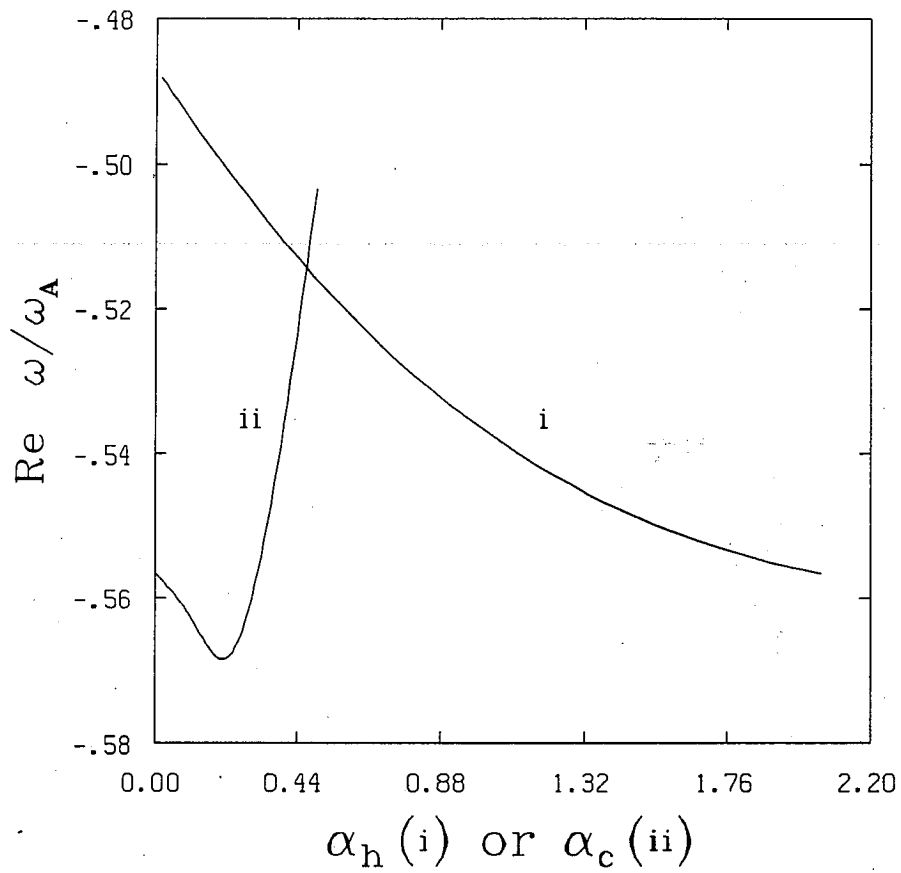


Fig. 4.8. Real part of the eigenvalue for the gap mode near $\omega/\omega_A=0.5$ as α_h [curve (i), $\alpha_c=0$], and α_c [curve (ii), $\alpha_h=2$.] are varied.

runs, $\omega_{d0}/\omega_A = 0.5$, $S = 0.5$, $\varepsilon = 0.2$, $\nu_0 = 0.785$, and $q = 2.0$. Note that at the initial point of the first curve ($\alpha_c = \alpha_h = 0$), $\omega/\omega_A \approx -0.49$, in reasonable agreement with Eq. (4.30). As α_h increases, $\text{Im } \omega/\omega_A$ first rises linearly in accord with Eq. (4.33) and then reaches a maximum near $\text{Im } \omega/\omega_A \approx 0.01$. The growth rates predicted here are considerably smaller than those discussed in Sec. 4.3.a. For small α_c , this remains true, but when $\alpha_c > 0.2$, $\text{Im } \omega/\omega_A$ begins to increase rapidly. Note that the real part (Fig. 4.8) appears to alter its behavior at this same point, heading outside of the gap,

$$\frac{1}{4(1+\varepsilon)} < \frac{\omega^2}{\omega_A^2} < \frac{1}{4(1-\varepsilon)}$$

If curve (ii) is followed up to $\alpha_c = 0.8$, and the other parameters are altered appropriately, one obtains the high frequency precessional mode, $\omega \ll \omega_d$, as in Figs. 4.1 and 4.2. Thus, at significant α_c and α_h , the fundamental gap mode "becomes" the drift resonant precessional mode; the switch in character appears to occur around $\alpha_c = 0.2$ for this particular set of parameters.

Although the gap mode near $|\omega/\omega_A| = 0.5$ may not be clearly identifiable in those regions of parameter space where both the MHD and precessional branches of solutions to Eqs. (4.17a) and (4.17b) are stable, the higher order gap modes, $|\omega/\omega_A| = 1.0, 1.5,$

2.0, ..., may remain and can be unstable. In order to systematically search for these modes and to identify any other instabilities described by this system of equations, we employ a Nyquist technique (see, for example, Ref. 115). That is, we plot the dispersion relation, $g(\omega) = d(\ln\phi)/d\psi(\psi=0)$, in the complex g plane as ω is varied according to the path shown in Fig. 4.9. The number of unstable roots is equal to the number of times the origin of the g plane is encircled in a counter-clockwise sense.

This basic approach must be modified somewhat due to the complicated nature of the problem; in particular, the presence of the gap modes introduces a great deal of structure into the diagram. First, only frequencies in the range $\text{Re}|\omega| \lesssim 3\omega_A$ will be examined; thus, we should be able to see modes with $\omega \ll \omega_d$, $\omega \lesssim \omega_d$ and several gap modes. Since ω_d has a definite sign ($\omega_d < 0$), and we expect resonant instability only when $\text{Re} \omega \cdot \omega_d > 0$, we can further narrow the range of interest to $\text{Re} \omega \leq 0$. Second, $\text{Im} \omega$ is generally required to be positive in order that the boundary conditions, $\text{Im} k > 0$ and $\text{Re} \partial\omega/\partial k > 0$, can both be satisfied (Sec. 4.2).

As an example, we show in Fig. 4.10 the path traced out in the $g(\omega)$ plane as $\text{Re} \omega$ is varied from $\sim -3\omega_A$ to $+\omega_A$ with $\text{Im} \omega/\omega_A = 10^{-4}$, $\alpha_h = 0.86$, and $\Delta_r/r = 0.2$; all other parameters are as in Fig. 4.3. The large scale view given in Fig. 4.10a shows the complicated structure introduced by the gap modes. The two lines extending outside the figure in the lower half plane connect at

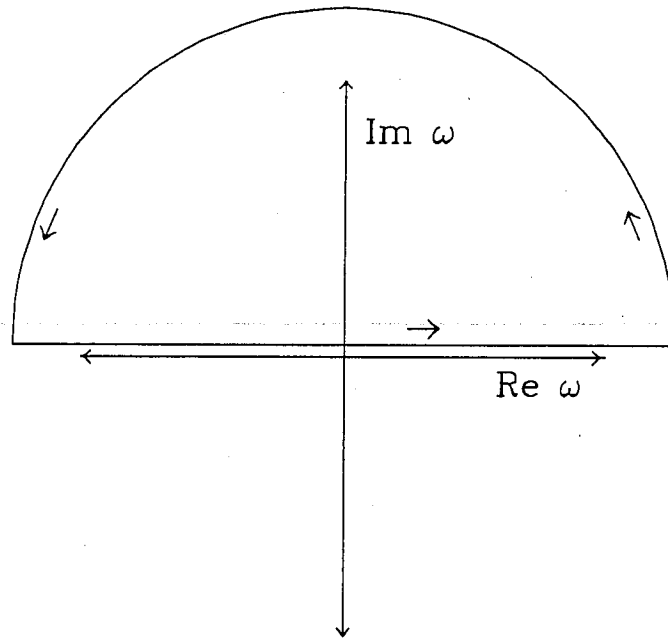


Fig. 4.9. Generic trajectory in the complex ω plane used to generate a Nyquist diagram.

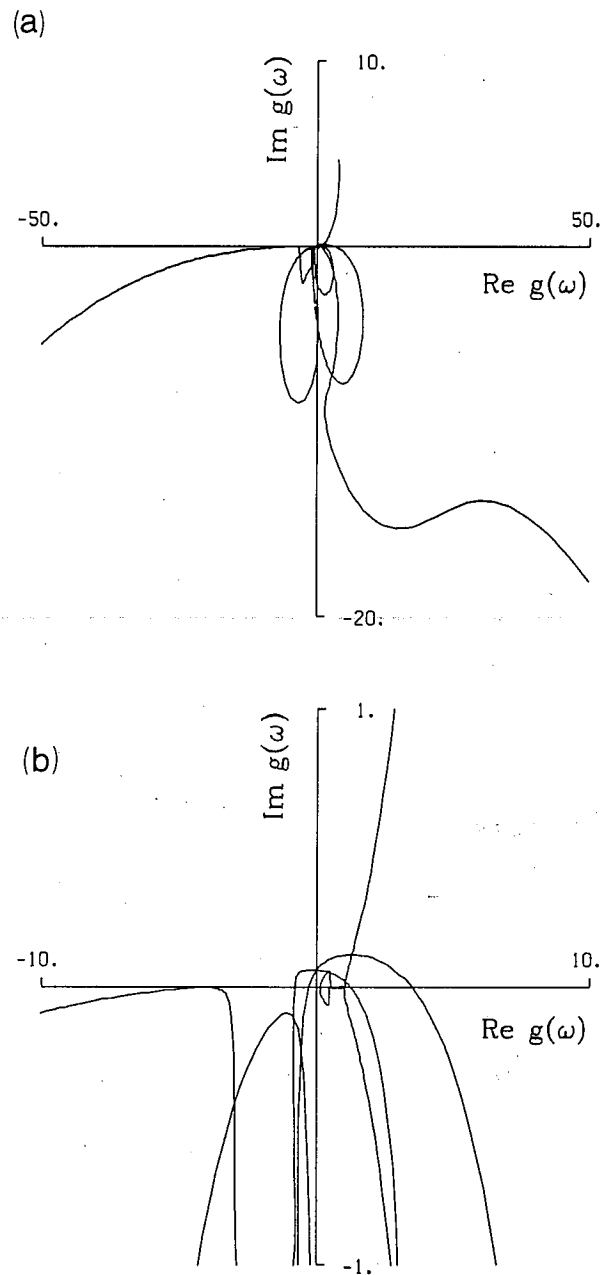


Fig. 4.10. Path traced out in the complex g plane (a) as $\text{Re } \omega$ is varied from $-3\omega_A$ to ω_A with $\text{Im } \omega/\omega_A = 10^{-4}$ and $\alpha_n = 0.86$. (b) is a close-up of the region near the origin shown in (a).

larger $|g(\omega)|$. The beginning of the path ($\omega \approx -3\omega_A$) cannot be clearly identified in this plot; it ends ($\omega \approx +\omega_A$) at a point in the first quadrant of Fig. 4.10a. A close-up of the region near the origin is shown in Fig. 4.10b. The unconnected lines at the edge of the plot represent the endpoints of the larger scale structures of Fig. 4.10a. We see two unstable gap roots here; their presence is indicated by the loops crossing the positive imaginary axis, denoting counter-clockwise encirclements of the origin. The value of $\text{Re } \omega$ at the point nearest $g=0$ provides a good guess for the eigenfrequency of the instability; further numerical calculations give actual roots to the dispersion relation: $\omega/\omega_A = -1.52 + 8.3 \times 10^{-4}i$ and $\omega/\omega_A = -2.53 + 1.4 \times 10^{-4}i$. The small crescent-shaped loop near the origin on the positive real axis in Fig. 4.10b represents the low frequency MHD instability. This loop is traversed in a clockwise sense as ω goes from just below to just above zero. When the ballooning root is stabilized (e.g., by raising α_h) this loop "moves" to the left and encircles the origin so that the path as a whole has executed one fewer counter-clockwise trips around $g=0$. In this case, the frequency of the eigenmode is $\omega/\omega_A = -.01 + .27i$.

This procedure was carried out for several different sets of parameters, both inside and outside of the stability window (Sec. 4.3.b). One or more unstable gap modes was found for each set. All told, roots near $\text{Re } \omega/\omega_A = -1.0, -1.5, -2.0,$ and -2.5

were seen, with the one at $\text{Re } \omega/\omega_A \cong -1.5$ producing the largest growth rate in general. As mentioned above, the gap mode near $\omega/\omega_A = -0.5$ at $\alpha_c = \alpha_h = 0$ is indistinguishable from the drift resonant precessional mode when α_c and α_h are of order unity. One run was made with $\omega_{*0}/\omega_{d0} \neq 0$; again, an unstable root not belonging to the MHD or precessional branches was found. The physical basis for this mode is not clear; it could conceivably be related to the gap modes.

The unstable gap modes usually have relatively small growth rates, $\text{Im } \omega/\omega_A \sim 10^{-3} - 10^{-4}$. As with the precessional mode, $\text{Im } \omega$ increases as α_h is made larger or as ω_{d0}/ω_A is lowered. Consequently, it is found that growth rates up to $\gamma_{\text{MHD}}/10$ can be found in relevant regions of parameter space, including cases where $\omega_{*0}/\omega_{d0} \neq 0$. Finally, these instabilities persist in many instances even if the $2\epsilon \cos\vartheta$ term is removed, although $\text{Im } \omega$ is reduced somewhat in the process. The modes remain because the ϑ dependences introduced by the various α_c and α_h terms in Eqs. (4.17a) and (4.17b) can provide the modulation necessary to couple neighboring poloidal harmonics.¹⁰³

4.3.d Conclusions

To conclude this section on deeply trapped particles, we again consider a marginal stability plot. Now, however, we include a third curve representing the $\omega/\omega_A \cong -1.5$ gap mode. Fig. 4.11

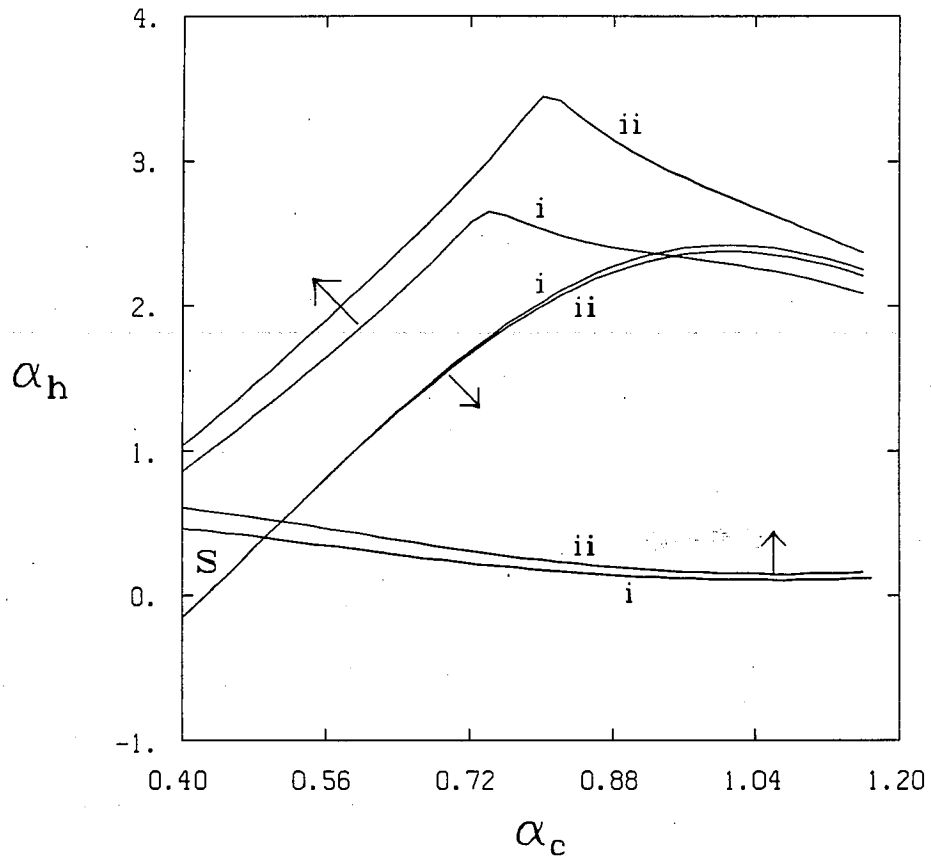


Fig. 4.11. Marginally stable ($\text{Im } \omega/\omega_A = 10^{-3}$) values of α_h for the high-frequency, precessional (uppermost pair), low-frequency, MHD (center pair), and $\text{Re } \omega/\omega_A \approx -1.5$ gap (lowest pair) modes as α_c is varied. Curves labelled (i) are for $\omega_{d0}/\omega_A = 0.848$; (ii) indicates $\omega_{d0}/\omega_A = 1.06$.

shows the boundaries in the $\alpha_h - \alpha_c$ plane for two values of ω_{d0}/ω_A , (i) $\omega_{d0}/\omega_A = 0.848$, and (ii) $\omega_{d0}/\omega_A = 1.06$; all other parameters are as in Sec. 4.3.b. $\text{Im } \omega$ changes rapidly with α_h near marginal stability (Fig. 4.3) for the MHD and precessional branches; hence, their true marginal stability contours are very close to the ones shown in Fig. 4.11 for $\text{Im } \omega/\omega_A = 10^{-3}$. On the other hand, the gap mode is unstable for all $\alpha_h > 0$; choosing to draw a line where $\text{Im } \omega/\omega_A = 10^{-3}$ for this instability is somewhat arbitrary. The region labelled S indicates an area in which $\text{Im } \omega/\omega_A < 10^{-3}$ for all three instabilities if $\omega_{d0}/\omega_A = 0.848$.

The uppermost pair of curves represents the stability boundaries for the high-frequency precessional branch. The arrow indicates the direction of increasing growth rate. As one would expect from previous discussions, the arrow points toward a region of larger α_h . We note a significant space between these two curves, especially at large α_c . This is just the effect predicted by the stability boundary for this mode shown in Fig. 4.4. Fig. 4.4 also emphasized the fact that changing ω_{d0}/ω_A has little effect on the stability boundary of the low-frequency, MHD branch, at least for $\omega_{d0}/\omega_A > 0.6$. The middle pair of curves demonstrates this feature once more; they represent the stability boundary for the low-frequency mode at (i) $\omega_{d0}/\omega_A = 0.848$ and (ii) $\omega_{d0}/\omega_A = 1.06$. The arrow here indicates increased growth rates for larger α_c , as we would expect since the MHD growth rate goes approximately like

$\sqrt{\alpha_c}$. Now, we note the stable band between this pair of curves and the marginal stability boundaries for the high-frequency branch. We have already examined how its width in α_h varies with ω_{d0}/ω_A , Δ_r/r , and ω_{*0}/ω_{d0} in Figs. 4.4 - 4.6. Note that it does not close off in case (ii) as the critical α_h for the low-frequency branch peaks and begins to decrease for $\alpha_c \gtrsim 1.1$. Presumably, this remains the case as second stability ($\alpha_c \cong 1.9$ for $S=0.6$) is approached, and the critical α_h goes to zero.

The third pair of curves represents the points at which $\text{Im } \omega/\omega_A = 10^{-3}$ for the $\omega/\omega_A \cong -1.5$ gap mode. The arrow indicates an increased growth rate for larger α_h (this increases the magnitude of the destabilizing kinetic term) so that most of the area plotted here would be unstable, except for the region labelled S. However, as noted in Sec. 4.3.c, the growth rates for this mode remain small compared to γ_{MHD} .

If we can ignore the gap mode, the possibilities for at least extending the first stability boundary to larger α_c seem promising. Although the path to second stability closes off for $\omega_{d0}/\omega_A \lesssim 1$ for this set of parameters, the stability window at small α_c remains relatively wide as ω_{d0}/ω_A is decreased. To get $\omega_{d0}/\omega_A \gtrsim 1$ for all mode numbers reasonably treated by the high-mode-number limit, particle energies of order 1 MeV are necessary. Unfortunately, such a high temperature species would be hard to create with present technology. It must also be pointed

out that these particles would no longer be needed once second stability is reached.

Certainly, the nonlinear behavior of each of these instabilities is very important in evaluating the utility of any operating regime. In particular, if the gap modes saturate at a tolerably low level and do not produce significant diffusion, it may only be necessary to arrange to be in the stability window in order to avoid high-mode-number instabilities in tokamaks with significant core pressure gradients. Further work should be done on low mode number instabilities, as well as including more detailed effects in the present system, such as full finite Larmor radius effects, banana width effects, and parallel pressure for the energetic particles.

4.4 Sloshing Particles

Most of the negative aspects of deeply trapped energetic particles in a tokamak are associated with the drift resonances in the kinetic term, Eq. (4.2b). To this point, we have considered average precessional drift frequencies of only one sign, $\omega_* \langle \omega_d \rangle > 0$. By introducing a distribution in which most of the particles are almost marginally trapped, with turning points in the good curvature region of the tokamak, it may be possible to arrange

$\omega_* \langle \omega_d \rangle < 0$, at least when averaged over the distribution, and thereby remove the resonant destabilization.³⁹

In this section, we examine the prospects for using a "sloshing ion"¹¹⁶ trapped particle distribution to stabilize the MHD ballooning mode and, hopefully, to avoid the unstable precessional mode, or at least lower the requirements on the energetic particle temperature necessary to stabilize it. We will use the same equations as in Sec. 4.2, but will modify the form of $F_h(\mu, E, \psi)$ according to our needs. From a theoretical point of view, this is all one needs to consider; however, this type of distribution requires more energy as it fills a larger volume and thus may be much more difficult to create and maintain than one with deeply trapped ions. Sloshing ions might be introduced by neutral beam injection with $v_{\parallel}/v_{\perp} \approx (2\varepsilon)^{1/2}$ on the outside of the tokamak so that the injected particles have turning points near the inside edge. Another approach might be to use cyclotron resonance heating, but with the resonances located in the good curvature region. Pitch angle scattering may cause the distribution to be rapidly depleted; if the sloshing ions are found to have favorable stability properties, questions such as this must then be addressed.

Due to the greater parallel velocities arising here than in the deeply trapped case, parallel pressure and banana width effects become more important. The former can be shown to be a factor of

r/R_0 smaller than the perpendicular pressure for the distribution we will use; again, this follows from the fact that the particles are trapped in a shallow mirror. Banana width effects will be ignored for simplicity, but deserve further study.

4.4.a Equilibrium Modifications

The distribution function we will use is similar to Eq. (4.16); an additional factor has been introduced to allow it to be peaked near $\mu = \epsilon/B_c$ (i.e., turning point is ψ_0). Namely,

$$F_h[\mu, E, \psi(r)] = \begin{cases} \alpha_F \left[1 - \frac{(r-r_0)^2}{\Delta_r^2} \right] \frac{(\mu B_c - E)e^{-E/T}}{\left[1 + \frac{(\mu B_c/E - 1)^2}{\Delta\lambda^2} \right]} & \frac{E}{B_c} < \mu < \frac{E}{B_{\min}} \\ 0 & 0 < \mu < \frac{E}{B_c} \end{cases} \quad (4.34)$$

where

$$\alpha_F = \frac{16 B_c^{3/2} \hat{p}_{lh}}{15\sqrt{\pi} m_h T^{7/2} C(0)}$$

$$C(\vartheta) \equiv B^{3/2} \int_1^{B_c/B} \frac{d\lambda \lambda}{\sqrt{B_c/B - \lambda}} \frac{(\lambda - 1)}{\left[1 + \frac{(\lambda - 1)^2}{\Delta\lambda^2}\right]}$$

Thus,

$$P_{\perp h}(\vartheta) = \hat{P}_{\perp h} \left[1 - \frac{(r-r_0)^2}{\Delta_r^2}\right] \frac{C(\vartheta)}{C(0)} = \hat{P}_{\perp h} \left[1 - \frac{(r-r_0)^2}{\Delta_r^2}\right] p_{\perp}(\vartheta),$$

as before. All other quantities are as defined in Sec. 4.2. Now, however, $p_{\perp}(\vartheta)$ and $p_{\parallel}(\vartheta)$ cannot be calculated analytically. Instead, they are computed numerically on a grid at the beginning of the program, and values at arbitrary ϑ are obtained by interpolation. Code testing is simplified by the fact that the deeply trapped results of Sec. 4.3 can be reproduced exactly in the limit $\Delta\lambda \rightarrow \infty$.

We first examine how varying $\Delta\lambda$ affects $p_{\perp}(\vartheta)$. Fig. 4.12 shows $p_{\perp}(\vartheta)$ for (i) $\Delta\lambda = 10.$, (ii) $\Delta\lambda = 0.1$, (iii) $\Delta\lambda = 0.05$, and (iv) $\Delta\lambda = 0.02$ when $\vartheta_0 = 3.04$ and $\varepsilon = 0.2$. Note the shift in the peak of $p_{\perp}(\vartheta)$ from $\vartheta = 0$ to $\vartheta > \pi/2$ (into the good curvature region), and the increase in $|dp_{\perp}/d\vartheta|$ near ϑ_0 as $\Delta\lambda$ is lowered. An important consequence of this fact is that $\tau = 1 + (1/B)\partial P_{\perp h}/\partial B$ could become negative if $\Delta\lambda$ is too small. It is well known that if $\tau < 0$, the plasma will be mirror-mode unstable.^{45,68} In addition, problems,

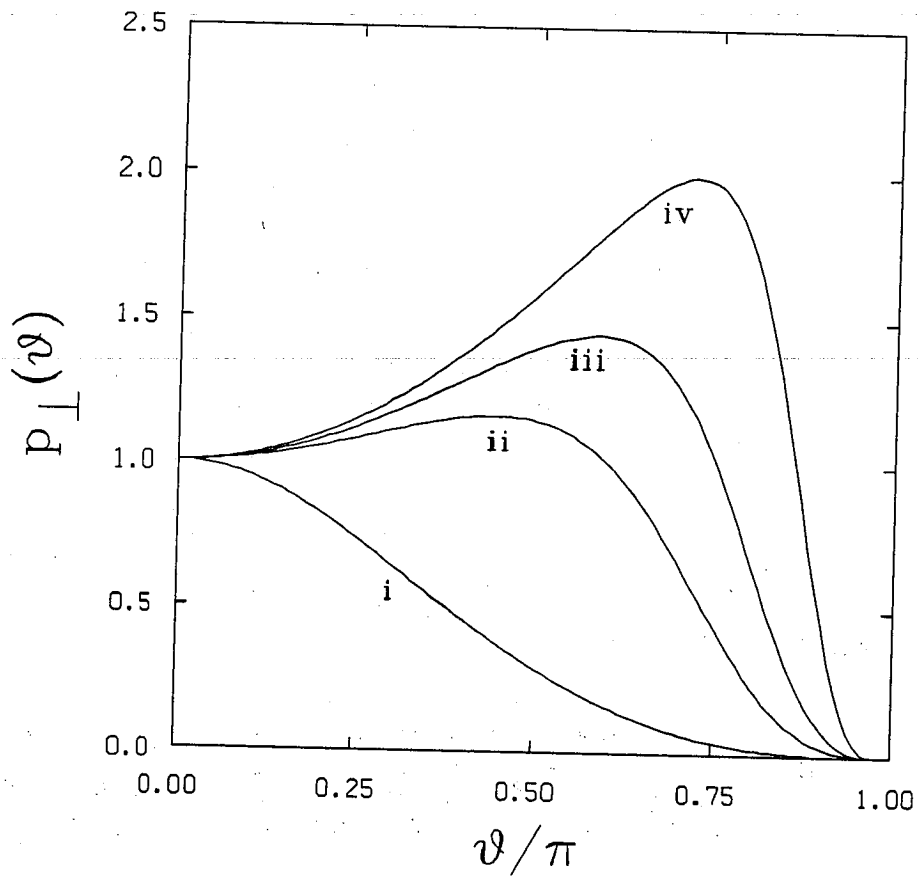


Fig. 4.12. Variation of the perpendicular pressure function $p_{\perp}(\vartheta)$ with ϑ for the distribution given by Eq. (4.34). Curves appear for (i) $\Delta\lambda=10.$, (ii) $\Delta\lambda=0.1$, (iii) $\Delta\lambda=0.05$, and (iv) $\Delta\lambda=0.02$.

both analytical and numerical, with calculating an equilibrium arise in this case. Of course, the size of $(1/B)\partial P_{\perp h}/\partial B$ depends also on $\hat{P}_{\perp h}$; recall that in terms of the input parameters, $\hat{P}_{\perp h} \propto \alpha_h \Delta_r / r$. In other words, if we set $\Delta_r / r = 0$, the calculation will proceed smoothly since $\tau = 1$, although the result may be physically unrealistic if $|\partial p_{\perp} / \partial \vartheta| \gg 1$.

Analytic estimates can be made for the restrictions on $\Delta\lambda$, α_h and Δ_r / r necessary to keep $\tau > 0$. First, consider $\Delta_r / r = 0.2$; should a smaller value be realistic, these results can be modified by the appropriate factor. Second, it can be shown that

$$\frac{1}{B} \frac{\partial P_{\perp h}}{\partial B} \Big|_{\text{maximum}} \approx \frac{-0.06}{\Delta\lambda^{3/2}} \frac{\alpha_h}{q^2} \frac{\Delta_r}{r} \frac{r}{R_0} \quad (4.35)$$

If we take $\alpha_h = 1.5$, a reasonable value considering previous runs, $\Delta\lambda = 0.02$, the largest $\Delta\lambda$ for which p_{\perp} shows a significant peak away from $\vartheta = 0$, $q = 2$, and $r/R_0 = 0.2$, we find $\frac{1}{B} \frac{\partial P_{\perp h}}{\partial B} \Big|_{\text{maximum}} \approx -0.33$. For this same value of $\hat{P}_{\perp h}$, $\frac{1}{B} \frac{\partial P_{\perp h}}{\partial B} \Big|_{\text{maximum}} = -1$ at $\Delta\lambda \approx 0.01$! Thus, even with moderate α_h and Δ_r / r , τ will go through zero if $\Delta\lambda < 0.01$.

These restrictions can be alleviated by including circulating as well as trapped energetic particles. In this manner $P_{\perp h}$ does not vanish anywhere along the field line. Thus, the pressure can be highly peaked in the good curvature region without

incurring large negative values of $\frac{1}{B} \frac{\partial P_{1h}}{\partial B}$. This approach is more realistic than the previous one if we consider the circulating, or passing, component to consist of trapped particles that have undergone pitch angle scattering.

When the passing particles have a high transit frequency (analogous to the bounce frequency for trapped particles), the alterations to Eqs. (4.17a) and (4.17b) are few since the passing particles do not contribute to the kinetic term in Eq. (4.17b).¹¹⁷ They do, however, enter the calculation through the fluid pressure gradient term in Eq. (4.17a) as well as appear in the various equilibrium quantities involving the energetic species pressure.

The distribution we now consider is

$$F_h[E, \mu, \psi] = \alpha_F \left[1 - \frac{(r-r_0)^2}{\Delta r^2} \right] \frac{E e^{-E/T}}{\left[1 + \frac{(\mu B_c/E-1)^2}{\Delta \lambda^2} \right]}, \quad (4.36)$$

where in this case

$$C(\vartheta) = B^{3/2} \int_0^{B_c/B} \frac{d\lambda \lambda}{\sqrt{B_c/B - \lambda}} \frac{1}{\left[1 + \frac{(\lambda - 1)^2}{\Delta \lambda^2} \right]},$$

and $\vartheta_0 \equiv \pi$. The normalization factor α_F remains as before,

$$\alpha_F = \frac{16 B_c^{3/2} \hat{P}_{\perp h}}{15\sqrt{\pi} m_h T^{7/2} C(0)}$$

Despite the change in the limits of the integral defining $C(\vartheta)$, the magnetic moment integral in Eq. (4.17b) still only ranges from E/B_c to E/B , including only the trapped particles.

For convenience, we have chosen the peak of the pitch angle distribution to be at $\lambda=1$; it turns out that $\frac{1}{B} \frac{\partial P_{\perp h}}{\partial B} < 0$ near $\vartheta=\pi$ in this case. However, by shifting the peak to a slightly smaller value, say $\lambda \cong 1 - \Delta\lambda$ (increase the fraction of passing particles), this effect may be removed completely so that $\frac{1}{B} \frac{\partial P_{\perp h}}{\partial B} > 0$ all along the field line. In other words, the problems with τ vanishing can be eliminated by altering the details of the distribution, whereas the sharp drop in $P_{\perp h}(B)$ is a fundamental feature of the purely-trapped distribution, Eq. (4.34)

With $\Delta\lambda=0.02$ and $r/R_0=0.2$, the trapped particle distribution in Eq. (4.34) yields a maximum value of $p_{\perp}(\vartheta)|_{\max} \cong 2$ (Fig. 4.12), while Eq. (4.36) with the same parameters produces $p_{\perp}(\vartheta)|_{\max} \cong 7$. Even so, due to the presence of the passing component, τ remains positive for typical values of α_h and Δ_r/r . The distribution in Eq. (4.36) allows us to achieve a considerable level of anisotropy and, hence, place the turning points of most of

the trapped particles near $\vartheta=\pi$ (i.e., $\mu=E/B_{\min}$) without having to be concerned about whether or not τ vanishes. Consequently, we can increase the contribution of particles with $\omega_*\langle\omega_d\rangle < 0$ to the kinetic integral in Eq. (4.17b) relative to what can be done using a distribution that contains only trapped particles.

4.4.b Eigenmode Calculations

We will consider the change from deeply trapped to sloshing particles in two steps. First, we increase ϑ_0 up to near π with $\Delta\lambda \gg 1$, and then, with ϑ_0 fixed, decrease $\Delta\lambda$. Other parameters will remain as before. The objective here is to demonstrate an improved stability picture relative to that described in Sec. 4.3. Hence, we set $\omega_{d0}/\omega_A = 0.636$, at which point the stability window in α_h is closed. If the sloshing ions cannot alleviate the unstable precessional mode in this case, it may be more reasonable to return to the deeply trapped case and seek experimental methods for increasing the realistic values of ω_{d0}/ω_A . Fig. 4.13 shows $\text{Im } \omega/\omega_A$ as a function of α_h for (i) $\vartheta_0 = 0.785$, (ii) $\vartheta_0 = 1.57$, (iii) $\vartheta_0 = 2.355$, and (iv) $\vartheta_0 = 3.04$. Increasing ϑ_0 apparently allows the MHD root to be stabilized at a faster rate; this is probably just due to the larger number of energetic particles in the system at higher values of ϑ_0 .

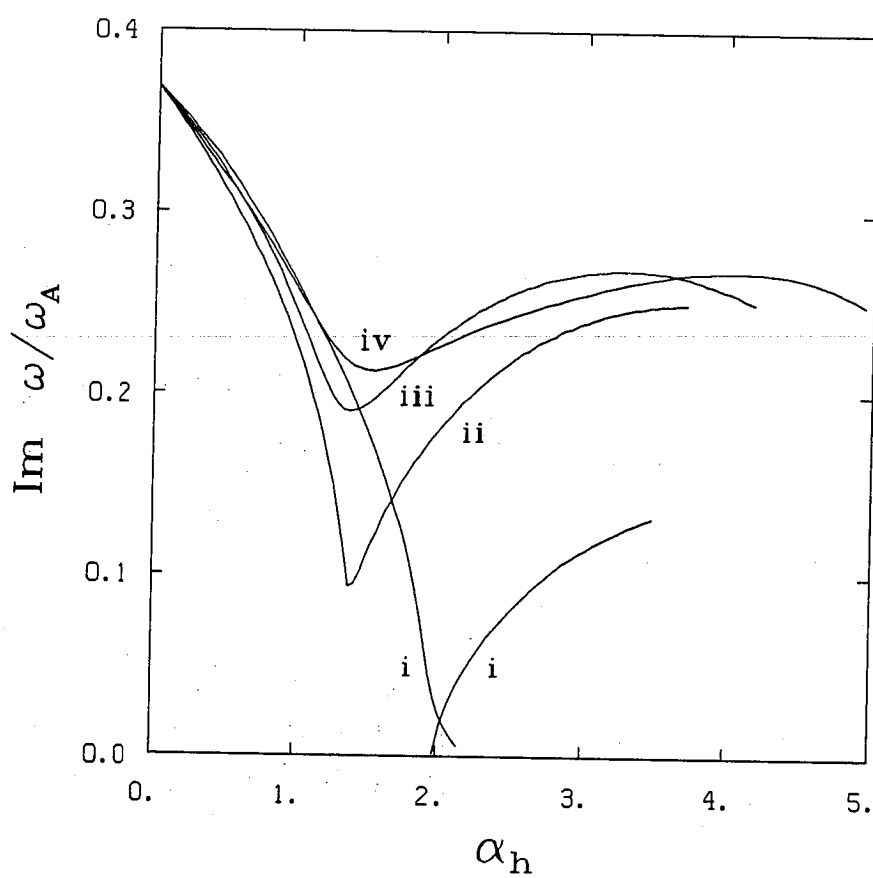


Fig. 4.13. Plot of the imaginary part of the eigenvalue as a function of α_h with $\Delta\lambda=10^6$. Curves appear for (i) $\vartheta_0=0.785$, (ii) $\vartheta_0=1.57$, (iii) $\vartheta_0=2.355$, and (iv) $\vartheta_0=3.04$.

The most startling feature of Fig. 4.13 is the rapid rise of $\text{Im } \omega/\omega_A$ with ϑ_0 for larger pressure gradients. The fact that each of the curves for $\vartheta_0 \geq 1.57$ goes through a minimum indicates that the instability on the right-hand side of the plot is the high frequency, precessional branch. Recall from the results of Sec. 4.3 that it is very sensitive to the value of $\langle \omega_d \rangle$. In particular, we note that the changes in the curves brought about by increasing ϑ_0 are reminiscent of what took place in Fig. 4.1 as ω_{d0}/ω_A was lowered. We may then suspect that it is the alteration of $\langle \omega_d \rangle$ with ϑ_0 that is responsible for the increased destabilization.

To understand this behavior, we need to examine $\langle \omega_d \rangle$ in more detail. Recall that,

$$\langle \omega_d \rangle \approx - \frac{\mu B}{\Omega_h} \langle \hat{e} \cdot \nabla B \rangle, \quad (4.37)$$

ignoring the v_{\parallel} contribution. Then, using the equilibrium relations derived in Sec. 4.3 (set $\sigma=\tau=1$ here for simplicity),

$$\begin{aligned} \frac{\langle \omega_d \rangle}{\omega_{d0}} = & -\lambda z \left(\langle \cos \vartheta \rangle + S \langle \vartheta \sin \vartheta \rangle - \alpha_c \left(\langle \sin^2 \vartheta \rangle + \frac{1}{2q^2} \right) \right. \\ & \left. - \alpha_h \left[\langle \sin \vartheta \cdot g(\vartheta) \rangle + \frac{1}{2q^2} \langle p_{\perp}(\vartheta) \rangle \right] \right). \end{aligned} \quad (4.38)$$

This expression can also be written in terms of the quantities defined by Eq. (4.21):

$$\frac{\langle \omega_d \rangle}{\omega_{d0}} = -\lambda z \frac{f(\lambda)}{I_1(\lambda)}. \quad (4.39)$$

Recall that λ and z represent the normalized velocity variables, $z=E/T$ and $\lambda=\mu B_c/E$. The range of λ , the pitch angle, is directly related to ϑ_0 ; namely, $1 \leq \lambda \leq B_c/B_{\min} = B(\vartheta_0)/B(0)$.

The primary contribution to $\langle \omega_d \rangle$ is $\langle \cos \vartheta \rangle$; it is a monotonically decreasing function of ϑ_T , the turning point of the bounce orbit, and changes sign for $\vartheta_T > \pi/2$ (the value of the function at ϑ_T is heavily weighted in the bounce average since $v_{\parallel}=0$ at that point). The geodesic curvature term, $S \langle \vartheta \sin \vartheta \rangle$, is initially zero and increases with ϑ_T up to near π , where $\sin \vartheta \ll 1/\vartheta$. So, in the good curvature region these two terms compete with one another and, in fact, with $\alpha_c = \alpha_h = 0$ and $S=0.6$, the geodesic curvature is large enough to completely offset any change in sign of the normal curvature, at least up to $\vartheta_T=3.04$. However, the diamagnetic effect of α_c is sufficient to change the sign of $\langle \omega_d \rangle$ for $\vartheta_T > 2.75$ ($\alpha_c=0.8$). These results can be demonstrated directly by expressing the first three averages on the right-hand side of Eq. (4.38) in terms of elliptic integrals, as done for the quantities appearing in Eq. (4.21).

Due to the fact that $P_{\perp h}$ varies along the field line while P_c is assumed to be constant, the contribution made by α_h to $\langle \omega_d \rangle$ is more complicated; in particular, it depends on ϑ_0 . Fig. 4.14 demonstrates this clearly; curves for (i) $\vartheta_0=0.785$, (ii) $\vartheta_0=1.57$, (iii) $\vartheta_0=2.355$, and (iv) $\vartheta_0=3.04$ for $\Delta\lambda \gg 1$, as well as one for (v) $\vartheta_0=3.04$, $\Delta\lambda=0.02$, are included. The quantity plotted is

$$\alpha_{h,crit} \equiv \left[\frac{-\langle \omega_d \rangle}{z\omega_{d0}} \right]_{\alpha_h=0} \left\{ \lambda [\langle \sin\vartheta g(\vartheta) \rangle + \frac{1}{2q^2} \langle p_{\perp}(\vartheta) \rangle] \right\}^{-1}; \quad (4.40)$$

that is, the vacuum plus core pressure portions of $\langle \omega_d \rangle$ divided by the trapped particle contribution made if $\alpha_h=1$. Note that this is also the value of α_h needed, for a given ϑ_T , to balance the numerator and denominator of Eq. (4.40) and force the total $\langle \omega_d \rangle$ to vanish.

The relationships between the $\Delta\lambda \gg 1$ curves in Fig. 4.14 are not unlike those on the right-hand side of Fig. 4.13. Indeed, it is this change in the character of $\langle \omega_d \rangle$, as a function of $\vartheta_T(\lambda)$, with ϑ_0 that has brought about the increased destabilization noted in Fig. 4.13. At small ϑ_0 , $\langle \sin\vartheta g(\vartheta) \rangle \ll \langle p_{\perp}(\vartheta) \rangle$. Since the latter is a monotonically decreasing function of ϑ_T at a given ϑ_0 (for $\Delta\lambda \gg 1$), $\alpha_{h,crit}$ rises with ϑ_T , as in the $\vartheta_0 = 0.785$ curve of Fig. 4.14. On the other hand, $\sin\vartheta$ and $g(\vartheta)$ increase from zero at $\vartheta=0$ to a maximum near $\vartheta=\pi/2$. At larger ϑ_0 , their contributions

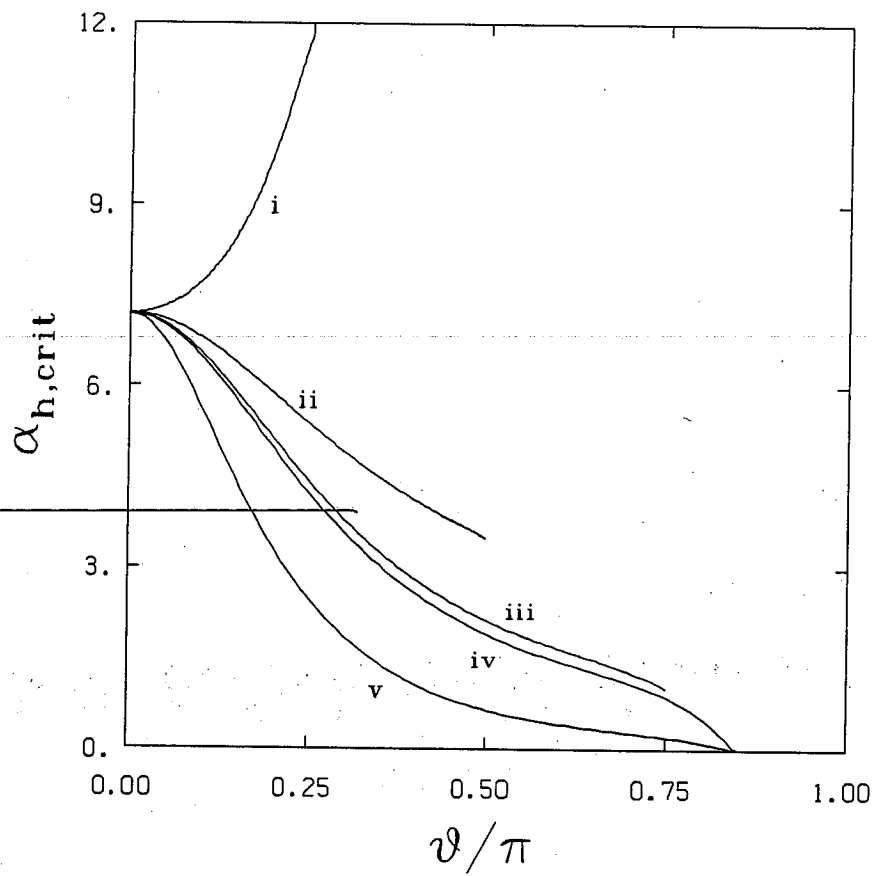


Fig. 4.14. The value of α_h needed to get $\langle \omega_d \rangle = 0$ plotted as a function of the turning point of the bounce average ϑ_T . Four curves represent the results of using $\Delta\lambda = 10^6$: (i) $\vartheta_0 = 0.785$, (ii) $\vartheta_0 = 1.57$, (iii) $\vartheta_0 = 2.355$, and (iv) $\vartheta_0 = 3.04$. The curve labelled (v) is for $\Delta\lambda = 0.02$ and $\vartheta_0 = 3.04$.

increase and can even become dominant, so that $\alpha_{h,crit}$ becomes a decreasing function of ϑ_T , as noted for $\vartheta_0 \geq 1.57$ in Fig. 4.14. For a given value of α_h , $\langle \omega_d \rangle$ is smaller overall for $\vartheta_0 \geq 1.57$ than it is at, say, $\vartheta_0 = 0.785$, but has not completely changed sign. This makes it appear as though ω_{d0}/ω_A was lowered; therefore we expect larger growth rates for this high frequency instability that is a mix of the MHD and precessional modes.

One final feature to note in Fig. 4.14 is that lowering $\Delta\lambda$ to 0.02 will have little effect on $\langle \omega_d \rangle$ [curve (v)]. Rather, the idea in peaking the distribution function near $\lambda=1$ is to switch the emphasis of the pitch angle integral of Eq. (4.20c) from small turning points to larger ones, near π , where $\langle \omega_d \rangle$ has actually changed sign from its value in vacuum. If $\Delta\lambda$ is small enough, the majority of the energetic trapped particles will have $\omega_* \langle \omega_d \rangle < 0$, and the resonant destabilization will hopefully be removed.

The next step is to examine $\text{Im } \omega/\omega_A$ as a function of α_h for $\Delta\lambda=0.02$, $\vartheta_0=3.04$. In Fig. 4.15, four curves appear: (i) $\omega_{*0}/\omega_{d0}=0$, (ii) $\omega_{*0}/\omega_{d0}=0.55$; (iii) and (iv) are just the deeply trapped results of Fig. 4.13 with $\vartheta_0=0.785$ provided for comparison. The difference in the growth rate at $\alpha_h=0$ is due to the fact that ω_{*i} provides a reduction in the MHD growth rate as well as a nonzero real frequency.

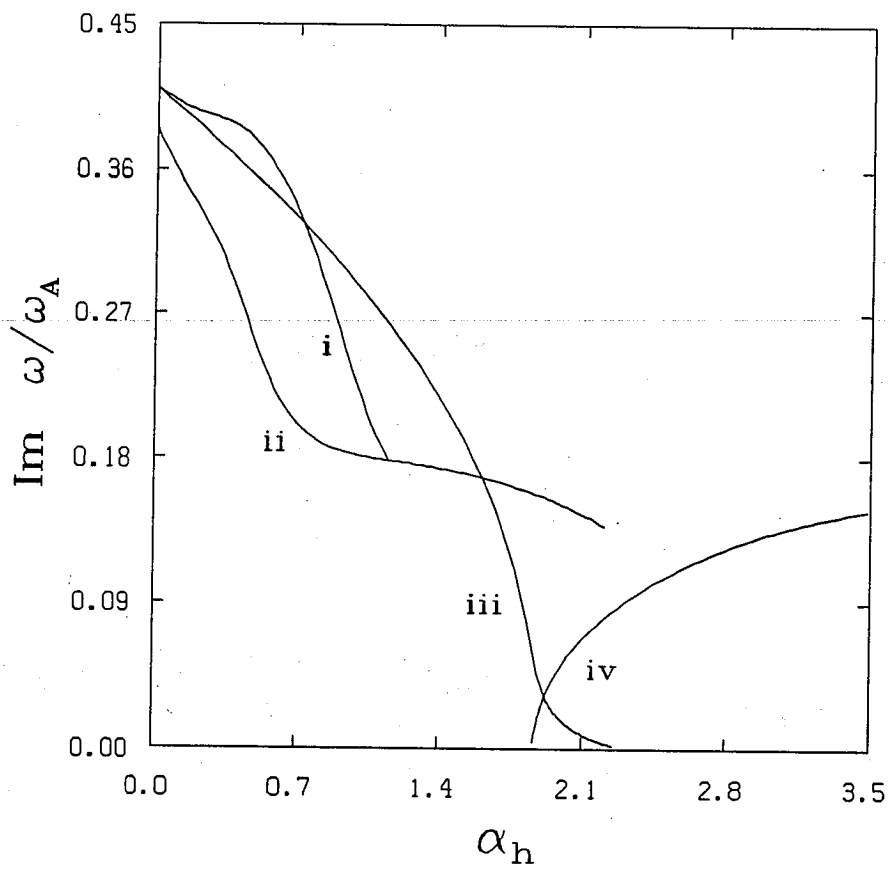


Fig. 4.15. The imaginary part of the eigenvalue plotted as a function of α_h for $\Delta\lambda=0.02$, $\nu_0=3.04$, and (i) $\omega_{*0}/\omega_{d0}=0$, (ii) $\omega_{*0}/\omega_{d0}=0.55$. Curves (iii) and (iv) are similar to the curves labelled (i) in Fig. 4.13; they represent using $\Delta\lambda=10^6$, $\nu_0=0.785$, and $\omega_{*0}/\omega_{d0}=0$.

Consider the first case (i). At the end of the range shown, the growth rate is smaller than in the deeply trapped case. If we consider some point on curve (i) and alter ω_{d0}/ω_A , we note very little change in $\text{Im } \omega$ or $\text{Re } \omega$. In fact, $\text{Re } \omega/\omega_A$ is always quite small in this instance. This indicates that we have not stabilized the MHD ($\omega \ll \omega_d$) root. Note, however, that there are significantly more energetic trapped particles in the tokamak than in the deeply trapped case. Of course, continuing to increase α_h at constant $\Delta\lambda$ will provide stability for the low frequency root, although it may require a great deal of total stored hot particle energy. Two restrictions prevent us from extending curve (i) in this manner. First, it may be that to get α_h large enough to stabilize the low frequency branch, we have to go past $\tau=0$ (Sec. 4.4.a). The other problem is that for $\alpha_h > 1.1$ at $\Delta\lambda=0.02$, the code cannot simultaneously satisfy the boundary conditions $\text{Im } k > 0$ and $\text{Re } \partial\omega/\partial k > 0$ at infinity. In the next subsection we will discuss the reasons for this and examine an alternative approach to the calculation.

Since it is readily acknowledged that ion finite Larmor radius effects (ω_{*i}) improve the stability of the MHD ballooning mode because of the reduced growth rate at $\alpha_h=0$, we ran case (ii) to see if we could get to a point where the eigenmode behaved more like the precessional mode. Indeed, we find that this is the case for $\alpha_h > 0.8$; we also note that the eigenfrequency has a significant

real part, $\text{Re } \omega \sim \omega_d$, as we would expect for the precessional mode. If the sloshing ion distribution is to be effective, the growth rate of the mode should decrease as we place a larger percentage of the turning points near $\vartheta=\pi$. To test this hypothesis, we start with the point at $\alpha_h=1.52$ on curve (ii), reduce $\Delta\lambda$ at constant α_h to $\Delta\lambda=0.013$, and note a drop in $\text{Im } \omega/\omega_A$ to 0.155. This represents a less than 10% reduction in growth rate from that found with $\Delta\lambda=0.02$. Furthermore, at this point we should be concerned with τ going through zero. The boundary condition problems again prevent us from extending curve (ii) farther than shown in Fig. 4.15. These results indicate that the sloshing ions are not strongly stabilizing.

In Fig. 4.16, we present a plot of $\text{Re } \delta Q$ normalized to its value at $\vartheta=0$ as a function of ϑ for the point with $\alpha_h=1.88$ on curve (ii) of Fig. 4.15. Clearly, the eigenfunction exhibits a large peak in the bad curvature region. This could emphasize the influence of the resonant particles and may have something to do with our inability to stabilize the high frequency mode.

4.4.c Asymptotic Solutions (Boundary Condition Problems)

The problem with the boundary conditions arises for $\vartheta_0 \gtrsim 3\pi/4$ at large α_h . In these cases, the calculations indicate that when $\text{Re } \partial\omega/\partial k > 0$ (outgoing waves) at infinity, we must have $\text{Im } k < 0$ (spatially growing waves). The response of the system

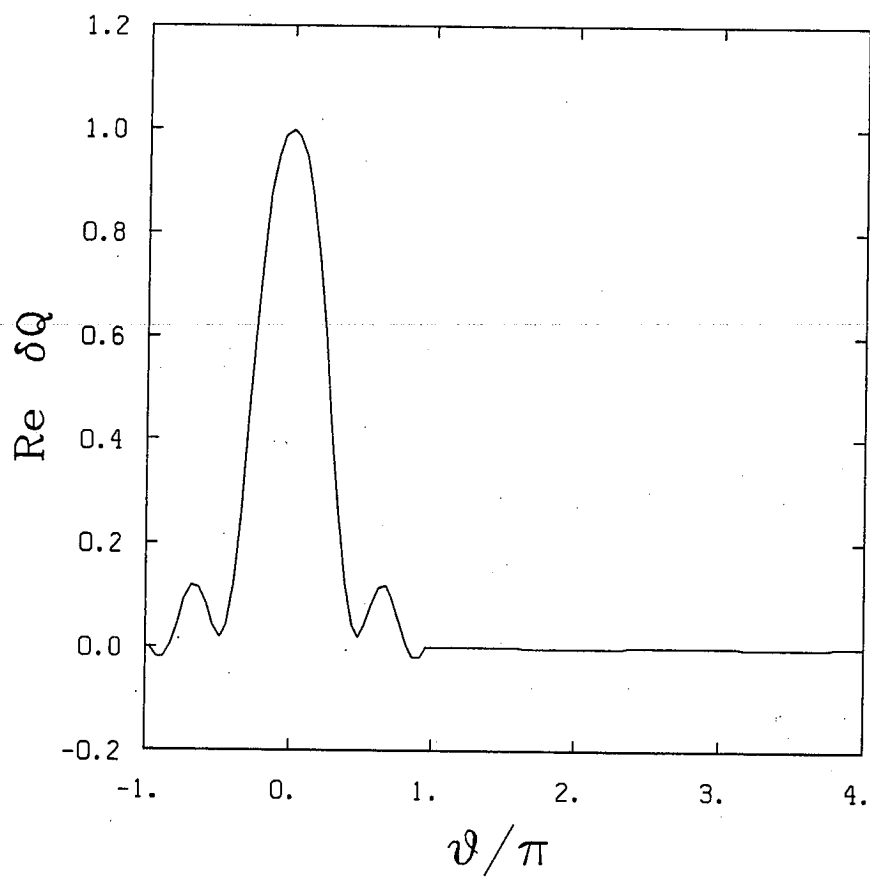


Fig. 4.16. Plot of $\text{Re } \delta Q$ (normalized to its value at $\vartheta=0$) as a function of ϑ . Parameters used here are $\alpha_h=1.88$, $\Delta\lambda=0.02$, $\vartheta_0=3.04$, and $\omega_{*0}/\omega_{d0}=0.55$

near $\varphi=0$ and at infinity are very different due to the appearance of the secular term, $S\varphi$, in $h(\varphi)$ [Eq. (4.15)]. The response near the origin is governed by the specific type of eigenmode being examined; here, it is an even mode centered at the origin. We characterize this response by the growth rate, $\gamma_{\text{eigenmode}}$, which is just the imaginary part of the eigenfrequency. On the other hand, the response at infinity is determined by the local value of $k(\omega)$, the characteristic exponent of the Floquet solution [Eq. (4.23)]. Conversely, we can specify k at infinity and calculate the corresponding value of ω . We search the real- k spectrum and look for the k value which gives the maximum growth rate, γ_{max} .

If $\gamma_{\text{eigenmode}} > \gamma_{\text{max}}$, the response should be spatially damped,¹¹⁸ as we would like to have. On the other hand, if $\gamma_{\text{eigenmode}} < \gamma_{\text{max}}$, we should find spatially growing modes. This is precisely what is happening here. Calculating eigenfrequencies using a spatially growing boundary condition at infinity is undesirable for two reasons. First, from a numerical point of view, the procedure described in Sec. 4.2 would require integrating the differential equation down an exponential gradient; this usually gives rise to spurious results. Secondly, such a mode apparently violates the assumption of $\phi \rightarrow 0$ as $\varphi \rightarrow \infty$ made in deriving the ballooning mode representation.^{8,9} As long as $\gamma_{\text{max}} > 0$, we can always find a localized unstable eigenmode. There should in fact be a continuum of these due to the lack of sensitivity of the

behavior near the origin to the value of ϕ at infinity (where $\phi \rightarrow \infty$). If we can arrange it so that $\gamma_{\max} = 0$ (by using the sloshing ion distribution, etc.), then all unstable eigenmodes will be spatially damped, and we can safely search for them using the approach described in Sec. 4.2. However, the most unstable mode may not be even about $\phi = 0$, as we have assumed heretofore.

In the limit of $\phi \rightarrow \infty$, Eqs. (4.17a) and (4.17b) become

$$\frac{d}{d\phi} \left(\sigma \frac{d\phi}{d\phi} \right) + \frac{\omega^2}{\omega_A^2} \phi = - \sin\phi \sigma \delta Q \text{ qr} R_0, \quad (4.41a)$$

$$\tau \delta Q = m_h \int d^3v \frac{\omega - \omega_*}{\omega - \langle \omega_d \rangle} \mu^2 \frac{\partial F_h}{\partial E} \left[\langle \delta Q \rangle + \frac{q}{r R_0} \frac{\langle \sigma \phi \sin\phi \rangle}{\tau} \right], \quad (4.41b)$$

where we have dropped the $2\epsilon \cos\phi$ in the inertia term for simplicity, and we will ignore ω_{*i} effects here. As an interesting side comment, note that since ω_{*i} involves

$$\hat{e} \cdot \nabla P_{\perp h} = \hat{e} \cdot \hat{\nabla} P_{\perp h} + \hat{e} \cdot \nabla B \frac{\partial P_{\perp h}}{\partial B};$$

it will introduce an extra secular term (through $\hat{e} \cdot \nabla B$) one order higher in $S\phi$ than the terms shown in Eqs. (4.40a) and (4.40b), so that if we were to include ω_{*i} with $|(1/B)\partial P_{\perp h}/\partial B| \lesssim 1$, it would be necessary to consider its contribution to be dominant at infinity!

Examining Eqs. (4.41a) and (4.41b) more closely, we note that it has exact Floquet solutions, $\phi(\vartheta) = \hat{\phi}(\vartheta) e^{ik\vartheta}$, where, unlike the case described in Sec. 4.2, k is a constant. Thus, modes proportional to $e^{ik\vartheta}$ with k real are proper continuum eigenmodes. If $\vartheta_0 \ll \pi$, we see that $\langle \phi \sin \vartheta \rangle \approx 0$, so $\delta Q \approx 0$ and $k = \pm \omega / \omega_A$. If this were always the case, there would be no problem. But, as we increase ϑ_0 , $\langle \phi \sin \vartheta \rangle$ becomes significant, and its effect on Eqs. (4.41a) and (4.41b) becomes larger; note that δQ is also proportional to α_h . Thus, it is not surprising that γ_{\max} can be positive. Physically, we have positive energy shear Alfvén waves at infinity, $\omega = \omega_A$. These are readily destabilized by the negative dissipation arising out of the drift resonance in Eq. (4.41b).

It should be noted that because of the symmetry of Eqs. (4.41a) and (4.41b), the two solutions for k (call them k_+ and k_-) obtained by the procedure given in Sec. 4.2 are equal in magnitude and of opposite sign: $k_+ = -k_-$. Then, a solution satisfying the pinch point conditions¹¹⁸

$$D(k, \omega) = 0 \quad \text{and} \quad \frac{\partial D}{\partial k}(k, \omega) = 0,$$

where $D(k, \omega)$ is the effective dispersion relation for the system, occurs at $k=0$ (purely periodic solutions). At this point k_+ and k_- come together to form a double root to the dispersion relation.

Near $k=0$, we must then have $D(k, \omega) = ak^2 - (\omega - \omega_0)$, where "a" and ω_0 are constants. Numerically, it is found that $\text{Im } \omega_0 > 0$ and $\text{Im } a < 0$, so that the local maximum in the growth rate for real k 's is at $k=0$. Numerical searches over the whole range of k in this case indicate that $k=0$ is an absolute maximum as well; hence, $\gamma_{\text{max}} = \text{Im } \omega_0$.

It then becomes straightforward to set up an iterative scheme to search for the value of ω in Eqs. (4.41a) and (4.41b) that yields $k=0$. Using the same parameters as in Fig. 4.15, $\vartheta_0=3.04$, $\omega_{d0}/\omega_A = 0.636$, $\omega_{*i}/\omega_A = 0$, $\Delta_r/r=0$, $\alpha_c=0.8$, $S=0.6$, but fixing $\alpha_H=1.52$, we compute $\gamma_{\text{max}} = \text{Im } \omega/\omega_A$ ($k=0$) as a function of $\Delta\lambda$ [curve (i) in Fig. 4.17]. The stabilizing effect of the peaked distribution is clearly apparent at small $\Delta\lambda$. The last point shown in curve (i) of Fig. 4.17 represents $\Delta\lambda = 2 \times 10^{-4}$, $\gamma_{\text{max}} \approx 0.036$; complete stabilization could be effected by continuing to lower $\Delta\lambda$. On the other hand, this growth rate is still larger than $\gamma_{\text{MHD}}/10$, and if we were to compute τ using some reasonable nonzero value of Δ_r/r , we would certainly find $\tau < 0$. The stabilization arises from an overall increase in the number of particles with $\omega_* < \omega_d < 0$. These particles are nonresonant and give no contribution to the negative dissipation term. However, some particles trapped in the bad curvature region remain regardless of the value of $\Delta\lambda$ and we get $\gamma_{\text{max}} > 0$.

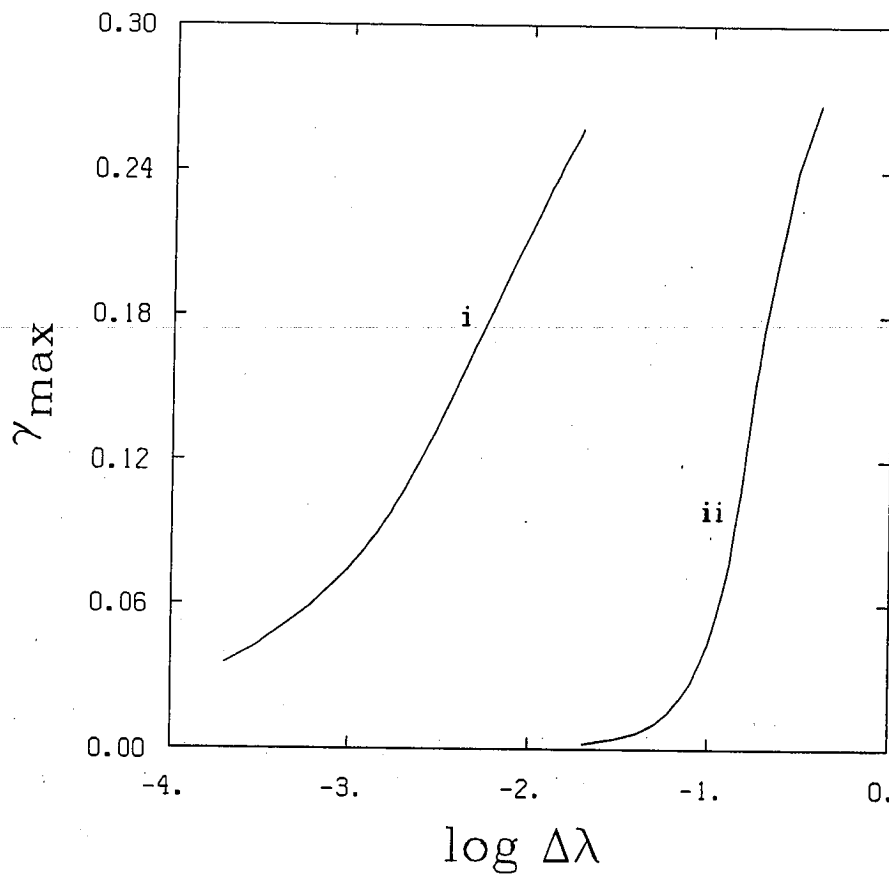


Fig. 4.17. Plot of γ_{\max} as a function of $\log \Delta\lambda$ for the $k=0$ mode with $\alpha_h=1.52$ using: (i) the purely-trapped distribution, Eq. (4.34) and (ii) the trapped and circulating distribution, Eq. (4.36).

Now, we consider the distribution containing both trapped and circulating energetic particles, Eq. (4.36). Calculating γ_{\max} with the parameters used in curve (i) of Fig. 4.15 at $\alpha_h=0.5$ yields $\gamma_{\max} = 0.0075 \omega_A$ [curve (ii) in Fig. 4.17], significantly smaller than the growth rates predicted in curves (i) and (ii) of Fig. 4.15. Increasing α_h at this point has the effect of lowering γ_{\max} even more. We then expect that the continuum instability will not interfere with the large ϑ boundary conditions used in solving Eqs. (4.17a) and (4.17b) as it did with the purely-trapped distribution. The fact that we have essentially stabilized this mode indicates that the dominant contribution to the kinetic integral is from particles with $\omega_* < \omega_d < 0$, as we had hoped to achieve at the outset.

When we repeat the calculations leading to curve (i) of Fig. 4.15 with the circulating-trapped distribution replacing the one in Eq. (4.34), we find qualitatively the same results as shown in curves (i) and (ii) of Fig. 4.15 for $\alpha_h \leq 1.6$. That is, we do not find a marginally stable point for the localized eigenmode. However, calculations for $\alpha_h > 1.6$ again lead to unsatisfactory boundary conditions at infinity. Further investigation of Eqs. (4.41a) and (4.41b) in this case indicates that while the branch of solutions with γ_{\max} occurring at $k=0$ may be nearly stable, another branch with the growth rate for real k 's peaking at $k = 1/2$ (solutions have period 4π) is clearly unstable. Whereas

the mode frequencies at $k=0$ had significant real parts indicative of a wave-precessional drift resonance, the ones calculated at $k = 1/2$ are almost purely imaginary with γ_{\max} on the order of MHD growth rates. As was the case with $k=0$, the two values of k found using Eq. (4.26) form a double root; $k = -1/2$ is equivalent to $k = +1/2$ since shifts by integer amounts do not change the result [see Eq. (4.23)]. At $k = 1/2$, we satisfy the pinch-point conditions for this branch of continuum solutions.

This instability arises due to the presence of a large energetic particle pressure peak in the good curvature region. Normally, one would think of this as aiding stability via the fluid pressure gradient - curvature terms on the left-hand side of Eq. (4.2a). The large pressure peak and low mode frequency allow us to assume that $|\omega/\langle\omega_d\rangle| \ll 1$, at least for the dominant part of the pitch angle distribution. In this case, we obtain a result familiar from EBT theory. Namely, the energetic particles produce through the kinetic term a contribution similar in magnitude but opposite in sign to the fluid pressure gradient - curvature terms (i.e., the energetic particles dig a diamagnetic well; see Sec. 3.2). In situations involving average good curvature, the stabilizing fluid terms dominate so that the ballooning instability does not arise. In Eqs. (4.41a) and (4.41b), however, the fluid terms do not appear since they are smaller than the field-line bending and inertia terms by a factor of $1/S\delta$. The kinetic

contribution, destabilizing in good curvature and represented by δQ on the right-hand side of Eq. (4.41a), is then uncanceled except for a small amount of field-line bending entering through the $d^2\phi/d\vartheta^2$ term. That δQ has a sign consistent with instability can be seen if we look at Eq. (4.41b) under the assumptions that $\omega \ll \langle \omega_d \rangle$, $\langle \delta Q \rangle < \langle \phi(q/rR_0) \sin\vartheta \rangle$, and note that $\omega_* \frac{\partial F_h}{\partial E} / \langle \omega_d \rangle > 0$ in good curvature. Since this kinetic term is comparable in magnitude to the fluid MHD instability drive terms, we expect the resultant instability to have γ_{\max} on the order of MHD growth rates. While it appears that there should be a stability threshold for this mode if α_h is small enough (because of the stabilizing influence of the field-line bending term), numerical calculations indicate a nonzero growth rate for $\alpha_h > 0$, as shown in Fig. 4.18. For large α_h , the mode frequency is largely imaginary, but becomes mostly real for small α_h ($\alpha_h < 0.7$ in this case), as can be seen in Fig. 4.19. When α_h is lowered, the mode becomes less like a fluid MHD instability driven by the energetic particle pressure and more like an Alfvén wave that is destabilized by the negative dissipation of the energetic particles. The transition should occur when the real and imaginary parts of Eq. (4.41b) are comparable. We will examine this mode in a more quantitative manner in the Sec. 4.4.e.

From these results, we can conclude that if $\omega_* \langle \omega_d \rangle > 0$ on average, the continuum instability with growth rate peaking at $k=0$ will be present, whereas if $\omega_* \langle \omega_d \rangle < 0$, the one at $k = 1/2$ appears.

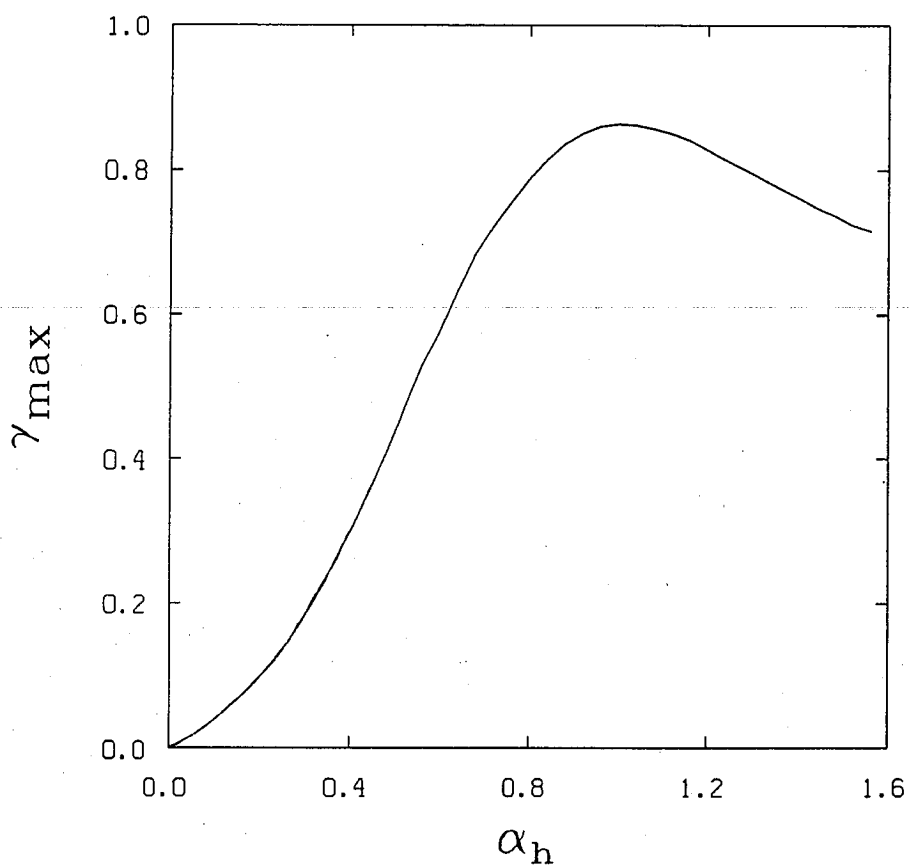


Fig. 4.18. Plot of γ_{\max} as a function of α_h for the $k = 1/2$ mode using the trapped and circulating distribution, Eq. (4.36), with $\Delta\lambda=0.02$, $\omega_{d0}/\omega_A = 5$, $\alpha_c = 0$.

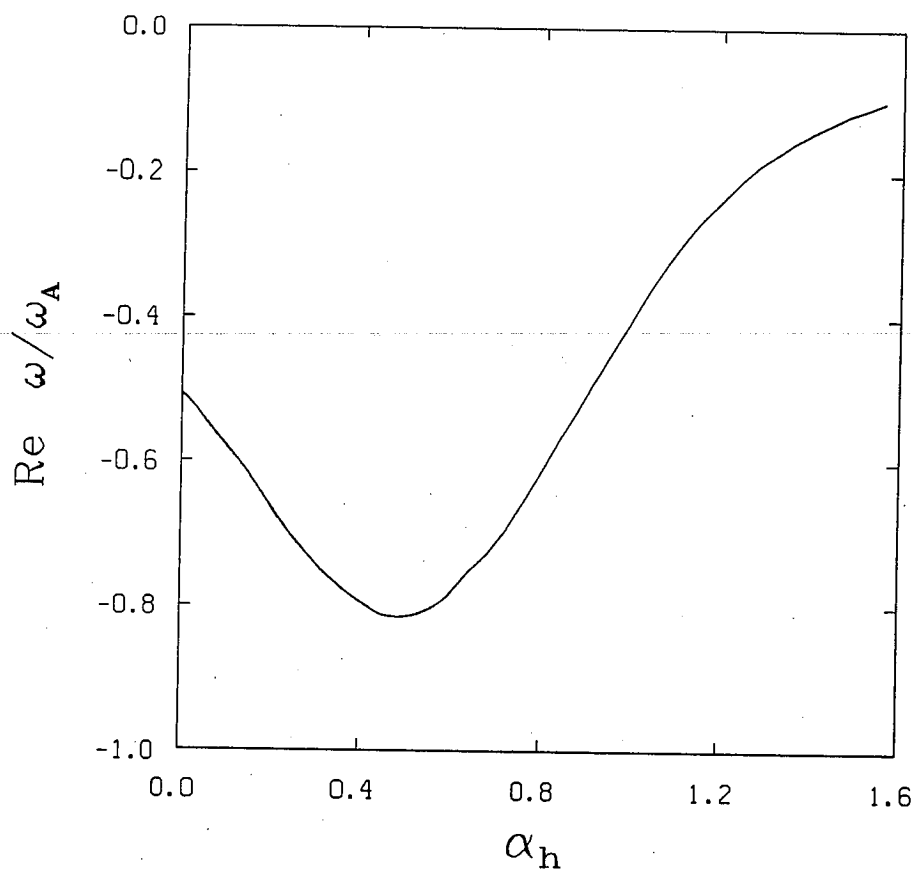


Fig. 4.19. Plot of the real part of the frequency as a function of α_h for the $k = 1/2$ mode using the trapped and circulating distribution, Eq. (4.36), with $\Delta\lambda=0.02$, $\omega_{d0}/\omega_A = 5$, $\alpha_c = 0$.

We should emphasize that a sloshing distribution (so that $\langle \phi \sin \vartheta \rangle$ is not small) and high bounce frequency ordering (so that δQ enters Eq. (4.41a) at the same order as the other two terms) are necessary for these modes to be unstable.

4.4.d Analytic Results: Full Eigenmode Equations

We now examine Eqs. (4.17a) and (4.17b) analytically and attempt to understand the conditions for stabilizing the precessional mode; a similar analysis for the $k = 1/2$ continuum instability will be presented in Sec. 4.4.e. For simplicity, we set $\Delta_r/r=0$, $\sigma=\tau=1$ and $\omega_{*i}=0$. To do the pitch angle integral in Eq. (4.17b), we assume that all of the averages can be evaluated at some representative pitch angle for the distribution λ_* . For example, if all of the particles were deeply trapped, we would set $\lambda_* = B_c/B_{\min}$; this amounts to evaluating the averaged quantity at $\vartheta=0$ and becomes exact in the limit $\vartheta_0 \rightarrow 0$. On the other hand, for a purely sloshing distribution, we would use $\lambda_* \approx 1$. The rest of the velocity integrations can be done exactly using the distribution specified in Eq. (4.34).

Solving for δQ in this manner, we obtain

$$\delta Q = \frac{-\langle \Phi D(\vartheta) / (1+h^2)^{1/2} \rangle \frac{\alpha_h}{2} p_{\perp}(\vartheta) H(a)}{\langle D(\vartheta) \rangle - \frac{\alpha_c}{2q^2} - \frac{\alpha_h}{2q^2} \langle p_{\perp}(\vartheta) \rangle [1-H(a)]}, \quad (4.42)$$

where $H(a)$ arises from doing the energy integral, and is given by (Sec. 3.3.a)

$$H(a) = 1 + \frac{2}{5}a + \frac{4}{15}a^2 + \frac{8}{15}a^3 + \frac{8}{15}a^{7/2}Z(a^{1/2}), \quad (4.43)$$

with Z being the plasma dispersion function and

$$a = -\frac{\omega}{\omega_{d0}} \langle \lambda [D(\vartheta) - \frac{\alpha_c}{2q^2} - \frac{\alpha_h}{2q^2} p_{\perp}(\vartheta)] \rangle^{-1}.$$

The angle brackets indicate a bounce average along the field line, as before, but evaluated at the specified pitch angle λ_* . We will retain this convention for the rest of this sub-section.

Note that the only field line dependence in Eq. (4.42) is $p_{\perp}(\vartheta)$. It is quite apparent, however, from Fig. 4.16 that the actual eigenfunction can differ significantly from the simple double-humped form we expect to see for $\Delta\lambda=0.02$ (see Fig. 4.12). This discrepancy points out one of the problems with such a simple

analysis; nonetheless, we hope to be able to achieve here a qualitative understanding of the precessional mode.

We now substitute Eq. (4.42) for δQ into Eq. (4.17a), and rearrange terms so that the ω dependence is isolated,

$$\begin{aligned} \frac{d^2\phi}{d\vartheta^2} - \frac{\phi}{(1+h^2)} \left[\frac{(dh/d\vartheta)^2}{(1+h^2)} + h \frac{d^2h}{d\vartheta^2} \right] + \frac{\phi D(\vartheta)}{(1+h^2)} \left[\alpha_c + \frac{\alpha_h}{2} p_{\perp}(\vartheta) \right] + \frac{\omega^2}{\omega_A^2} \phi \\ = \frac{\alpha_h}{2} \frac{D(\vartheta) p_{\perp}(\vartheta)}{(1+h^2)^{1/2}} \frac{\langle \phi D / (1+h^2)^{1/2} \rangle}{\alpha_h \langle p_{\perp} \rangle / 2q^2} \\ - \frac{\alpha_h}{2} \frac{D(\vartheta) p_{\perp}(\vartheta)}{(1+h^2)^{1/2}} \frac{\langle \phi D / (1+h^2)^{1/2} \rangle}{\alpha_h \langle p_{\perp} \rangle / 2q^2} \\ \times \frac{\langle D \rangle - \frac{\alpha_c}{2q^2} - \frac{\alpha_h}{2q^2} \langle p_{\perp} \rangle}{\langle D \rangle - \frac{\alpha_c}{2q^2} - \frac{\alpha_h}{2q^2} \langle p_{\perp} \rangle (1-H)} \end{aligned} \quad (4.44)$$

This equation is of the form

$$\frac{d^2\phi}{d\vartheta^2} + G(\phi; \vartheta) = 0. \quad (4.45)$$

So, we can solve for $\frac{d\phi}{d\vartheta}(\vartheta_0)$:

$$\frac{d\phi}{d\vartheta}(\vartheta_0) = - \int_0^{\vartheta_0} d\vartheta G(\phi; \vartheta); \quad (4.46)$$

we have made use of the fact that only even eigenmodes are being considered here, $\frac{d\phi}{d\vartheta}(\vartheta=0)=0$.

Now, to make further progress, we assume that the energetic particles are important only over the range $-\vartheta_0 \leq \vartheta \leq \vartheta_0$; this assumption is supported by the fact that the amplitude of the eigenfunction shown in Fig. 4.16 is small for $\vartheta \geq \pi$. Then, solving Eq. (4.45) for $\vartheta > \vartheta_0$ becomes basically an MHD problem. We presume that this has been done and treat $\frac{1}{\phi} \frac{d\phi}{d\vartheta}(\vartheta_0)$ as a known quantity. This term represents the removal of energy off to infinity in the form of shear Alfvén waves and is thus a source of positive dissipation. Were we to match onto shear Alfvén waves at ϑ_0 , we would find $\frac{d}{d\vartheta} \ln \phi = i\omega/\omega_A$. The correct result is considerably different from this, but the imaginary part should still have the same sign,

$$\left(\operatorname{Im} \frac{d}{d\vartheta} \ln \phi \right) \left(\operatorname{Re} \frac{\omega}{\omega_A} \right) > 0,$$

so that the positive dissipation remains.⁹⁴ Similarly, when ω has a

positive imaginary part, assuming that $\frac{d}{d\vartheta} \ln \phi$ has the same sign as $i\omega/\omega_A$ implies $\text{Re} \frac{d}{d\vartheta} \ln \phi < 0$.

Furthermore, we take $\phi = \text{constant}$ over $0 < \vartheta < \vartheta_0$ to obtain

$$\begin{aligned} & \left[\frac{\omega^2}{\omega_A^2} + \frac{1}{\vartheta_0} \frac{d}{d\vartheta} \ln \phi(\vartheta_0) + \gamma_c^2 + \gamma_h^2 - \gamma_h'^2 \frac{\langle D/(1+h^2)^{1/2} \rangle}{\alpha_h \langle p_{\perp} \rangle / 2q^2} \right] \\ & + \left(\gamma_h'^2 \frac{\langle D/(1+h^2)^{1/2} \rangle}{\alpha_h \langle p_{\perp} \rangle / 2q^2} \left[\langle D \rangle - \frac{\alpha_c}{2q^2} - \frac{\alpha_h}{2q^2} \langle p_{\perp} \rangle \right] \right) \\ & \times \left[\langle D \rangle - \frac{\alpha_c}{2q^2} - \frac{\alpha_h}{2q^2} \langle p_{\perp} \rangle (1-H) \right]^{-1} = 0, \end{aligned} \quad (4.47)$$

where

$$\gamma_c^2 \equiv \int_0^{\vartheta_0} \frac{d\vartheta}{\vartheta_0} \left\{ \frac{\alpha_c D(\vartheta)}{(1+h^2)} - \frac{1}{(1+h^2)} \left[\frac{(dh/d\vartheta)^2}{(1+h^2)} + h \frac{d^2 h}{d\vartheta^2} \right] \right\},$$

$$\gamma_h^2 \equiv \int_0^{\vartheta_0} \frac{d\vartheta}{\vartheta_0} \frac{\alpha_h}{2} \frac{p_{\perp}(\vartheta) D(\vartheta)}{(1+h^2)},$$

$$\gamma_h'^2 \equiv \int_0^{\vartheta_0} \frac{d\vartheta}{\vartheta_0} \frac{\alpha_h}{2} \frac{p_{\perp}(\vartheta) D(\vartheta)}{(1+h^2)^{1/2}}$$

For a deeply-trapped distribution, Eq. (4.47) provides a good approximation to the eigenvalue ω if we can evaluate $\frac{d}{d\vartheta} \ln \phi(\vartheta_0)$ in terms of ω . To demonstrate this, we consider parameter values: $\alpha_h=4.7$, $\alpha_c=0.8$, $S=0.6$, $r/R_0=0.2$, $\vartheta_0=0.45$, $q=2$, $\Delta\lambda=10^6$, and $\omega_{d0}/\omega_A=0.8$. Numerical solution of Eqs. (4.17a) and (4.17b) in this case yields $\Omega \equiv \omega/\omega_A = -0.25 + 0.005i$, and $\frac{d}{d\vartheta} \ln \phi(\vartheta_0) = -0.038 - 0.029i$. $\frac{d}{d\vartheta} \ln \phi(\vartheta_0)$ was obtained by integrating Eqs. (4.17a) and (4.17b) numerically from $\vartheta_m = 2\pi m$ (here, $m=2$) to ϑ_0 in the manner described in Sec. 4.2 using $\Omega = -0.25 + 0.005i$.

In the deeply-trapped case, $h \ll 1$, and in fact $h \rightarrow 0$ as $\vartheta \rightarrow 0$. So, $D(\vartheta) \approx \cos\vartheta$, and since $\cos\vartheta$ varies only slightly over $\vartheta = 0 \rightarrow 0.45$, we can reasonably assume $\langle D \rangle \approx 1$. On the other hand, $p_{\perp}(\vartheta)$ falls sharply from 1 to 0 over the same interval. If we choose $\lambda_* = 1.02 \lesssim B_c/B_{\min}$, $\langle p_{\perp} \rangle = 0.85$ and $\langle \omega_d \rangle / \omega_{d0} = -0.39$; the turning point at this pitch angle is $\vartheta_T(\lambda_*) = 0.2$.

In calculating γ_c^2 , it should be noted that $\frac{dh}{d\vartheta} = S - \alpha_c \cos\vartheta - \alpha_h \frac{dg}{d\vartheta}$ is not necessarily small compared to unity and should not be neglected; it is, however, slowly varying over $\vartheta = 0 \rightarrow \vartheta_0$, so that

$$\gamma_c^2 \approx \alpha_c - \left[\frac{dh}{d\vartheta}(\vartheta=0) \right]^2.$$

We can either estimate using the expression for $g(\vartheta)$ following Eq. (4.14) or calculate numerically that $\frac{dg}{d\vartheta}(\vartheta=0) \approx 0.2$. So, $\gamma_c^2 \approx 0.71$. Using $h \approx 0$ and $D(\vartheta) \approx 1$, we see

$$\gamma_h^2 \approx \gamma_h'^2 \approx \frac{\alpha_h}{2} \int_0^{\vartheta_0} \frac{d\vartheta}{\vartheta_0} p_{\perp}(\vartheta);$$

with these parameters, $\gamma_h^2 \approx 1.4$.

Since $\text{Im } \omega \ll |\text{Re } \omega|$, the real and imaginary pieces of the dispersion relation, Eq. (4.47), can be easily separated. Setting $h=0$ in the imaginary part and solving it for $\text{Im } H$, we find

$$\text{Im } H \approx \frac{\text{Im}\left(\frac{1}{\vartheta_0} \frac{d}{d\vartheta} \ln \phi\right) \left[\langle D \rangle - \frac{\alpha_c}{2q^2} - \frac{\alpha_h \langle p_{\perp} \rangle}{2q^2} (1 - \text{Re } H)\right]}{\gamma_h^2 \left(\langle D \rangle - \frac{\alpha_h \langle p_{\perp} \rangle}{2q^2}\right) - \frac{\alpha_h \langle p_{\perp} \rangle}{2q^2} \left[\Omega^2 + \text{Re}\left(\frac{1}{\vartheta_0} \frac{d}{d\vartheta} \ln \phi\right) + \gamma_c^2\right]} \quad (4.48)$$

Using the information given above, we can argue that $\Omega^2 + \text{Re}\left(\frac{1}{\vartheta_0} \frac{d}{d\vartheta} \ln \phi\right)$ is small relative to γ_c^2 . Furthermore, since $\frac{\alpha_h \langle p_{\perp} \rangle}{2q^2} < 1$ and $\text{Re } H \sim O(1)$, we can also neglect the last term in the numerator. Thus,

$$\text{Im } H \cong \frac{\text{Im}\left(\frac{1}{\psi_0} \frac{d}{d\psi} \ln \phi\right) \left(\langle D \rangle - \frac{\alpha_c}{2q^2}\right)}{\left[\gamma_h^2 \left(\langle D \rangle - \frac{\alpha_h \langle p_\perp \rangle}{2q^2}\right) - \frac{\alpha_h \langle p_\perp \rangle}{2q^2} \gamma_c^2\right]} \quad (4.49)$$

Now, the only terms depending on ω are $\text{Im } H = -\frac{8}{15} \sqrt{\pi} |a^{7/2}| e^{-a}$ (for real $a > 0$ and $\omega < 0$; see Sec. 3.3.a) and $\text{Im}\left(\frac{1}{\psi_0} \frac{d}{d\psi} \ln \phi\right)$. Although we do not have a closed-form expression for $\text{Im}\left(\frac{1}{\psi_0} \frac{d}{d\psi} \ln \phi\right)$, we do know its value for these parameters and can use it in Eq. (4.49) to calculate $|a^{7/2}| e^{-a} \cong 0.18$. Hence, $a \cong \omega / \langle \omega_d \rangle \cong 0.76$; with $\langle \omega_d \rangle = (0.8)(-0.39)\omega_A$, we obtain $\Omega \cong -0.24$, in good agreement with the full numerical result of $\Omega \cong -0.25$. It should be noted that in the deeply-trapped limit, the assumptions $\delta Q \approx \text{constant} \times p_\perp(\psi)$ and $\phi \approx \text{constant}$ over $\psi = 0 \rightarrow \psi_0$ are quite accurate so that this kind of agreement is expected.

The dispersion relation Eq. (4.47) has the form $A(\Omega) + C/B(\Omega) = 0$, or

$$A(\Omega)B(\Omega) + C = 0, \quad (4.50)$$

with

$$A(\Omega) = \Omega^2 + \frac{1}{\psi_0} \frac{d}{d\psi} \ln \phi(\psi_0) + \gamma_c^2 + \gamma_h^2 - \gamma_h^2 \frac{\langle D / (1+h^2) \rangle^{1/2}}{\alpha_h \langle p_\perp \rangle / 2q^2},$$

$$B(\Omega) = \frac{[\langle D \rangle - \frac{\alpha_c}{2q^2} - \frac{\alpha_h}{2q^2} \langle p_{\perp} \rangle (1-H)]}{(\langle D \rangle - \frac{\alpha_c}{2q^2} - \frac{\alpha_h}{2q^2} \langle p_{\perp} \rangle)}$$

$$C = \gamma_h^2 \frac{\langle D / (1+h^2)^{1/2} \rangle}{\alpha_h \langle p_{\perp} \rangle / 2q^2}$$

and $\Omega = \omega / \omega_A$. We suggest that lowest order solutions are $\text{Re } A(\Omega_1) \equiv A_R(\Omega_1) = 0$ and $\text{Re } B(\Omega_2) \equiv B_R(\Omega_2) = 0$, with Ω_1, Ω_2 real (the last term in A should be large enough to allow this to be true), and that $\text{Im } A \equiv A_I, \text{Im } B \equiv B_I, C$ are typically small in comparison with A_R and B_R . Then, we can write the full solution to Eq. (4.48) as $\Omega = \Omega_1 + \delta\Omega_1 = \Omega_2 + \delta\Omega_2$, with $\delta\Omega_1, \delta\Omega_2 \ll \Omega$. Expanding A and B about Ω_1 and Ω_2 , respectively, Eq. (4.50) becomes approximately

$$\begin{aligned} & [(\Omega - \Omega_1) \frac{\partial A_R}{\partial \Omega}(\Omega_1) + iA_I(\Omega_1)] \\ & \times [(\Omega - \Omega_2) \frac{\partial B_R}{\partial \Omega}(\Omega_2) + iB_I(\Omega_2)] + C = 0, \end{aligned} \quad (4.51)$$

where

$$\frac{\partial A_R}{\partial \Omega}(\Omega_1) \cong 2\Omega_1,$$

$$A_I = \text{Im} \left[\frac{1}{\psi_0} \frac{d}{d\psi} \ln \phi(\psi_0) \right],$$

$$\frac{\partial B_R}{\partial \Omega}(\Omega_2) = - \frac{\omega_A}{\omega_{d0}} \frac{\frac{\alpha_h \langle p_{\perp} \rangle}{2q^2} \frac{d}{da} (\text{Re } H)}{\left[\langle D \rangle - \frac{\alpha_c}{2q^2} - \frac{\alpha_h \langle p_{\perp} \rangle}{2q^2} \right]^2},$$

and

$$B_I(\Omega_2) = \frac{\frac{\alpha_h \langle p_{\perp} \rangle}{2q^2} \text{Im } H}{\langle D \rangle - \frac{\alpha_c}{2q^2} - \frac{\alpha_h \langle p_{\perp} \rangle}{2q^2}}.$$

We have neglected any contribution to $\frac{\partial A_R}{\partial \Omega}$ made by $\frac{d}{d\psi} \ln \phi(\psi_0)$; this is consistent with assuming $\frac{d}{d\psi} \ln \phi(\psi_0) = i\Omega$ (the derivative then has no real part). This dispersion relation exhibits the typical form for the interaction of two waves, each with its associated dissipation, providing two damped roots in the limit $C \rightarrow 0$ [assuming $A_I/(\partial A_R/\partial \Omega)$ and $B_I/(\partial B_R/\partial \Omega)$ are positive, as we will show below].

The normalization we use here is that $\langle \omega_d \rangle / \omega_A < 0$ without drift reversal, i.e., when $\langle D \rangle - \frac{\alpha_c}{2q^2} - \frac{\alpha_h \langle p_{\perp} \rangle}{2q^2} > 0$. With drift

reversal, each of these quantities changes sign, e.g., $\langle \omega_d \rangle / \omega_A > 0$.

The solution of $B_R(\Omega_2) = 0$ implies that

$$\text{Re } H = \frac{-[\langle D \rangle - \frac{\alpha_c}{2q^2} - \frac{\alpha_h}{2q^2} \langle p_{\perp} \rangle]}{\frac{\alpha_h}{2q^2} \langle p_{\perp} \rangle}, \quad (4.52a)$$

or

$$\text{Re } H - 1 = \frac{-[\langle D \rangle - \frac{\alpha_c}{2q^2}]}{\frac{\alpha_h}{2q^2} \langle p_{\perp} \rangle}. \quad (4.52b)$$

Solutions to these equations without drift reversal are such that $a > 0$. For instance, near drift reversal, the right-hand side of Eq. (4.52a) is small and negative; at the same time $|a| = |\omega / \langle \omega_d \rangle|$ should be large since $\langle \omega_d \rangle$ is near zero. We can then use the asymptotic expansion for $Z(a^{1/2})$ to find⁷⁰

$$H(a) \cong -\frac{7}{2a}. \quad (4.53)$$

Thus,

$$a \cong \frac{\frac{2}{7} \frac{\alpha_h \langle p_{\perp} \rangle}{2q^2}}{[\langle D \rangle - \frac{\alpha_c}{2q^2} - \frac{\alpha_h \langle p_{\perp} \rangle}{2q^2}]}$$

or equivalently

$$\Omega_2 \cong - \frac{\omega_{d0}}{\omega_A} \frac{\alpha_h}{7q^2} \langle p_{\perp} \rangle. \quad (4.54)$$

Eq. (4.54) then implies that $\Omega_2 < 0$, at least near drift reversal, so $a > 0$ when $\langle \omega_d \rangle < 0$, and $a < 0$ if $\langle \omega_d \rangle > 0$. Numerical calculations for larger values of $|\langle \omega_d \rangle|$ indicate that $a > 0$ in general without drift reversal. However, it is clear from Eq. (4.52b) that $a \rightarrow 0$ as $\langle D \rangle - \frac{\alpha_c}{2q^2} \rightarrow 0$ since

$$\text{Re } H \cong 1 + \frac{2}{5} a \quad (4.55)$$

for $|a| \ll 1$. Thus when $|\langle D \rangle - \frac{\alpha_c}{2q^2}| / \frac{\alpha_h \langle p_{\perp} \rangle}{2q^2} \ll 1$, we find

$$a \cong - \frac{5}{2} \frac{[\langle D \rangle - \frac{\alpha_c}{2q^2}]}{\frac{\alpha_h \langle p_{\perp} \rangle}{2q^2}}$$

so,

$$\Omega_2 \cong \frac{5}{2} \frac{\omega_{d0}}{\omega_A} \frac{(\langle D \rangle - \frac{\alpha_c}{2q^2})(\langle D \rangle - \frac{\alpha_c}{2q^2} - \frac{\alpha_h}{2q^2} \langle p_{\perp} \rangle)}{\frac{\alpha_h}{2q^2} \langle p_{\perp} \rangle} \quad (4.56)$$

Clearly, $\Omega_2 < 0$ and $a < 0$ with drift reversal if $\langle D \rangle - \frac{\alpha_c}{2q^2} > 0$. This is just as we find using Eq. (4.54). However when $\langle D \rangle - \frac{\alpha_c}{2q^2} < 0$, Ω_2 is positive. Since we must in this case also have $\langle \omega_d \rangle > 0$ (i.e., $\langle D \rangle - \frac{\alpha_c}{2q^2} - \frac{\alpha_h}{2q^2} \langle p_{\perp} \rangle < 0$), "a" is also positive.

When we solve $A_R(\Omega_1) = 0$, only Ω_1^2 is determined if we neglect any contribution made by $\text{Re}(\frac{1}{v_0} \frac{d}{dv} \ln \phi)$. Since we require $\Omega_1 \approx \Omega_2$ for our method to be valid, it is necessary to pick the sign of Ω_1 such that $\Omega_1 = \text{sgn}(\Omega_2) |\Omega_1|$.

Now we can specify the signs of the various quantities in Eq. (4.51). As long as $D(\psi) > 0$, $C > 0$. Computing a bounce average of $D(\psi)$ implies a weighting along the field line much like that used in calculating $\gamma_h'^2$ where the weighting function is approximately $p_{\perp}(\psi)$. Thus, $\langle D/(1+h^2)^{1/2} \rangle$ and $\gamma_h'^2$ should have the same sign in most cases even if $D(\psi) < 0$ for some distance along the field line. It is then reasonable to assume $C > 0$ in general.

The signs of $\frac{\partial A_R}{\partial \Omega}$ and A_I should follow that of Ω_1 , as discussed above. To determine $\frac{\partial B_R}{\partial \Omega}$ we need to know $\frac{d}{da}(\text{Re } H)$. From both Eq. (4.53) and Eq. (4.55), it appears that $\frac{d}{da}(\text{Re } H) > 0$. Numerical calculations for values of "a" intermediate between those for which Eqs. (4.53) and (4.55) are valid indicate that this is always the case. Thus, $\frac{\partial B_R}{\partial \Omega} < 0$ in all instances.

If we note that $\text{Im } Z(\zeta) = \sqrt{\pi} \exp(-a^2)$ for ζ real, and $\text{Re } Z(\zeta) = 0$ when ζ is purely imaginary,

$$B_I = \begin{cases} \frac{\frac{8}{15} \sqrt{\pi} a^{7/2} e^{-a} \frac{\alpha_h}{2q^2} \langle p_I \rangle}{\langle D \rangle - \frac{\alpha_c}{2q^2} - \frac{\alpha_h}{2q^2} \langle p_I \rangle} & a > 0 \\ 0 & a < 0. \end{cases}$$

As pointed out in Sec. 3.3.a, the sign of $a^{1/2}$ depends on the sign of Ω_2 . Using the criterion described there, we must have $(a^{1/2})\Omega_2 > 0$. Since $\Omega_2 < 0$ without drift reversal and $\Omega_2 > 0$ when $\langle D \rangle - \frac{\alpha_c}{2q^2} < 0$, both of these cases with $a > 0$ result in $B_I < 0$.

There are then three different regimes to consider. First, we have the case without drift reversal. From the above discussions, $C > 0$; $\Omega_1, \Omega_2 < 0$; $\frac{\partial A_R}{\partial \Omega} < 0$, $A_I < 0$, $\frac{\partial B_R}{\partial \Omega} < 0$, and $B_I < 0$.

0 in this regime. From Eq. (4.51) it can be shown that Ω is real if

$$C = A_I B_I \left[1 + \frac{(\Omega_1 - \Omega_2)^2}{\left(\frac{A_I}{\partial A_R / \partial \Omega} + \frac{B_I}{\partial B_R / \partial \Omega} \right)^2} \right]. \quad (4.57)$$

Smaller values of C yield stability; that is, in the limit $C \rightarrow 0$, $A(\Omega)$ and $B(\Omega)$ decouple, and we get two damped roots [see Eq. (4.51)]. This is the regime relevant to the deeply-trapped calculations presented in Sec. 4.3. $\frac{\partial A_R}{\partial \Omega}$ and $\frac{\partial B_R}{\partial \Omega}$ represent, respectively, positive and negative energy waves here (the wave energy is actually related to $\Omega_1 \frac{\partial A_R}{\partial \Omega}$ and $\Omega_2 \frac{\partial B_R}{\partial \Omega}$). Similarly, A_I and B_I correspond to positive and negative dissipation, respectively. The primary destabilization mechanism operating at large α_h is that the negative energy precessional mode is being driven unstable by the positive dissipation while the stabilizing influence of the negative dissipation provides a marginally stable point at a smaller, nonzero value of α_h [e.g., curve (iv) in Fig. 4.15]. Presumably, Eq. (4.57) is satisfied at this marginal point.

In the second regime, drift reversal is reached by using the energetic particle diamagnetism; that is, $\langle D \rangle - \frac{\alpha_c}{2q^2} - \frac{\alpha_h}{2q^2} \langle p_{\perp} \rangle < 0$, but $\langle D \rangle - \frac{\alpha_c}{2q^2} > 0$. All quantities have the same sign as in the first regime, except $B_I = 0$. Marginal stability is obtained in this

case only when $C = 0$. We still have the negative energy precessional mode being destabilized by its interaction with the positive energy wave and the positive dissipation, but the stabilizing influence of the negative dissipation is gone. Thus, we always have instability in this regime as long as there is finite coupling ($C \neq 0$) between A and B. This result is familiar from mirror theory.¹¹⁰

Finally, in the third regime, drift reversal is reached without the energetic particle diamagnetism, so that $\langle D \rangle - \frac{\alpha_c}{2q^2} < 0$, and consequently $\langle D \rangle - \frac{\alpha_c}{2q^2} - \frac{\alpha_h}{2q^2} \langle p_{\perp} \rangle < 0$. As discussed above, the signs of the various terms in Eq. (4.51) are now: $C > 0$; $\Omega_1, \Omega_2 > 0$; $\frac{\partial A_R}{\partial \Omega} > 0$, $A_I > 0$, $\frac{\partial B_R}{\partial \Omega} < 0$, and $B_I < 0$. The system is completely stable in this regime. To see this, consider the "worst case" of $\Omega_1 = \Omega_2$ [e.g., this assumption yields the most stringent requirements on C in Eq. (4.57)]. From Eq. (4.51), we find

$$\Omega - \Omega_2 = \frac{-i}{2} \left(\frac{A_I}{\partial A_R / \partial \Omega} + \frac{B_I}{\partial B_R / \partial \Omega} \right) \pm \frac{1}{2} \left[- \left(\frac{A_I}{\partial A_R / \partial \Omega} - \frac{B_I}{\partial B_R / \partial \Omega} \right)^2 - \frac{4C}{(\partial A_R / \partial \Omega)(\partial B_R / \partial \Omega)} \right]^{1/2}. \quad (4.58)$$

In the limit $C = 0$, we get two damped roots,

$$\Omega - \Omega_2 = \frac{-iA_I}{\partial A_R / \partial \Omega} \quad \text{and} \quad \Omega - \Omega_2 = \frac{-iB_I}{\partial B_R / \partial \Omega}$$

So, if we consider the even worse case in which $A_I = B_I = 0$, Eq. (4.58) reduces to

$$\Omega - \Omega_2 = \pm \left[\frac{-C}{(\partial A_R / \partial \Omega)(\partial B_R / \partial \Omega)} \right]^{1/2} \quad (4.59)$$

Since $\frac{\partial A_R}{\partial \Omega} \frac{\partial B_R}{\partial \Omega} < 0$ in this regime, Ω is real. Note that using $B_I = 0$ is somewhat appropriate since $B_I = 0$ as we cross from the second regime into this one. The most important effect here is that $\Omega_2 \frac{\partial B_R}{\partial \Omega}$ has changed sign relative to what it was in the other two cases while the sign of $\Omega_1 \frac{\partial A_R}{\partial \Omega}$ has remained the same. This indicates that the precessional mode has changed to a positive energy wave; likewise, its associated dissipation (still a stabilizing influence) has also become positive in character. Thus, we now have two positive energy waves coupled together, and we expect the system to be stable. Again, similar results have been obtained for mirror geometries.¹¹⁹

It appears that the sloshing ion distribution must be arranged so that $\langle D \rangle - \frac{\alpha_c}{2q^2} < 0$ in order for the precessional mode to be stable. While this may be the case for some range of pitch angles in each of the two sloshing distributions, Eqs. (4.34) and

(4.36), it is not true for all pitch angles. One important shortcoming of this analytic treatment is that the behavior at only one pitch angle λ_* is accounted for; however, the numerical calculations include contributions from all allowed pitch angles. Some of these contributions may yield instability when subjected to the criteria described here. As is clear from Eq. (4.2b), the relative weightings of the various pitch angles can be affected by the form of the eigenfunction. The plot of $\delta Q(\vartheta)$ shown in Fig. 4.16 indicates an emphasis on pitch angles having turning points near $\vartheta=0$. Since these pitch angles would most likely fall into the first regime discussed above, the existence of instability in that case is consistent with these results. If we could remove all of the energetic particles leading to instability, we might be able to eliminate the precessional mode. However, this implies very low energetic particle pressure at $\vartheta=0$ relative to the peak values. If we are to stabilize the MHD ballooning mode, this pressure must be significant (as demonstrated in Sec. 4.3).

Part of the problem here is that there is only a very short distance along the field line in which $D(\vartheta) < 0$ (see Fig. 4.14); the geodesic curvature contribution ($\sim S\vartheta\sin\vartheta$) keeps $D(\vartheta)$ from vanishing except near $\vartheta=\pi$ where $\sin\vartheta = 0$. If $D(\vartheta)$ included contributions from only the normal curvature, it might be possible to arrange for the fraction of pitch angles in a sloshing ion distribution corresponding to instability to be quite small and

still maintain sufficient pressure at $\psi=0$ to stabilize the MHD ballooning mode. With the geodesic curvature included, sloshing distributions of the type described in Sec. 4.4.b are such that most of the pitch angles in the system fall into the second regime in which the precessional mode is unstable. Thus, at least as far as the tokamak is concerned, the introduction of sloshing particles only removes a stabilizing influence: the negative dissipation.

It is apparent that the increased growth rates for larger values of ψ_0 (Fig. 4.13) provide evidence for this transition from the first regime where marginal stability is possible (e.g., $\psi_0 = 0.785$) to the second in which one always finds instability (e.g., $\psi_0 \geq 1.57$). The loss or reduction in negative dissipation associated with such a transition is precisely the effect produced by reducing $\langle \omega_d \rangle$. The drop in $\langle \omega_d \rangle$ as ψ_0 increases was shown in Sec. 4.4.b to be directly related to the higher growth rates in Fig. 4.13.

4.4.e Analytic Results: $k = 1/2$ Continuum Instability

We can apply the same procedures employed in obtaining Eq. (4.44) from Eqs. (4.17a) and (4.17b) to Eqs. (4.41a) and (4.41b) to find

$$\frac{d^2\phi}{d\vartheta^2} + \frac{\omega^2}{\omega_A^2}\phi = \frac{\alpha_h}{2} \frac{\sin\vartheta p_{\perp,t}(\vartheta) \langle\phi\sin\vartheta\rangle H}{\langle D \rangle - \frac{\alpha_c}{2q^2} - \frac{\alpha_h}{2q^2}[\langle p_{\perp,p} \rangle + \langle p_{\perp,t} \rangle(1-H)]}. \quad (4.60)$$

We have split $p_{\perp}(\vartheta)$ into contributions from trapped ($p_{\perp,t}$) and passing ($p_{\perp,p}$) particles so that $p_{\perp} = p_{\perp,p} + p_{\perp,t}$. Of course when considering distributions such as Eq. (4.34), $p_{\perp,p}=0$. Here, we want to examine more closely the $k = 1/2$ solution to this equation, found to be unstable with the circulating - trapped distribution Eq. (4.36).

This instability is primarily a result of having $p_{\perp,p}$, $p_{\perp,t}$, $p_{\perp} \gg 1$ on the inside edge of the tokamak. Such a high level of anisotropy is necessary in a distribution containing trapped particles with turning points near $\vartheta=\pi$. Since $a = -\frac{\omega}{\omega_{d0}} \langle \lambda(D - \frac{\alpha_c}{2q^2} - \frac{\alpha_h}{2q^2} p_{\perp}) \rangle^{-1}$, we expect $a \ll 1$ and $H(a) \approx 1$ when $\alpha_h \sim 1$; in effect, $|\omega/\omega_d| \ll 1$, as in EBT theory. Were it not for the $\frac{\alpha_h}{2q^2} \langle p_{\perp,p} \rangle$ term in the denominator of Eq. (4.60), we could analyze these equations in a manner similar to that used in EBT theory (see Sec. 3.2). But with $H=1$ in Eq. (4.60), the large negative contribution made by $\frac{\alpha_h}{2q^2} \langle p_{\perp,p} \rangle$ to the denominator implies that the right-hand side will be less than zero (i.e., destabilizing). Because of the factor $\alpha_h p_{\perp,t}(\vartheta)$ in the numerator, this right-hand side is not necessarily small even if $\alpha_h \langle p_{\perp,p} \rangle \gg 1$. Thus, we

should find instability as long as ϕ does not vary so rapidly that $d^2\phi/d\vartheta^2$ is large.

We can solve Eq. (4.60) approximately by assuming that $p_{\perp,t}$ consists of delta functions at some angle ϑ_p ,

$$p_{\perp,t}(\vartheta) \approx p_t [\delta(\vartheta + \vartheta_p) + \delta(\vartheta - \vartheta_p)].$$

We choose p_t so that this function has the same average as the one used in the numerical calculations,

$$p_t = \int_0^\pi d\vartheta p_{\perp,t}(\vartheta).$$

Integrating Eq. (4.60) with initial conditions $\phi(-\pi) = 0$, $\frac{d\phi}{d\vartheta}(-\pi) = 1$, we find

$$\phi(\vartheta) = \phi_0(\vartheta) + \Lambda \phi_1(\vartheta), \quad (4.61)$$

where

$$\phi_0(\vartheta) = \frac{\sin[\Omega(\vartheta + \pi)]}{\Omega},$$

$$\phi_1(\vartheta) = \frac{p_t \sin\vartheta_p}{\Omega} \{ \sin[\Omega(\vartheta - \vartheta_p)] H_0(\vartheta - \vartheta_p) - \sin[\Omega(\vartheta + \vartheta_p)] H_0(\vartheta + \vartheta_p) \},$$

$$\Lambda = \frac{A \langle \phi_0 \sin\vartheta \rangle}{1 - A \langle \phi_1 \sin\vartheta \rangle},$$

$$A = \frac{\alpha_h}{2} \frac{H}{\left[\langle D \rangle - \frac{\alpha_c}{2q^2} - \frac{\alpha_h}{2q^2} \langle p_{\perp, p} \rangle - \frac{\alpha_h}{2q^2} \langle p_{\perp, t} \rangle (1-H) \right]}$$

and H_0 is the Heaviside function,

$$H_0(x) = \begin{cases} 0 & x < 0 \\ 1 & x > 0. \end{cases}$$

To get a dispersion relation for $k = 1/2$, we need only set $\frac{d\phi}{d\vartheta}(\pi) = -1$ [see Eq. (4.26)], so that Ω is given by

$$\cos^2 \pi \Omega + \Lambda p_t \sin \vartheta_p \sin \pi \Omega \sin \Omega \vartheta_p = 0. \quad (4.62)$$

In computing a bounce average of some function $f(\vartheta)$, the value of the function at the turning point ϑ_T receives heavy weighting due to the $1/|v_{\parallel}|$ factor. We can then get an estimate for Λ if we approximate $\langle f \rangle \approx f(\vartheta_T)$. Since $\lambda_* \approx 1$ for a sloshing distribution, the corresponding turning point is near ϑ_0 . But, $\vartheta_0 \equiv \pi$ for the case we are considering; so $\vartheta_T \approx \vartheta_0 \equiv \pi$. Likewise, the fact that the pressure function $p_{\perp, t}$ peaks near $\vartheta = \pi$ implies that we should select $\vartheta_p \approx \pi$. We can then reasonably set $\vartheta_T \approx \vartheta_p \approx \pi$ and $\langle f \rangle \approx f(\vartheta_p)$ in Eq. (4.62) to obtain

$$\Omega \cot \pi \Omega = - A p_t \sin^2 \vartheta_p. \quad (4.63)$$

When the right-hand side of Eq. (4.63) is less than $1/\pi$, the field-line bending term in Eq. (4.60) dominates the energetic particle contribution, and Ω is real. If it is larger than $1/\pi$, unstable solutions can be found. As mentioned previously, when $\alpha_h \sim 1$ we can assume $|\alpha_h \langle p_{\perp,p} \rangle| > |2q^2 \langle D \rangle - \alpha_c|$ and $H(a) \approx 1$. When we look for purely imaginary solutions with $\pi \operatorname{Im} \Omega > 1$, we see that

$$\gamma = \operatorname{Im} \Omega \cong \left(\frac{\int_0^\pi d\vartheta p_{\perp,t}(\vartheta)}{\langle p_{\perp,p} \rangle} \right) q^2 \sin^2 \vartheta_p.$$

For the parameters we have been using here, $\gamma \approx 0.6$, on the order of MHD growth rates as was found through the numerical calculations.

We now examine the behavior of this mode at small α_h . Recall that in Sec. 4.4.c no nonzero threshold α_h was found numerically. It appears from Eq. (4.63) that a sufficient condition for stability is that $A > 0$. With $H=1$, this implies that the approximate threshold for α_h would be such that

$$\langle D \rangle - \frac{\alpha_c}{2q^2} - \frac{\alpha_h}{2q^2} \langle p_{\perp,p} \rangle = 0. \quad (4.64)$$

Implicit in this result is the assumption that $\Omega \rightarrow 0$ at marginal stability. However, with $k = 1/2$ and $\alpha_h = 0$ in Eq. (4.60), we must have $\Omega = \pm 1/2$. Furthermore, if Eq. (4.64) is nearly satisfied, $\langle \omega_d \rangle$ should not be very large. As a result, we cannot assume $\omega / \langle \omega_d \rangle \ll 1$ and $H=1$ near marginal stability.

To demonstrate that removal of this assumption leads to instability for any small but nonzero α_h , we expand the mode frequency about $\Omega = -1/2$:

$$\Omega = -1/2 + \delta\Omega,$$

where $|\delta\Omega| \ll 1/2$, and we determine the sign of $\text{Im } \delta\Omega$. We take as our dispersion relation

$$F(\Omega) = 0 \cong F(\Omega = -1/2) + \delta\Omega \frac{dF}{d\Omega}(\Omega = -1/2).$$

Calculating $\frac{dF}{d\Omega}$ and solving for $\delta\Omega$, we find

$$\delta\Omega = \frac{-q^2 \alpha_h p_t \sin^2 \psi_p H [\text{Den}]}{\frac{\pi}{2} [\text{Den}]^2 - 2q^4 \alpha_h p_t \sin^2 \psi_p \frac{\omega_A}{\omega_{d0}} \left[H \left(\frac{7}{2a} - 1 \right) - \frac{7}{2a} \right]}, \quad (4.65)$$

with

$$[\text{Den}] \equiv 2q^2 \langle D \rangle - \alpha_c - \alpha_h \langle p_{\perp,p} \rangle - \alpha_h \langle p_{\perp,t} \rangle (1 - H).$$

In the limit $\alpha_h \rightarrow 0$, Eq. (4.57) becomes

$$\delta\Omega \cong - \frac{\alpha_h p_t \sin^2 \theta_p H}{\pi \left(\langle D \rangle - \frac{\alpha_c}{2q^2} \right)} \quad (4.66)$$

If $\omega_* \langle \omega_d \rangle > 0$ (as would be the case for small α_h) and $a = \omega / \langle \omega_d \rangle > 0$,

$$\text{Im } H = - \frac{8}{15} \sqrt{\pi} |a^{7/2}| e^{-a} < 0.$$

Thus, $\text{Im } \delta\Omega > 0$, and we have instability. Note that by lowering α_h we increase the fraction of resonant particles. If $\langle D \rangle - \frac{\alpha_c}{2q^2} \approx 0$, this analysis breaks down. Furthermore when $\langle D \rangle - \frac{\alpha_c}{2q^2} < 0$, $\omega_* \langle \omega_d \rangle < 0$ even if $\alpha_h = 0$; consequently, $a < 0$ and $\text{Im } H = 0$, implying that $\delta\Omega$ is real. As was discussed above, $\langle D \rangle - \frac{\alpha_c}{2q^2} < 0$ only if λ_* is very close to unity for $S = 0.6$ and $\alpha_c = 0.8$. Again, the numerical calculations also include contributions from larger pitch angles. For these pitch angles, $\langle D \rangle - \frac{\alpha_c}{2q^2} > 0$; the resulting imaginary part of the kinetic integral leads to the nonzero growth rate noted in Fig. 4.18. Thus, the resonant particles of the sloshing distribution, Eq. (4.36), prevent us from stabilizing the $k = 1/2$

mode, as was the case with the $k=0$ mode when the purely-trapped distribution, Eq. (4.34), was employed. For this reason, it would not be surprising to find that the $k=0$ mode is just as unstable as the $k = 1/2$ mode for these small values of α_h .

4.4.f Conclusions

In this section we have considered a distribution function in which most of the energetic particles are barely trapped. The numerical calculations carried out here suggest several problems with using energetic sloshing ions to eliminate resonant particle destabilization of ballooning modes. Computations made with a distribution containing only trapped particles point out that the requirement $\tau > 0$ necessary to avoid mirror-mode instability and to prevent numerical problems sets a lower limit on the width of the distribution in pitch angle space. The numerical results in this case indicate that the sloshing ions do not have a strong stabilizing effect on the high-frequency ($\omega \sim \langle \omega_d \rangle$) branch of solutions to the ballooning mode equations. It is also noted that at large energetic particle pressures the boundary conditions of outgoing waves and spatially damped waves at infinity are no longer consistent. Investigations of the ballooning mode equations in the $S \rightarrow \infty$ limit point to a continuum instability as the source of this problem. The instability results from the destabilization of shear

Alfvén waves by the negative dissipation due to resonant particles in the distribution.

By employing a distribution containing both circulating and trapped energetic particles, the restrictions imposed to keep $\tau > 0$ can be relaxed significantly. In this case, the turning points of the trapped particles can be concentrated on the inside edge of the tokamak sufficiently well to eliminate almost all of the resonant particles so that the continuum solutions are nearly stable. However, another branch of continuum solutions is predicted to be unstable as a result of the presence of a large energetic particle pressure peak in the good curvature region. This instability has been examined analytically and found to have a growth rate on the order of MHD time scales. Furthermore, it is unstable for all nonzero values of the energetic particle pressure gradient. Thus, it appears that at least one of the two branches of the continuum solutions is always unstable for a sloshing distribution in the high-bounce-frequency regime. As long as this is true, an unstable solution can be found to the ballooning mode equations.

Analytic calculations examining the high-frequency, precessional mode show that changing the sign of $\langle \omega_d \rangle$ (i.e., so that $\omega_* \langle \omega_d \rangle < 0$) through diamagnetic effects does not provide stability since doing so removes the one stabilizing influence in the system: the negative dissipation arising out of the drift resonance. The overall increases in the growth rate as ν_0 is

raised for $\Delta\lambda \gg 1$ (Fig. 4.13) are explained as arising from a drop in $\langle\omega_d\rangle$; such a result is consistent with losing a stabilizing effect when $\langle\omega_d\rangle$ changes sign. The stabilizing effect of the sloshing particles appears only if $\omega_*\langle\omega_d\rangle < 0$ when the energetic particle diamagnetic contribution to $\langle\omega_d\rangle$ is not included. In the tokamak geometry this is a much more stringent condition than in a simple mirror due to the presence of the (unfavorable) geodesic curvature in $\langle\omega_d\rangle$. Attempts to satisfy it would most likely lead to destabilization of the MHD ballooning branch or would fail as a result of the eigenfunction peaking in such a way that the effects of remnant unstable particles in the system are heavily weighted.

These several problems: the limitations imposed to keep $\tau > 0$, the continuum instabilities, and the difficulty of achieving $\omega_*\langle\omega_d\rangle < 0$ without the energetic particle diamagnetic contribution, in addition to the larger volume of hot plasma required for a sloshing distribution, lead us to conclude that sloshing energetic particles would be less effective in bridging the unstable gap to second stability than a deeply-trapped distribution of the same energy.

Possible future work includes treating the low-bounce-frequency limit that may be relevant in some cases of interest. For the distribution containing trapped and circulating particles, this could give significantly different results since the entire distribution appears in the kinetic term. Finally, as was

mentioned in Sec. 4.3.d, additional physical effects such as those of finite Larmor radius and banana widths (especially here with the larger parallel velocities) could have a significant stabilizing effect and should be taken into account.

CHAPTER V

CONCLUSIONS

In this dissertation we have considered the effect of energetic particles on the stability of ballooning and other curvature-driven modes in both mirror and tokamak plasmas. We have also included investigations of how the negative energy precessional mode associated with the high temperature species (defined by having magnetic drift frequencies much greater than typical MHD growth rates) can be destabilized. For the tokamak configuration in particular, such instabilities limit the effectiveness of using energetic particles to stabilize the ballooning mode driven by the main, core plasma pressure gradient.

As an introduction to the beneficial aspects of energetic particles, a numerical simulation of the midplane of an EBT mirror cell was carried out. An MHD particle code was used to do the simulation, and the hot electrons were modeled by a fixed, embedded current ring. One of the advantages of this approach to the problem is that considerably less computational effort is required than with a full-dynamics code. The stabilizing effect of the hot electron ring on the interchange mode driven by the product of the

MHD particle pressure gradient and radial gravity is quite clear. However, a linear analysis suggests that the critical level of current to achieve stability is a function of radius in the axisymmetric mirror. The result is that the system may still be unstable in the outer regions of the simulation box, although the majority of the particles can be effectively confined. Future work along these lines involves including interactions between the hot electrons and the MHD particles in order to observe the hot electron or interacting interchange instabilities and is currently underway.

The second part of the dissertation also considered hot electrons in EBT. Appropriate linear equations were presented for the system and were solved analytically under the assumption $\omega \ll \omega_{dh}$ in a manner introduced previously.^{34,66} The new work discussed here concerns the numerical solution of the equation describing the magnetic compressional mode. For typical EBT-S parameters,²⁵ instability is predicted for all pressure scale lengths just below those needed for drift reversal. If larger core densities are present, a wave-particle resonance arises when the particle drifts are not reversed, causing instability up to much larger scale lengths. Recent experimental measurements indicate that the hot electron ring widths are not narrow enough to bring about drift reversal, as was once thought. It is possible that the nonlinear

properties of this mode are causing the observed radial spreading of what would otherwise be a sharp hot electron ring profile.

A similar approach to a numerical solution of the two coupled equations that describe the interchange and magnetic compressional modes in EBT was also discussed. It is found that very little error is made in using a single equation for the perturbed parallel magnetic field in describing the magnetic compressional mode. The inclusion of the field line dependence of equilibrium quantities, as is accomplished by numerical solution of the coupled equations, reduces the amount of hot electron pressure needed to stabilize the background pressure-driven interchange relative to local estimates. Likewise, investigation of the interacting pressure-driven interchange shows that the full equations predict a lower value for the growth rate than do local estimates. In this case, however, the simple stability criterion, $\beta_c < 2\Delta_r/R$, remains fairly accurate.

In the third and final part of this dissertation, we examined the prospects for using energetic particles to reach the second stability region for ballooning modes in tokamaks. After adopting an appropriate model for energetic particles deeply trapped on the outside edge of the tokamak, the ballooning mode equations were solved numerically; our efforts were focused on the low frequency ($\text{Re } \omega \ll \omega_{dh}$) MHD and high frequency ($\text{Re } \omega \lesssim \omega_{dh}$) precessional branches. If the energetic particle temperature is

large enough (of order 1 MeV), there is a range of values for the energetic particle pressure gradient inside which both of these modes are stable, and a path to second stability is opened. However, even if means of introducing such particles into the system are found, and this state is achieved, other instabilities arise when the negative energy precessional mode couples to other positive energy waves or sources of positive dissipation. The discrete eigenmodes set up by the toroidal coupling of neighboring poloidal harmonics in the shear Alfvén spectrum¹⁰² are destabilized in this manner.

In an attempt to remove the resonant destabilization of the precessional branch and thereby lower the requirements on the energetic particle temperature, a sloshing ion distribution was considered. Numerical calculations do not indicate a significant stabilizing effect on the precessional mode when a large percentage of the trapped particle turning points are placed in the good curvature region. To do as well as a deeply-trapped distribution with the same midplane pressure gradient, we require a distribution too narrow to be easily maintained or to allow the system to be mirror-mode stable ($\tau > 0$).^{45,68} In addition, the presence of a continuum instability is predicted by an examination of the ballooning mode equation in the limit $S\beta \rightarrow \infty$. When the energetic species is completely trapped, the restrictions imposed on the distribution to keep $\tau > 0$ imply that a significant number of

resonant particles ($\omega_* \langle \omega_d \rangle > 0$) are present in the system. The instability results from the destabilization of shear Alfvén waves by the negative dissipation due to these particles. For a distribution containing both circulating and trapped energetic particles, the restrictions imposed to keep $\tau > 0$ can be relaxed so that the fraction of resonant particles becomes quite small. However, in this case another branch of continuum solutions is predicted to be unstable as a result of the presence of a large energetic particle pressure peak in the good curvature region. Analytic calculations examining the high-frequency, precessional mode show that changing the sign of $\langle \omega_d \rangle$ relative to ω_* by the diamagnetic effects of the energetic species does not provide stability since doing so removes the one stabilizing influence in the problem: the negative dissipation arising out of the drift resonance. The stabilizing effect of the sloshing distribution can appear only if this change in sign of $\langle \omega_d \rangle$ is achieved without the diamagnetic contribution of the energetic particle pressure. Due to the presence of geodesic curvature in this problem, this is a much more stringent requirement than in a simple mirror geometry. These results lead us to conclude that sloshing energetic particles would be less effective in reaching second-stability than a deeply-trapped distribution of the same energy.

Future work on the effects of energetic particles on tokamak stability should consider finite Larmor radius and banana width effects. There is also a need for information about the nonlinear behavior of the drift resonant precessional instabilities. It may be that they do not give rise to a significant loss of confinement, although it is quite clear that interaction of the precessional mode with the internal kink leads to expulsion of trapped energetic ions (i.e., fishbone oscillations).

REFERENCES

1. G. Bateman, MHD Instabilities (MIT Press, Cambridge, 1978).
2. R. A. Gross, Fusion Energy (John Wiley & Sons, New York, 1984).
3. L. Spitzer, Physics of Fully Ionized Gases (John Wiley (Interscience), New York, 1962).
4. M. N. Rosenbluth and C. L. Longmire, *Ann. Phys.* 1, 120 (1957).
5. J. M. Greene and J. L. Johnson, *Plasma Phys.* 10, 729 (1968).
6. D. B. Nelson and C. L. Hedrick, *Nucl. Fusion* 19, 238 (1979).
7. J. P. Freidberg, *Rev. Mod. Phys.* 54, 801 (1982).
8. J. W. Connor, R. J. Hastie, and J. B. Taylor, *Proc. R. Soc. London, Ser. A*365, 1 (1979).
9. J. W. Connor, R. J. Hastie, and J. B. Taylor, *Phys. Rev. Lett.* 40, 396 (1978).
10. A. M. M. Todd, M. S. Chance, J. M. Greene, R. C. Grimm, J. L. Johnson, and J. Manickam, *Phys. Rev. Lett.* 38, 826 (1977).
11. D. Lortz and J. Nuhrenberg, *Phys. Lett.* 68A, 49 (1978).
12. D. Lortz and J. Nuhrenberg, *Nucl. Fusion* 19, 1207 (1979).
13. B. Coppi, A. Ferreira, J. W.-K. Mark, and J. J. Ramos, *Nucl. Fusion* 19, 715 (1979).
14. D. Dobrott, D. B. Nelson, J. M. Greene, A. H. Glasser, M. S. Chance, and E. A. Frieman, *Phys. Rev. Lett.* 39, 943 (1977).
15. B. Coppi, *Phys. Rev. Lett.* 39, 939 (1977).
16. J. M. Greene and M. S. Chance, *Nucl. Fusion* 21, 453 (1981).

17. B. Coppi, A. Ferreira, and J. J. Ramos, Phys. Rev. Lett. 44, 990 (1980).
18. C. Mercier, in Plasma Physics and Controlled Nuclear Fusion Research (International Atomic Energy Agency, Vienna, 1979), Vol. I, p. 701.
19. H. R. Strauss, W. Park, D. A. Monticello, R. B. White, S. C. Jardin, M. S. Chance, A. M. M. Todd, and A. H. Glasser, Nucl. Fusion 20, 638 (1980).
20. N. C. Christofilis, in Proceedings of the Second United Nations International Conference on the Peaceful Uses of Atomic Energy (United Nations, Geneva, Switzerland, 1958), Vol. 32, p. 279.
21. R. N. Sudan and E. Ott, Phys. Rev. Lett. 33, 355 (1974).
22. H. H. Fleischmann, Ann. N.Y. Acad. Sci. 251, 472 (1975).
23. R. A. Dandl, H. O. Eason, P. H. Edmonds, and A. C. England, Nucl. Fusion 11, 411 (1971).
24. N. A. Krall, Phys. Fluids 9, 820 (1966).
25. R. A. Dandl, H. O. Eason, G. E. Guest, C. L. Hedrick, H. Ikegami, and D. B. Nelson, in Proceedings of Plasma Physics and Controlled Fusion Research (International Atomic Energy Agency, Vienna, 1975), Vol. II, p. 141.
26. R. R. Dominguez and H. L. Berk, Phys. Fluids 21, 827 (1978).
27. H. Ikegami, H. Ikezi, M. Hosokawa, S. Tanaka, and K. Takayama, Phys. Rev. Lett. 19, 779 (1967).
28. M. Fujiwara, T. Kamimura, M. Hosokawa, T. Shoji, H. Iguchi, H. Sanuki, K. Takosugi, F. Tsuboi, H. Tsuchidate, K. Kadota, K. Sato, K. Tsuchida, A. Tsushima, and H. Ikegami, in Proceedings of Plasma Physics and Controlled Fusion Research (International Atomic Energy Agency, Vienna, 1985), Vol. II, p. 551.
29. B. H. Quon, R. A. Dandl, W. DiVergilio, G. E. Guest, L. L. Lao, N. H. Lazar, T. K. Samec, and R. F. Wuerker, Phys. Fluids 28, 1503 (1985).

30. R. S. Post, M. Gerver, J. Kesner, J. H. Irby, B. G. Lane, M. E. Mauel, B. D. McVey, A. Ram, E. Sevillano, D. L. Smatlak, D. K. Smith, J. D. Sullivan, J. Trulsen, A. Bers, J. W. Coleman, M. P. J. Gaudreau, R. E. Klinkowstein, R. P. Torti, X. Chen, R. C. Garner, D. L. Goodman, P. Goodrich, and S. A. Hokin, in Proceedings of Plasma Physics and Controlled Fusion Research (International Atomic Energy Agency, Vienna, 1985), Vol. II, p. 285.
31. D. L. Hillis, J. B. Wilgen, J. A. Cobble, W. A. Davis, S. Hiroe, D. A. Rasmussen, R. K. Richards, T. Uckan, E. F. Jaeger, O. E. Hankins, J. R. Goyer, and L. Solenstein, Phys. Fluids 28, 2848 (1985).
32. D. L. Hillis, J. B. Wilgen, T. S. Bigelow, E. F. Jaeger, D. W. Swain, O. E. Hankins, and R. E. Juhala, submitted to Phys. Fluids.
33. M. N. Rosenbluth, N. A. Krall, and N. Rostoker, Nucl. Fusion, Suppl. Part 1, 143 (1962).
34. H. L. Berk, C. Z. Cheng, M. N. Rosenbluth, and J. W. Van Dam, Phys. Fluids 26, 2642 (1983).
35. Y. Ohsawa and J. M. Dawson, Phys. Fluids 27, 1491 (1984).
36. H. L. Berk, J. W. Van Dam, M. N. Rosenbluth, and D. A. Spong, Phys. Fluids 26, 201 (1983).
37. H. Sanuki and F. F. Chen, Phys. Fluids 28, 3567 (1985).
38. A. M. El Nadi, Phys. Fluids 25, 2019 (1982).
39. M. N. Rosenbluth, S. T. Tsai, J. W. Van Dam, and M. G. Engquist, Phys. Rev. Lett. 51, 1967 (1983).
40. J. M. Greene and B. Coppi, Phys. Fluids 8, 1745 (1965).
41. H. P. Furth, Phys. Fluids 8, 2020 (1965).
42. H. L. Berk and R. N. Sudan, J. Plasma Physics 6, 413 (1971).
43. T. M. Antonsen, Jr. and Y. C. Lee, in Proceedings of Hot Electron Workshop (Oak Ridge National Lab, Oak Ridge, 1981), Conf. 811203, p. 191.

44. M. N. Rosenbluth, J. W. Van Dam, and Y. C. Lee, *Phys. Fluids* 25, 1349 (1982).
45. T. M. Antonsen and Y. C. Lee, *Phys. Fluids* 25, 132 (1982).
46. K. T. Tsang, X. S. Lee, B. Hafizi, and T. M. Antonsen, Jr., *Phys. Fluids* 27, 2511 (1984).
47. D. E. Baldwin and H. L. Berk, *Phys. Fluids* 26, 3595 (1983).
48. H. L. Berk and T. B. Kaiser, *Phys. Fluids* 28, 345 (1985).
49. H. L. Berk and H. V. Wong, *Phys. Fluids* 28, 1881 (1985).
50. H. L. Berk, J. W. Van Dam, and D. A. Spong, *Phys. Fluids* 26, 606 (1983).
51. F. Brunel, J. N. Lebeouf, T. Tajima, J. M. Dawson, M. Makino, and T. Kamimura, *J. Comput. Phys.* 43, 268 (1981).
52. F. Brunel, J. N. Lebeouf, D. P. Stotler, H. L. Berk, and S. M. Mahajan, in Algorithms, Architectures and the Future of Scientific Computation, edited by F. A. Matsen and T. Tajima (University of Texas Press, Austin, 1986), p.60.
53. D. B. Nelson, *Phys. Fluids* 23, 1850 (1980).
54. J. W. Van Dam and Y. C. Lee, in Proceedings of EBT Ring Workshop (Oak Ridge National Lab, Oak Ridge, 1979), Conf. 791288, p. 471.
55. R. L. Morse, in Method of Computational Physics, eds. B. Adler, et al. (Academic Press, New York, 1970), Vol. 9, p. 213.
56. D. E. Potter, Computational Physics (Academic Press, New York, 1973).
57. R. J. Colchin, T. Uckan, F. W. Baity, L. A. Berry, F. M. Bieniosek, L. Bighel, W. A. Davis, E. Dullni, H. O. Eason, J. C. Glowienka, G. A. Hallock, G. R. Hasté, D. L. Hillis, A. Komori, T. L. Owens, R. K. Richards, L. Solensen, T. L. White, and J. B. Wilgen, *Plasma Phys.* 25, 597 (1983).
58. H. L. Berk, *Phys. Fluids* 19, 1255 (1976).

59. M. N. Rosenbluth, Phys. Rev. Lett. 46, 1525 (1981).
60. D. P. Stotler, H. L. Berk, and M. G. Engquist, Phys. Fluids 29, 1149 (1986).
61. J. H. Hammer and H. L. Berk, Phys. Fluids 28, 2442 (1985).
62. T. M. Antonsen, Jr., Y. C. Lee, H. L. Berk, M. N. Rosenbluth, and J. W. Van Dam, Phys. Fluids 26, 3580 (1983).
63. X. S. Lee and P. J. Catto, Phys. Fluids 24, 2010 (1983).
64. D. A. Spong, H. L. Berk, J. W. Van Dam, and M. N. Rosenbluth, Phys. Fluids 26, 2652 (1983).
65. K. T. Nguyen and T. Kammash, Phys. Fluids 26, 3085 (1983).
66. H. Abe, H. L. Berk, C. Z. Cheng, M. N. Rosenbluth, J. W. Van Dam, D. A. Spong, N. A. Uckan, T. M. Antonsen, Y. C. Lee, K. T. Tsang, P. J. Catto, X. S. Lee, K. T. Nguyen, and T. Kammash, in Proceedings of Plasma Physics and Controlled Fusion Research (International Atomic Energy Agency, Vienna, 1983), Vol. III, p. 427.
67. P. J. Catto, R. J. Hastie, and J. W. Connor, Plasma Phys. Controlled Fusion 27, 307 (1985).
68. D. M. Kruskal and C. Oberman, Phys. Fluids 1, 275 (1958).
69. J. W. Connor, R. J. Hastie, T. J. Martin, and M. F. Turner, in Heating in Toroidal Plasmas (Commission of the European Communities, Brussels, 1982), Vol. I, p. 65.
70. B. D. Fried and S. D. Conte, The Plasma Dispersion Function (Academic, New York, 1961).
71. E. F. Jaeger, L. A. Berry, C. L. Hedrick, and R. K. Richards, Nucl. Fusion 25, 71 (1985).
72. S. Hiroe, J. B. Wilgen, F. W. Baity, L. A. Berry, R. J. Colchin, W. A. Davis, A. M. El Nadi, G. R. Haste, D. L. Hillis, D. A. Spong, T. Uckan, and T. L. Owens, Phys. Fluids 27, 1019 (1984).
73. K. T. Nguyen and T. Kammash, Phys. Fluids 27, 1483 (1984).

74. P. J. Fielding and F. A. Haas, *Phys. Rev. Lett.* 41, 801 (1978).
75. M. S. Chu, C. Chu, G. Guest, J. Y. Hsu, and T. Ohkawa, *Phys. Rev. Lett.* 41, 247 (1978).
76. M. Murakami, D. W. Swain, S. C. Bates, C. E. Bush, L. A. Charlton, J. L. Dunlap, G. R. Dyer, P. H. Edmonds, A. C. England, H. H. Haselton, J. T. Hogan, H. C. Howe, D. P. Hutchinson, R. C. Isler, T. C. Jernigan, S. Kasai, H. E. Ketterer, J. Kim, P. W. King, E. A. Lazarus, J. F. Lyon, C. H. Ma, J. T. Mihalcz, J. K. Munro, A. P. Navarro, G. H. Neilson, D. R. Overbey, V. K. Paré, M. J. Saltmarsh, S. D. Scott, J. Sheffield, J. E. Simpkins, W. L. Stirling, C. C. Tsai, R. M. Wieland, J. B. Wilgen, W. R. Wing, R. E. Worsham, and B. Zurro, in Proceedings of Plasma Physics and Controlled Fusion Research (International Atomic Energy Agency, Vienna, 1981), Vol. I, p. 377.
77. J. K. Munro, L. A. Charlton, D. J. Stickler, W. A. Cooper, J. T. Hogan, and D. W. Swain, *Nucl. Fusion* 22, 599 (1982).
78. W. M. Tang, J. W. Connor, and R. J. Hastie, *Nucl. Fusion* 20, 1439 (1980).
79. R. J. Hastie and K. W. Hesketh, *Nucl. Fusion* 21, 651 (1981).
80. K. T. Tsang, and D. J. Sigmar, *Nucl. Fusion* 21, 1227 (1981).
81. C. Z. Cheng, *Nucl. Fusion* 22, 773 (1982).
82. W. A. Cooper, *Phys. Fluids* 26, 1830 (1983).
83. M. Keilhacker, G. Fussmann, G. von Gierke, G. Janeschitz, M. Kornherr, K. Lackner, E. R. Muller, P. Smeulders, F. Wagner, G. Becker, K. Bernhardt, U. Ditte, A. Eberhagen, O. Gehre, J. Gernhardt, E. Glock, T. Grave, O. Gruber, G. Haas, M. Hesse, F. Karger, S. Kissel, O. Kluber, G. Lisitano, H. M. Mayer, K. McCormick, D. Meisel, V. Mertens, H. Murmann, H. Niedermeyer, W. Poschenrieder, H. Rapp, F. Ryter, F. Schneider, G. Siller, F. Soldner, E. Speth, A. Stabler, K.-H. Steuer, and O. Vollmer, in Proceedings of Plasma Physics and Controlled Fusion Research (International Atomic Energy Agency, Vienna, 1985), Vol. I, p. 71.
84. R. D. Stambaugh, R. W. Moore, L. C. Bernard, A. G. Kellman, E. J. Strait, L. Lao, D. O. Overskei, T. Angel, C. J. Armentrout, J. F. Baur, F. P. Blau, G. Bramson,

- N. H. Brooks, K. H. Burrell, R. W. Callis, R. P. Chase, A. P. Collerainé, G. Cottrell, J. C. DeBoo, S. Ejima, E. S. Fairbanks, J. Fasolo, C. H. Fox, J. R. Gilleland, R. Groebner, F. J. Helton, R. M. Hong, C. L. Hsieh, G. L. Jahns, C. L. Kahn, J. Kim, D. Knowles, J. K. Lee, P. Lee, A. J. Lieber, J. M. Lohr, D. B. McColl, C. H. Meyer, T. Ohkawa, N. Ohyabu, P. I. Petersen, T. W. Petrie, W. W. Pfeiffer, J. C. Phillips, L. C. Rottler, D. P. Schissel, J. T. Scoville, R. P. Seraydarian, B. W. Sleaford, J. R. Smith, R. T. Snider, R. D. Stav, H. St. John, R. E. Stockdale, J. F. Tooker, D. Vaslow, J. C. Wesley, S. S. Wojtowicz, S. K. Wong, and E. M. Zawadski, in Proceedings of Plasma Physics and Controlled Fusion Research (International Atomic Energy Agency, Vienna, 1985), Vol. I, p. 217.
85. F. Troyon, T. Gruber, H. Sauremann, S. Semenzato, and S. Succi, Plasma Phys. Controlled Fusion (11th European Conference, Aachen, European Physical Society) 26, 209 (1983).
86. A. Sykes, M. F. Turner, and S. Patel, in Controlled Fusion and Plasma Physics (11th European Conference, Aachen, European Physical Society, 1983), Vol. 7D, Part II, p. 363.
87. K. McGuire, R. Goldston, M. Bell, M. Bitter, K. Bol, K. Brau, D. Buchenauer, T. Crowley, S. Davis, F. Dylla, H. Eubank, H. Fishman, R. Fonck, B. Grek, R. Grimm, R. Hawryluk, H. Hsuan, R. Hulse, R. Izzo, R. Kaita, S. Kaye, H. Kugel, D. Johnson, J. Manickam, D. Manos, D. Mansfield, E. Mazzucato, R. McCann, D. McCune, D. Monticello, R. Motley, D. Mueller, K. Oasa, M. Okabayashi, K. Owens, W. Park, M. Reusch, N. Sauthoff, G. Schmidt, S. Sesnic, J. Strachan, C. Surko, R. Slusher, H. Takahashi, F. Tenney, P. Thomas, H. Towner, J. Valley, and R. White, Phys. Rev. Lett. 50, 891 (1983).
88. R. B. White, R. J. Goldston, K. McGuire, A. H. Boozer, D. A. Monticello, and W. Park, Phys. Fluids 26, 2958 (1983).
89. L. Chen, R. B. White, and M. N. Rosenbluth, Phys. Rev. Lett. 52, 1122 (1984).
90. R. B. White, L. Chen, F. Romanelli, and R. Hay, Phys. Fluids 28, 278 (1985).
91. L. Chen, R. B. White, C. Z. Cheng, F. Romanelli, J. Weiland, R. Hay, J. W. Van Dam, D. C. Barnes, M. N. Rosenbluth, and S. T. Tsai, in Proceedings of Plasma Physics and Controlled

- Fusion Research (International Atomic Energy Agency, Vienna, 1985), Vol. II, p. 59.
92. B. Coppi and F. Porcelli, Massachusetts Institute of Technology Report PTP-85/13 (1985).
 93. G. Rewoldt and W. M. Tang, Nucl. Fusion 24, 1573 (1984).
 94. J. Weiland and L. Chen, Phys. Fluids 28, 1359 (1985).
 95. D. A. Spong, D. J. Sigmar, W. A. Cooper, D. E. Hastings, and K. T. Tsang, Phys. Fluids 28, 2494 (1985).
 96. K. McGuire, D. Buchenauer, R. Izzo, J. Manickam, D. Monticello, K. Okano, W. Park, and N. Sauthoff, Bull. Am. Phys. Soc. 28, 1173 (1983).
 97. B. Coppi and F. Pegoraro, Comments Plasma Phys. Controlled Fusion 5, 131 (1979).
 98. K. T. Tsang, D. J. Sigmar, and J. C. Whitson, Phys. Fluids 24, 1508 (1981).
 99. J. Weiland, Physica Scripta 23, 801 (1981).
 100. D. A. Spong, D. E. Hastings, D. J. Sigmar, and W. A. Cooper, Oak Ridge National Lab Report ORNL/TM-9688 (1985).
 101. P. C. Efthimon, M. Bell, W. R. Blanchard, N. Bretz, J. L. Cecchi, J. Coonrod, S. Davis, H. F. Dylla, R. Fonck, and H. P. Furth, Phys. Rev. Lett. 52, 1492 (1984).
 102. C. Z. Cheng, L. Chen, and M. S. Chance, Ann. Phys. 161, 21 (1984).
 103. J. W. Van Dam and M. N. Rosenbluth, Sherwood Theory Meeting, Madison, Wisconsin, 1985, paper 1C-6.
 104. R. D. Hazeltine and J. D. Meiss, Physics Reports 121, Nos. 1 & 2 (1985).
 105. H. Grad, Phys. Fluids 10, 137 (1967).
 106. E. L. Ince, Ordinary Differential Equations (Longmans, Green and Co., 1927, reprinted by Dover Publications, Inc., New York, 1944).

107. Handbook of Mathematical Functions, edited by M. Abramowitz and I. A. Stegun, 9th ed. (Dover, New York, 1970).
108. R. J. Hawryluk, V. Arunasalam, M. Bell, M. Bitter, K. Bol, K. Brau, S. Davis, F. Dylla, H. Eubank, M. Finkenthal, R. Fonck, R. Goldston, B. Grek, J. Hugill, D. Johnson, R. Kaita, S. Kaye, H. Kugel, D. Mansfield, D. Manos, K. McGuire, R. McCann, D. McCune, D. Mueller, M. Okabayashi, K. Owens, M. Reusch, N. Sauthoff, G. Schilling, G. Schmidt, S. Sesnic, S. Suckewer, G. Tait, H. Takahashi, F. Tenney, and K. Yamazaki, *Phys. Rev. Lett.* 49, 326 (1982).
109. H. L. Berk, L. D. Pearlstein, J. D. Callen, C. W. Horton, and M. N. Rosenbluth, *Phys. Rev. Lett.* 22, 877 (1969).
110. H. L. Berk and Y. Z. Zhang, Institute for Fusion Studies Report IFSR-199 (1985).
111. O. P. Pogutse and E. I. Yurchenko, *Nucl. Fusion* 18, 1629 (1978).
112. D. A. D'Ippolito and J. P. Goedbloed, *Plasma Phys.* 22, 1091 (1980).
113. C. E. Kieras and J. A. Tataronis, *J. Plasma Phys.* 28, 395 (1982).
114. C. Z. Cheng and M. S. Chance, Princeton Plasma Physics Laboratory Report PPPL-2286 (1985).
115. N. A. Krall and A. W. Trivelpiece, Principles of Plasma Physics, (McGraw - Hill Book Company, St. Louis, 1973).
116. J. Kesner, *Nucl. Fusion* 20, 557 (1980).
117. M. N. Rosenbluth, *Phys. Fluids* 11, 869 (1968).
118. A. Bers, in Handbook of Plasma Physics, Chapter 3.2, eds. M. N. Rosenbluth and R. Z. Sagdeev (North - Holland Publishing Company, New York, 1983).
119. H. L. Berk, M. N. Rosenbluth, H. V. Wong, and T. M. Antonsen, *Phys. Fluids* 27, 2705 (1984).

VITA

Daren Price Stotler was born on May 20, 1959 in McAllen, Texas, the son of Mary Price Stotler and Earl Edward Stotler. After graduating from McAllen High School, he entered Rice University in Houston during the Fall of 1977. In May of 1981 he was awarded the Bachelor of Arts degree with honors, majoring in Physics and Materials Science. He worked at the Fusion Energy Division of Oak Ridge National Laboratory as a participant in student research programs during the summers of 1980 and 1981. In September of 1981, he entered the Graduate School of the University of Texas at Austin. While enrolled there, he was employed by the Institute for Fusion Studies.

Permanent address: 1309 Hibiscus
McAllen, Texas 78501

This thesis was typed by the author.